

**Measurement of the $K^+ \rightarrow \pi^+ \mu^+ \mu^-$
Branching Ratio**

Mehran Ardebili

A DISSERTATION
PRESENTED TO THE FACULTY
OF PRINCETON UNIVERSITY
IN CANDIDACY FOR THE DEGREE OF
DOCTOR OF PHILOSOPHY

RECOMMENDED FOR ACCEPTANCE
BY THE DEPARTMENT OF PHYSICS

June 1995

UMI Number: 9527860

UMI Microform 9527860
Copyright 1995, by UMI Company. All rights reserved.

**This microform edition is protected against unauthorized
copying under Title 17, United States Code.**

UMI

**300 North Zeeb Road
Ann Arbor, MI 48103**

© Copyright by Mehran Ardebili, 1995.
All rights reserved.

Abstract

The search for the $K^+ \rightarrow \pi^+ \mu^+ \mu^-$ decay in the 1989-1991 data by Experiment 787 at Brookhaven National Laboratory is reported. This decay is suppressed to first order in the Standard Model because of the GIM mechanism, and it can only proceed through the exchange of a least two electroweak bosons. Comparison of this and other related rare kaon decay rates with the predictions of chiral perturbation theory can be used to constrain the theory's empirical parameters. The analysis is aimed at extracting a peak in the total kinetic energy distribution corresponding to the decay's Q-value of 142.76 MeV. A clear signal with a low level of background is observed. A fit to the energy spectrum yields 196.0 ± 16.7 $K_{\pi\mu\mu}$ events. This results in a branching ratio of $BR(K^+ \rightarrow \pi^+ \mu^+ \mu^-) = (4.98 \pm 0.43_{stat} \pm 0.59_{sys}) \times 10^{-8}$.

to my parents and my sister

Acknowledgments

I owe the completion of this thesis to a great many people to whom I would like to express my gratitude.

Very few graduate students ever have the opportunity of enjoying the guidance of five advisors. I have been among the lucky ones. I am mainly and extremely grateful to one of the brightest individuals I have ever known, Peter Meyers. I always find walking into Peter's office to be a truly delightful experience: encountered by a formidable problem you would go to his office frustrated, puzzled and lost. By the time you leave you are full of new ideas and hope.

Stew Smith has always given me great inspiration and support. I deeply appreciate his encouragement of my work. Frank Shoemaker, Dan Marlow, and Mark Ito never hesitated to give me countless hours of their valuable times to provide detailed answers to my unsolicited questions. I would also like to thank Laurence Littenberg from Brookhaven National Laboratory for his excellent comments and criticism of my work. My many thanks also to John Haggerty and Chris Witzig whose parallel analysis benefitted me largely. The rest of my collaborators have always been generous in their help. My gratitude is also due to a great teacher, Kirk McDonald, who was my first advisor and my second reader.

I would also like to thank my fellow office-mates: Mark Convery, Robert McPherson and Bob Stone. These guys are so much fun to both work and travel with. I am sure they are looking forward to my graduation so that they can lower the lab's thermostat. Having Laurel Lerner as a friend has been a pleasure for many of us. I also enjoyed being friends with a group of very talented graduate students in this department, especially Doug Wright, Patrick Russell, Dan Akerib, and Josh Klein.

Most importantly, I must mention the loving support of my family in my many years as a student. Without my parents and my sister, I would never have been able to reach this point. This thesis truly belongs to them. My many thanks also to a great friend, Shahin Hatamian, who has been a good part of many of my pleasant memories.

Contents

Abstract	iii
Acknowledgments	v
1 Introduction	1
2 Theory	4
2.1 The GIM Mechanism	5
2.2 The $K^+ \rightarrow \pi^+ \mu^+ \mu^-$ Branching Ratio	8
2.2.1 Chiral Perturbation Theory	9
3 Detector	17
3.1 Beam Line	18
3.1.1 Čerenkov Counter	20
3.1.2 Degradar and Beam Counters	21
3.2 Target	22
3.2.1 The I- and V-Counters	23
3.3 Drift Chamber	24

3.4	Range Stack	26
3.4.1	Transient Digitizers	28
3.5	Photon Veto	29
3.5.1	Barrel Veto	30
3.5.2	End Caps	30
3.6	Trigger	31
3.6.1	Level 0	31
3.6.2	Level 1	35
4	Analysis	37
4.1	Analysis Strategy	37
4.2	Monte Carlo	41
4.2.1	Energy and Time Smearing	42
4.2.2	Signal Simulation	44
4.2.3	Background Simulation	47
4.3	Pass2	50
4.3.1	Target Analysis	51
4.3.2	Photon and Neutron Rejection	54
4.3.3	Electron Rejection (in Pass2)	55
4.3.4	Pass2 Output	57
4.4	Pass3	59
4.4.1	Mass Measurement	59
4.4.2	Combination of Charges	69

4.4.3	Conservation of Momentum	70
4.4.4	Pass3 Summary	78
4.5	Background	78
4.5.1	K_{e4}	81
4.5.2	$K_{\mu 4}$	82
4.5.3	Dalitz/ γ Conversions	83
4.5.4	τ	86
4.6	Signal	91
4.6.1	Stability of the Signal	97
4.6.2	FITPI Study of the Final Sample	98
4.6.3	Extracting the Signal	104
5	Acceptance	114
5.1	Accidental Vetoes	116
5.2	Delayed Coincidence	123
5.3	Drift Chamber Reconstruction	125
5.4	Mass Cut	127
5.5	Acceptance Factors from Monte Carlo	130
5.6	Systematic Errors	131
5.6.1	Systematic Error Associated with the B -field	131
5.6.2	Systematic Error Associated with other UMC-Measured Accep- tance Factors	136
5.6.3	Systematic Errors Associated with the Accidentals	136

5.6.4	The Overall Systematic Error	136
5.7	Summary	139
6	Conclusion	140
6.1	w_+	142
6.2	Spectrum	143

List of Figures

2.1	The dominant Feynman diagram in $K^+ \rightarrow \pi^+ \mu^+ \mu^-$ decay.	8
2.2	The other weak/electromagnetic Feynman diagram in $K^+ \rightarrow \pi^+ \mu^+ \mu^-$ decay.	8
2.3	The purely weak diagrams in $K^+ \rightarrow \pi^+ \mu^+ \mu^-$ decay.	9
2.4	First order tree-level diagrams for $K \rightarrow \pi \gamma^*$ The virtual photon γ^* can produce an $e^+ e^-$ or $\mu^+ \mu^-$ pair.	10
2.5	One-loop diagrams for $K \rightarrow \pi \gamma^*$ which contribute to the rate calculation.	11
2.6	Expected branching ratios of $K^+ \rightarrow \pi^+ \mu^+ \mu^-$ and $K^+ \rightarrow \pi^+ e^+ e^-$ as a function of the coupling constant w_+	14
2.7	Expected distribution of the $e^+ e^-$ invariant mass in the $K^+ \rightarrow \pi^+ e^+ e^-$ decay for vector coupling and for the coupling constant $w_+ = 0.89$. . .	15
2.8	Expected distribution of the $\mu^+ \mu^-$ invariant mass in the $K^+ \rightarrow \pi^+ \mu^+ \mu^-$ decay for vector coupling and for the coupling constant $w_+ = 0.89$. . .	15
2.9	Expected ratio of $BR(K^+ \rightarrow \pi^+ \mu^+ \mu^-)/BR(K^+ \rightarrow \pi^+ e^+ e^-)$ as a function of the coupling constant w_+ . The dotted line is the expected ratio for the vector coupling assumption (0.196).	16

3.1	The LESB I beamline at the AGS directs, steers, and selects particles entering the E787 detector.	19
3.2	The side and cross-sectional views of the Čerenkov counter.	20
3.3	The schematic view of the beam instrumentation between the LESB I beamline and the Target.	21
3.4	Target, the I-counter, and the V-counter.	23
3.5	The geometrical drawing of a Drift Chamber cell. The drift trajectories are rough representations of the real paths traversed by the ionization electrons.	25
3.6	Range Stack and the Barrel Veto	27
3.7	Pulse shapes corresponding to a π to μ decay as recorded by the Transient Digitizers.	29
3.8	Block diagram of the level 0 trigger.	32
3.9	Block diagram of the Mean Timers.	34
4.1	Examples of typical $\pi\mu\mu$ events.	39
4.2	Pion momentum distribution in real and UMC-generated τ decays that satisfy the $\pi\mu\mu$ trigger. The narrow range of their momentum allows a Gaussian fit in order to compare the two resolutions.	43
4.3	The π^+ and μ^+ masses of UMC $\pi\mu\mu$ events. The Monte Carlo banks were used to identify the particles in each track. In addition to RS photoelectron statistics, a smearing of $130 \text{ MeV}/E_{RS}$ is applied. . . .	44
4.4	Excess energy in the RS stopping counter for π^+ and π^- tracks. . . .	47

4.5	Distribution of the number of TG triangles in the third track for the UMC-generated $\pi\mu\mu$ events. Some single-cell tracks were missed by the Target routine resulting in the dip above the spike.	53
4.6	Energy distribution in RS layers T through C for the UMC-generated $\pi\mu\mu$ events. Events with more than 120 MeV are rejected.	56
4.7	Distribution of the number of Target elements in UMC-generated τ and $\pi\mu\mu$ events.	59
4.8	Total kinetic energy distribution for the Pass2 output events with ++ and +- combination of charges.	62
4.9	Momentum distribution of reconstructed events in $\pi\gamma\gamma(2)$ triggers (after correction for energy loss in the Target).	64
4.10	Measured mass of for the π^+ , μ^+ , and p^+ samples with and without the 2.5 MeV correction. The gaussian fits are for the comparison purpose.	68
4.11	Total kinetic energy distribution of UMC-generated K_{e4} before and after mass cuts.	71
4.12	Total kinetic energy distribution of UMC-generated $\pi\mu\mu$ before and after mass cuts.	72
4.13	Difference between measured and expected transverse momentum squared for the UMC-generated $\pi\mu\mu$ events and the data.	75
4.14	Schematic K_{e4} event with an observable missing transverse momentum due to a large $\vec{P}_t^{(\nu_e)}$	76

4.15	Difference between measured and expected angle of the TG stub for the UMC-generated $\pi\mu\mu$ events and the data. Events above 0.9 radian were cut.	76
4.16	Difference between measured and expected kinetic energy of the TG stub for the UMC-generated $\pi\mu\mu$ events and the data.	77
4.17	Total kinetic energy distribution for the Pass3 output events.	79
4.18	Mass of the positive and negative tracks in the Pass2 output. Pion and muon hypotheses are used for the positive and negative particles, respectively.	83
4.19	Mass distribution of the positive and negative tracks in the UMC- K_{e4} Pass2 output. Pion and muon hypotheses are used for the positive and negative particles, respectively.	85
4.20	Total kinetic energy distribution of the UMC-generated τ events after Pass2 for (a) all, (b) $\pi\pi$, (c) $\pi\mu$, and (d) $\mu\mu$ pairs.	89
4.21	Total kinetic energy distribution for the Pass3 output events for all three years plotted in (a) 2-MeV and (b) 5-MeV bins.	91
4.22	E_{stub} versus E_{tot} for the data and UMC- $\pi\mu\mu$ Pass3 output events. . .	95
4.23	dE/dx in the two energetic Target tracks for the data and the UMC- $\pi\mu\mu$ Pass3 output events.	96
4.24	Total kinetic energy distribution for the Pass3 output events after the "purification" cuts on Target energies.	97

-
- 4.25 Total kinetic energy distribution of the 1991 events with and without the $B_NTGT \geq 9$ cut. The requirement is expected to have little effect on true $\pi\mu\mu$ events. 98
- 4.26 Energy spectrum for a) all two-track events, and also events in which b) both particles, c) the heavier one, and d) the lighter one passed FITPI. 99
- 4.27 Total kinetic energy distribution of the final events with a fit composed of two gaussians and a second-degree polynomial. 107
- 4.28 Total kinetic energy distributions of the UMC-generated $\pi\mu\mu$ events after Pass3 and also the data events after background subtraction. . . 108
- 4.29 Total kinetic energy distribution of the final events with a fit composed of two gaussians and an exponential term. 111
- 4.30 Total kinetic energy distribution of the final events with a fit composed of a gaussian and an exponential in the [75,250] MeV region. 112
- 4.31 Total kinetic energy distribution of the “purified” final events with a fit composed of two gaussians and a second-degree polynomial. 112
- 4.32 The kaon decay time in the purified $\pi\mu\mu$ sample. 113
- 5.1 Corrected momentum of the reconstructed $K_{\mu 2}$ triggers and the total energy of the ones that pass the [225,260] MeV/c momentum cut. . . 118
- 5.2 The decay time for the kaons in UMC $\pi\mu\mu$ events. The spike at zero for all kaons corresponds to the decays in flight. The right plot indicates that the UMC kaons stop about 0.5 nsec after they are generated. . . 125

5.3	Mass plots for K_{e4} -FITPI and also UMC- $\pi\mu\mu$ pions for the three momentum bins.	128
5.4	Mass plots for $\pi\gamma\gamma(2)$ - $K_{\mu 3}$ and also UMC- $\pi\mu\mu$ muons for the three momentum bins.	128
5.5	Trigger acceptance as a function of the magnetic field.	135
5.6	Total acceptance as a function of the magnetic field in a wide range. The fitted gaussian is simply used as an empirical function to represent the overall shape.	135
5.7	Total acceptance as a function of the magnetic field in a short range.	138
6.1	Total acceptance for several values of $w_+ \geq 0$	144
6.2	Distribution of the normalized di-muon invariant mass $m_{\mu\mu}^2/m_{K^+}^2$ for the (a) purified and (b) UMC-generated $\pi\mu\mu$ events in the signal region ($115 \text{ MeV} < E_{\text{tot}} < 155 \text{ MeV}$).	145
6.3	A Dalitz representation of the (a) purified and (b) UMC-generated $\pi\mu\mu$ events within the signal region. Plotted is E_{μ^+} versus E_{μ^-}	145

List of Tables

4.1	Acceptance for $\pi\mu\mu$ trigger for the 1989 and also 1990/1991 data. Note that the “Delayed Coincidence” in UMC simply requires a hit in the I-Counter.	46
4.2	Relative rates for nn or np direct production in a pion capture. The relative cross sections are calculated from isospin Clebsch-Gordon coefficients.	49
4.3	Time offsets and window half-widths used by the code INTIME.	55
4.4	Summary of Pass2 cuts with their estimated rejections.	57
4.5	Summary of the Target-tracks requirements. Notice that most of these cuts have low rejections and are mainly used for event reconstruction.	58
4.6	Expected and measured masses for the π^+ , μ^+ , and p^+ samples.	67
4.7	Combinations of particles in the $++$ and $+ -$ branches for the three major decays in Pass3.	69
4.8	$\pi\mu\mu$ acceptance and K_{e4} rejection in the $++$ and $+ -$ branches.	70
4.9	Summary of Pass3 cuts with their rejections estimated from part of the 1989 data. † Events with two DC-TG matched tracks.	78

4.10	$\pi\mu\mu$ trigger acceptance for various K^+ decay modes using the full (1989) trigger. The last column shows the expected percentage of each decay mode present in the $\pi\mu\mu$ triggers.	80
4.11	Rejection of various stages of the analysis for UMC- K_{e4} events. The effects of applying the mass- and branching-cuts in two different orders are shown separately.	82
4.12	Number of output events in Pass3.	91
4.13	Correction factor for the measured energy in the Target tracks.	93
5.1	Number of stopped kaons observed during the 1989-1991 runs.	116
5.2	INTIME and trigger accidental vetoing in the $K_{\mu 2}$ data samples.	119
5.3	Efficiency of the trigger and INTIME cuts due to the accidentals.	123
5.4	Acceptance factors for both the online and offline delayed coincidence cuts.	124
5.5	Single-track and the inferred two-track DC reconstruction efficiencies for low-momentum events. The latter is used to normalize the DC efficiency for the UMC-generated events.	127
5.6	The mass cut efficiency for K_{e4} pions in three momentum bins. The adjusted cuts for UMC $\pi\mu\mu$ pions simulate the measured efficiency. The last column shows the fraction of events in each momentum bin.	129

5.7	The mass cut efficiency for $\pi\gamma\gamma(2)$ muons in three momentum bins. The adjusted cuts for UMC $\pi\mu\mu$ muons simulate the measured efficiency. The last column shows the fraction of events in each momentum bin.	129
5.8	The number of UMC- $\pi\mu\mu$ events surviving various Pass3 cuts.	132
5.9	Breakdown of the number of UMC- $\pi\mu\mu$ events surviving the various Target reconstruction cuts.	133
5.10	Systematic errors in the UMC-measured acceptance associated with uncertainties in various detector elements.	137
5.11	Systematic errors associated with simulating the trigger requirements in studying the accidentals. The acceptance pertains to all the prompt energy cuts (both online and offline). The values are for the 1989 data.	138
5.12	Acceptance factors for the $\pi\mu\mu$ search.	139

Chapter 1

Introduction

The development of the Standard Model (SM) of electroweak interactions can be considered as one of the greatest achievements of the recent years. This firm and elegant structure has so far endured many experimental tests. However despite its great predictive power, the model leaves many fundamental issues untouched. Among them are questions about the mass of the fermions, the source of their electric charges, the number of generations of quarks and leptons, the astonishing symmetries among the families, various quantum number conservation laws, and last but not least, the mysterious CP violation.

A precise test of the SM at higher orders in perturbation theory has been the main objective of Experiment 787 at Brookhaven National Laboratory. It involves search for a second order decay that could only happen via weak forces: $K^+ \rightarrow \pi^+ \nu \bar{\nu}$. A measured rate for this decay consistent with the SM would be another victory for the model, whereas a higher rate could lead to the revelation of new bosons.

A by-product of the effort to observe this mode, was the search for other second order kaon decay channels where a mixture of both components of the electroweak forces are involved. $K^+ \rightarrow \pi^+ \mu^+ \mu^-$ is one of them. Whereas this mode can occur via purely weak interactions, the combination of weak and electromagnetic forces constitute the dominant part due to the strength of the latter. Despite this fact, $K_{\pi\mu\mu}$ has a predicted branching ratio of only a few 10^{-8} . Hence, the probability of observing this decay mode is like that of finding a needle in a haystack... literally!

To show this let us assume that the space that a piece of hay occupies in a stack is within a 5 cm tall, 5 mm thick cylinder, and also assume that the same dimensions applies to the needle's space. Moreover suppose that our stack of hay is cone-shaped, with a circular base 5 meters in diameter, and 2 meters high. Then

$$\text{Number of hay pieces in the stack} = \frac{20 \text{ m}^3}{1 \text{ cm}^3} = 2 \times 10^7.$$

Therefore the probability for a *randomly* picked piece to be the needle is, interestingly, $\sim 5. \times 10^{-8}$!

But we tried to be more efficient in our rummaging...

Reported here is the third analysis of the $\pi\mu\mu$ data collected by the E787 collaboration. The first set of data taken during the spring of 1988 was analyzed by Mats Selen who was then a graduate student at Princeton University [1]. The work resulted in three candidate events consistent with the $K_{\pi\mu\mu}$ decay. Based on these

events, an upper limit of $BR(K^+ \rightarrow \pi^+ \mu^+ \mu^-) \leq 2.1 \times 10^{-7}$ with 90% confidence level was published [2]. The $\pi\mu\mu$ data collected during the 1989, 1990 and 1991 runs were initially analyzed by John Haggerty, and Chris Witzig from Brookhaven National Laboratory and by Larry Felawka from TRIUMF [3]. This analysis, similar to the first one, pursued a full event reconstruction based on direct momentum measurements of all three charged decay particles. The analysis found 12 $K_{\pi\mu\mu}$ events in all three years with a background level of less than one event.

The analysis presented here was independently performed on the same data set (1989-1991) with an entirely orthogonal approach. It was aimed at extracting a signal by reconstructing the total kinetic energy released in the decay. Energy deposition by *all* the decay products motivated the search for a peak in the total kinetic energy near the 142.76 MeV Q-value of $K_{\pi\mu\mu}$. This approach accepts even the events in which only two out of the three charged particles carry out most of the available energy. This class of events was found to contain the great majority of the recorded data. Therefore it achieved a very high efficiency as compared to the previous analyses. A fit to the total kinetic energy spectrum of the final events yields $196.0 \pm 16.7 \pm 17.5$ $K_{\pi\mu\mu}$ events. This results in a branching ratio of $BR(K^+ \rightarrow \pi^+ \mu^+ \mu^-) = (4.98 \pm 0.43_{stat} \pm 0.59_{sys}) \times 10^{-8}$.

Chapter 2

Theory

One of the interesting features of the three-generation model of the fundamental fermions is the set of eigenstates in which the quarks and leptons appear. Under a mass operator, the fermions' eigenstates are:

$$\begin{pmatrix} u \\ c \\ t \end{pmatrix} \quad \begin{pmatrix} d \\ s \\ b \end{pmatrix} \quad \text{and} \quad \begin{pmatrix} e \\ \mu \\ \tau \end{pmatrix} \quad \begin{pmatrix} \nu_e \\ \nu_\mu \\ \nu_\tau \end{pmatrix}$$

However, the weak eigenstates of these fermions are:

$$\begin{pmatrix} u \\ c \\ t \end{pmatrix} \quad \begin{pmatrix} d_c \\ s_c \\ b_c \end{pmatrix} \quad \text{and} \quad \begin{pmatrix} e \\ \mu \\ \tau \end{pmatrix} \quad \begin{pmatrix} \nu_{e,c} \\ \nu_{\mu,c} \\ \nu_{\tau,c} \end{pmatrix}$$

For the leptons, the assumption that all three neutrinos are massless directly

implies that

$$\begin{pmatrix} \nu_{e,c} \\ \nu_{\mu,c} \\ \nu_{\tau,c} \end{pmatrix} = \begin{pmatrix} 1 & 0 & 0 \\ 0 & 1 & 0 \\ 0 & 0 & 1 \end{pmatrix} \begin{pmatrix} \nu_e \\ \nu_\mu \\ \nu_\tau \end{pmatrix}$$

This is simply because a massless neutrino has a $\beta = 1$ and thus its lifetime in its rest frame is zero. The neutrino has no time to oscillate into anything else.

In the quark sector, however, the following relation has been proposed by Kobayashi and Maskawa [4]

$$\begin{pmatrix} d_c \\ s_c \\ b_c \end{pmatrix} = \begin{pmatrix} c_1 & c_3 s_1 & s_1 s_3 \\ -c_2 s_1 & c_1 c_2 c_3 - s_2 s_3 e^{i\delta} & c_1 c_2 s_3 + c_3 s_2 e^{i\delta} \\ s_1 s_2 & -c_1 c_3 s_2 - c_2 s_3 e^{i\delta} & -c_1 s_2 s_3 + c_2 c_3 e^{i\delta} \end{pmatrix} \begin{pmatrix} d \\ s \\ b \end{pmatrix} \equiv M \begin{pmatrix} d \\ s \\ b \end{pmatrix}$$

Where $c_i = \cos \theta_i$ and $s_i = \sin \theta_i$. Here θ_1 , θ_2 and θ_3 are the three Euler angles for the rotation of (d, s, b) vector. The additional phase angle δ allows the possibility of a T - or CP -violating amplitude since $e^{i\delta} \rightarrow e^{-i\delta}$ under the time reversal operator.

2.1 The GIM Mechanism

The weak currents have been observed to have two forms: charged and neutral. The hadronic matrix elements for the two currents are formed from the appropriate combinations of $q\bar{q}$ pairs, where q 's are the weak eigenstates of the quarks and the

bar indicates an anti-quark.

The matrix element for the positive current is defined as

$$\begin{aligned} \mathcal{M}_{\text{Charged Current}} &\propto J_{\text{C.C.}}^+ \propto (u \ c \ t) \begin{pmatrix} \bar{d}_c \\ \bar{s}_c \\ \bar{b}_c \end{pmatrix} \\ &= u\bar{d}_c + c\bar{s}_c + t\bar{b}_c \end{aligned}$$

This suggests that the mediator for the weak positive charged current, namely the W^+ , couples the up -quark to all three \bar{d} , \bar{s} , and \bar{b} mass eigenstates (with various strengths, of course). The same is true for couplings of the *charm* and *top* quarks.

Similarly, for the neutral current's matrix element we have

$$\begin{aligned} \mathcal{M}_{\text{Neutral Current}} &\propto J_{\text{N.C.}} \propto (u \ c \ t) \begin{pmatrix} \bar{u} \\ \bar{c} \\ \bar{t} \end{pmatrix} + (d_c \ s_c \ b_c) \begin{pmatrix} \bar{d}_c \\ \bar{s}_c \\ \bar{b}_c \end{pmatrix} \\ &= (u \ c \ t) \begin{pmatrix} \bar{u} \\ \bar{c} \\ \bar{t} \end{pmatrix} + (d \ s \ b) M^{-1} M \begin{pmatrix} \bar{d} \\ \bar{s} \\ \bar{b} \end{pmatrix} \end{aligned}$$

$$\begin{aligned}
&= (u \ c \ t) \begin{pmatrix} \bar{u} \\ \bar{c} \\ \bar{t} \end{pmatrix} + (d \ s \ b) \begin{pmatrix} \bar{d} \\ \bar{s} \\ \bar{b} \end{pmatrix} \\
&= u\bar{u} + c\bar{c} + t\bar{t} + d\bar{d} + s\bar{s} + b\bar{b}
\end{aligned}$$

The fact that $M^{-1}M = I$ follows from the unitarity of the KM matrix. This result clearly shows that the mediator of the neutral weak current, namely the Z^0 , only couples to the quark/anti-quark pairs of the *same* flavor. The suppression of any *flavor changing neutral current*, FCNC, according to the above formalism was first suggested by Glashow, Iliopoulos, and Maiani in 1970 within a two quark doublet frame-work [5]. Their classic proposition (which predicted the existence of the charm quark) is known as the GIM mechanism.

In order to examine the consequences of the GIM mechanism, one can look at the following two semi-leptonic decay modes of K^+ :

$$K^+ \rightarrow \pi^0 \mu^+ \nu_\mu \quad (\text{called } K_{\mu 3}) \quad \text{and,}$$

$$K^+ \rightarrow \pi^+ \mu^+ \mu^-$$

The quark structure of the hadrons in these decays are:

$$K^+ = (u, \bar{s}) \quad \text{and} \quad \begin{cases} \pi^+ = (u, \bar{d}) \\ \pi^0 = (u, \bar{u}) \end{cases}$$

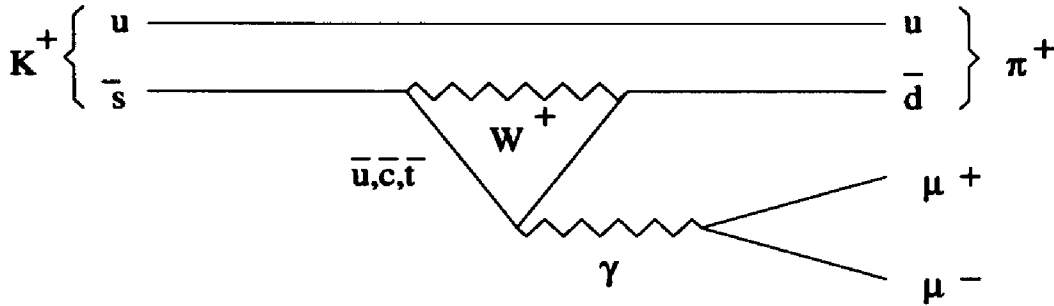


FIG. 2.1: The dominant Feynman diagram in $K^+ \rightarrow \pi^+ \mu^+ \mu^-$ decay.

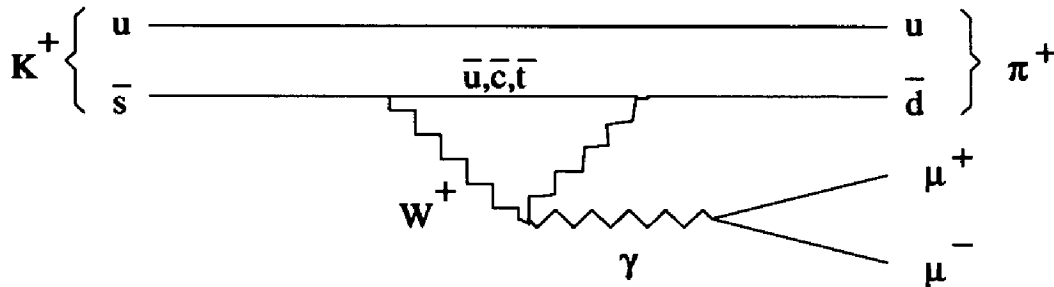
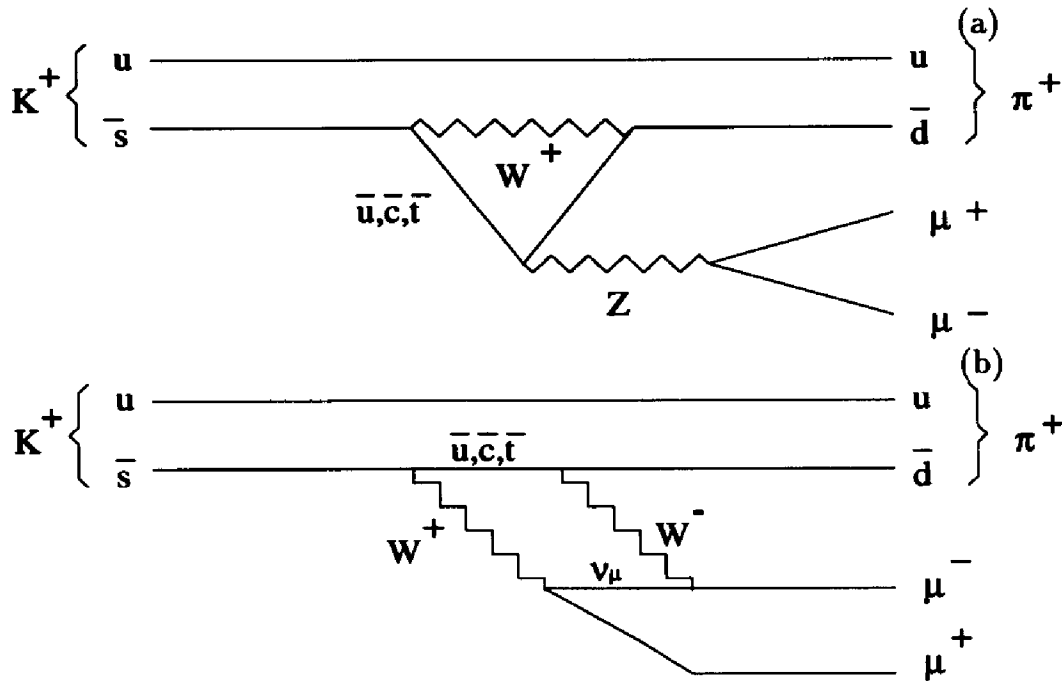


FIG. 2.2: The other weak/electromagnetic Feynman diagram in $K^+ \rightarrow \pi^+ \mu^+ \mu^-$ decay.

The u quark is a spectator in both semi-leptonic decays. This implies that the leptons are the result of a flavor changing weak current that transforms the \bar{s} into a \bar{d} or \bar{u} . In $K_{\mu 3}$ the net charge of the leptons suggests the involvement of a charged current. By the same token, a neutral current has to be present in $\pi\mu\mu$. However, according to the GIM mechanism, the former is allowed whereas the latter is forbidden to first order. Thus one can predict a much higher rate for the $K_{\mu 3}$ decay than $\pi\mu\mu$. Indeed, the branching ratio for $K_{\mu 3}$ is 3.18% – several orders of magnitude larger than the theoretically expected value for $\pi\mu\mu$ ($\sim 10^{-8}$).

2.2 The $K^+ \rightarrow \pi^+ \mu^+ \mu^-$ Branching Ratio

The Feynman diagrams for the $K^+ \rightarrow \pi^+ \mu^+ \mu^-$ decay are shown in figures 2.1, 2.2, and 2.3. Calculations of the above “Penguin” (Figures 2.1, 2.2, and 2.3a) and “Box”


 FIG. 2.3: The purely weak diagrams in $K^+ \rightarrow \pi^+ \mu^+ \mu^-$ decay.

diagrams (Figure 2.3b) are very complicated. They involve the evaluation of hadronic matrix elements of four-quark operators, in particular those concerning $\Delta I = \frac{1}{2}$ transitions. This is a very difficult task since it requires calculation of the same matrix elements to all orders in the effective theory of strong interactions *and* to lowest order in the electromagnetic coupling. However, a different approach can be taken towards the problem by only considering the meson fields and the long-range forces.

2.2.1 Chiral Perturbation Theory

The decay amplitudes of $K \rightarrow \pi \ell^+ \ell^-$ transition (with $\ell = e$ or μ) are calculated by Ecker, Pich and de Rafael in chiral perturbation theory to the first non-trivial order [6]. Within the framework of the effective chiral lagrangian, the lowest order calculation pertains to the tree level Feynman diagrams shown in Figure 2.4. These

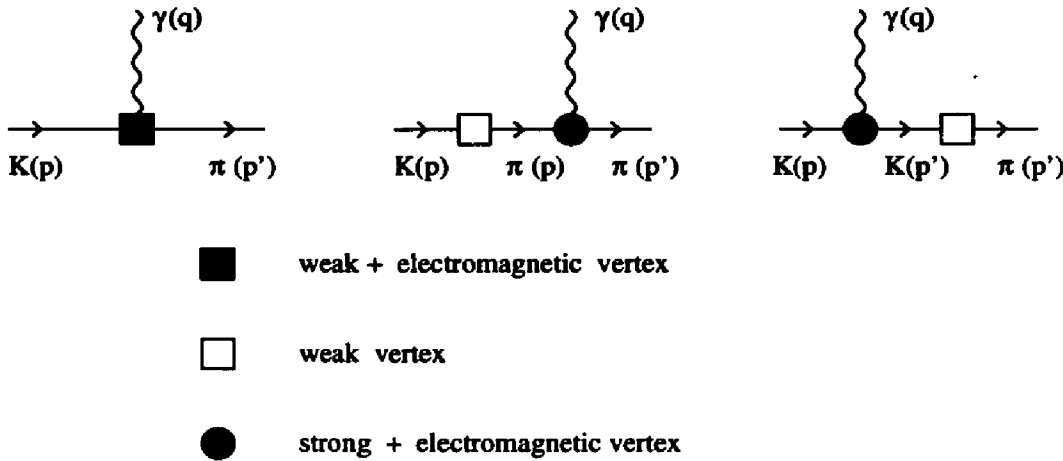


FIG. 2.4: First order tree-level diagrams for $K \rightarrow \pi \gamma^*$. The virtual photon γ^* can produce an e^+e^- or $\mu^+\mu^-$ pair.

diagrams lead to the following amplitude:

$$\left(\sqrt{\frac{1}{2}} G_F s_1 c_1 c_3 g_8 \right) f_\pi^2 (p + p')_\mu \left\{ 2ie + 2ip^2 \frac{i}{p^2 - m_\pi^2} ie + ie \frac{i}{p'^2 - M_K^2} 2ip'^2 \right\}$$

where $|g_8| \simeq 5.1$ is a dimensionless coupling constant whose value is experimentally determined from $K \rightarrow \pi\pi$, and $f_\pi \simeq 93.3$ MeV. The sum of the above three terms vanishes exactly for all values of q as long as $p^2 = M_K^2$ and $p'^2 = m_\pi^2$ (on-shell mesons). This is shown to be due to the combined requirements of gauge and chiral symmetries in the effective lagrangian.

To the above diagrams should be added the higher order tree-level contributions (Figure 2.5) from the effective electroweak chiral lagrangian to fourth order in derivatives and meson masses. The result yields the following decay rate:

$$\Gamma(K \rightarrow \pi \ell^+ \ell^-) =$$

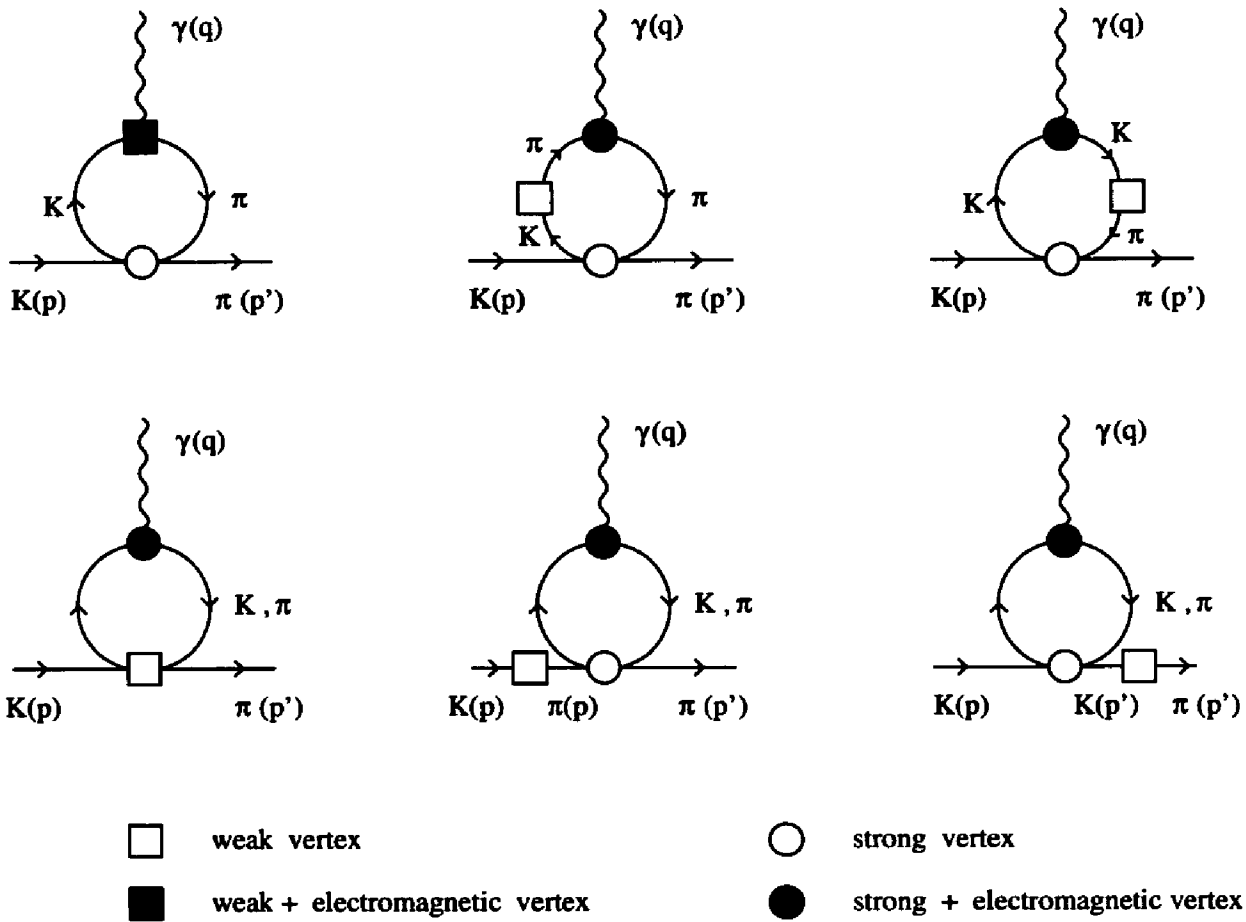


FIG. 2.5: One-loop diagrams for $K \rightarrow \pi \gamma^*$ which contribute to the rate calculation.

$$\bar{\Gamma} \int_{4\epsilon}^{(1-\sqrt{\delta})^2} dz \left(1 + z^2 + \delta^2 - 2z - 2\delta - 2z\delta\right)^{3/2} (1 - 4\epsilon/z)^{1/2} (1 + 2\epsilon/z) \left|\hat{\phi}_+(q^2)\right|^2$$

where

$$z = \frac{q^2}{M_K^2} = \frac{m_{\ell\ell}^2}{M_K^2} \quad \epsilon = \frac{m_\ell^2}{M_K^2} \quad \delta = \frac{m_\pi^2}{M_K^2}$$

and

$$\bar{\Gamma} = \left(\sqrt{\frac{1}{2}} G_{FS1} c_1 c_3\right) \frac{\alpha^2 M_K^5 |g_8|^2}{12\pi(4\pi)^4} = 1.37 \times 10^{-22} \text{ GeV}$$

$\hat{\phi}_+$ is defined in terms of the kaon and pion fields as

$$\hat{\phi}_+(q^2) = - \left[\phi_K(q^2) + \phi_\pi(q^2) + w_+\right]$$

ϕ_K and ϕ_π are defined as:

$$\phi_K(q^2) = \int_0^1 dx \left[\frac{M_K^2}{q^2} - x(1-x)\right] \log \left[1 - \frac{q^2}{M_K^2} x(1-x)\right],$$

$$\phi_\pi(q^2) = \int_0^1 dx \left[\frac{M_\pi^2}{q^2} - x(1-x)\right] \log \left[1 - \frac{q^2}{M_\pi^2} x(1-x)\right].$$

Setting $\hat{\phi}_+(q^2) = 1$ yields the vector coupling prediction for the $K_{\pi\ell\ell}^+$ branching ratios.

The value of the constant w_+ is not theoretically known and is to be determined from the experimental data. However, w_+ is the same for both $\ell = e$ and μ . Thus in order to estimate the theoretical prediction for the $\pi\mu\mu$ branching ratio, one can use the experimentally measured branching ratio for $K^+ \rightarrow \pi^+ e^+ e^-$ to deduce w_+ .

Substituting for $\hat{\phi}_+(q^2)$ and considering the fact that

$$\Gamma(K^+ \rightarrow \text{all}) = \frac{\hbar}{\tau_{K^+}} = \frac{6.58 \times 10^{-25} \text{ GeV sec}}{1.2371 \times 10^{-8} \text{ sec}} = 5.32 \times 10^{-17} \text{ GeV}.$$

one obtains

$$BR(K^+ \rightarrow \pi^+ e^+ e^-) = (3.15 - 21.1w_+ + 36.1w_+^2) \times 10^{-8}$$

$$BR(K^+ \rightarrow \pi^+ \mu^+ \mu^-) = (3.92 - 32.6w_+ + 70.3w_+^2) \times 10^{-9}.$$

In a paper published by the BNL E777 collaboration [7], the authors extract $w_+ = 0.89_{-0.14}^{+0.24}$ from a simultaneous fit of the decay rate and the spectrum. The fit yields a $BR(K^+ \rightarrow \pi^+ e^+ e^-) = (2.99 \pm 0.22) \times 10^{-7}$ as opposed to the directly measured value of $(2.75 \pm 0.22 \pm 0.13) \times 10^{-7}$. The expected branching ratios of both $K_{\pi\mu\mu}^+$ and $K_{\pi ee}^+$ decays as a function of w_+ were calculated [8] and plotted in Figure 2.6. Using $w_+ = 0.89_{-0.14}^{+0.24}$,

$$\text{Expected } BR(K^+ \rightarrow \pi^+ \mu^+ \mu^-) = 3.1_{-1.3}^{+2.2} \times 10^{-8}.$$

Figures 2.7 and 2.8 show the expected distribution of the $\ell^+ \ell^-$ invariant masses for both the vector coupling assumption and the chiral perturbation theory with $w_+ = 0.89$. Finally, Figure 2.9 shows the ratio of $K^+ \rightarrow \pi^+ \mu^+ \mu^-$ versus $K^+ \rightarrow \pi^+ e^+ e^-$ branching ratios as a function of w_+ .

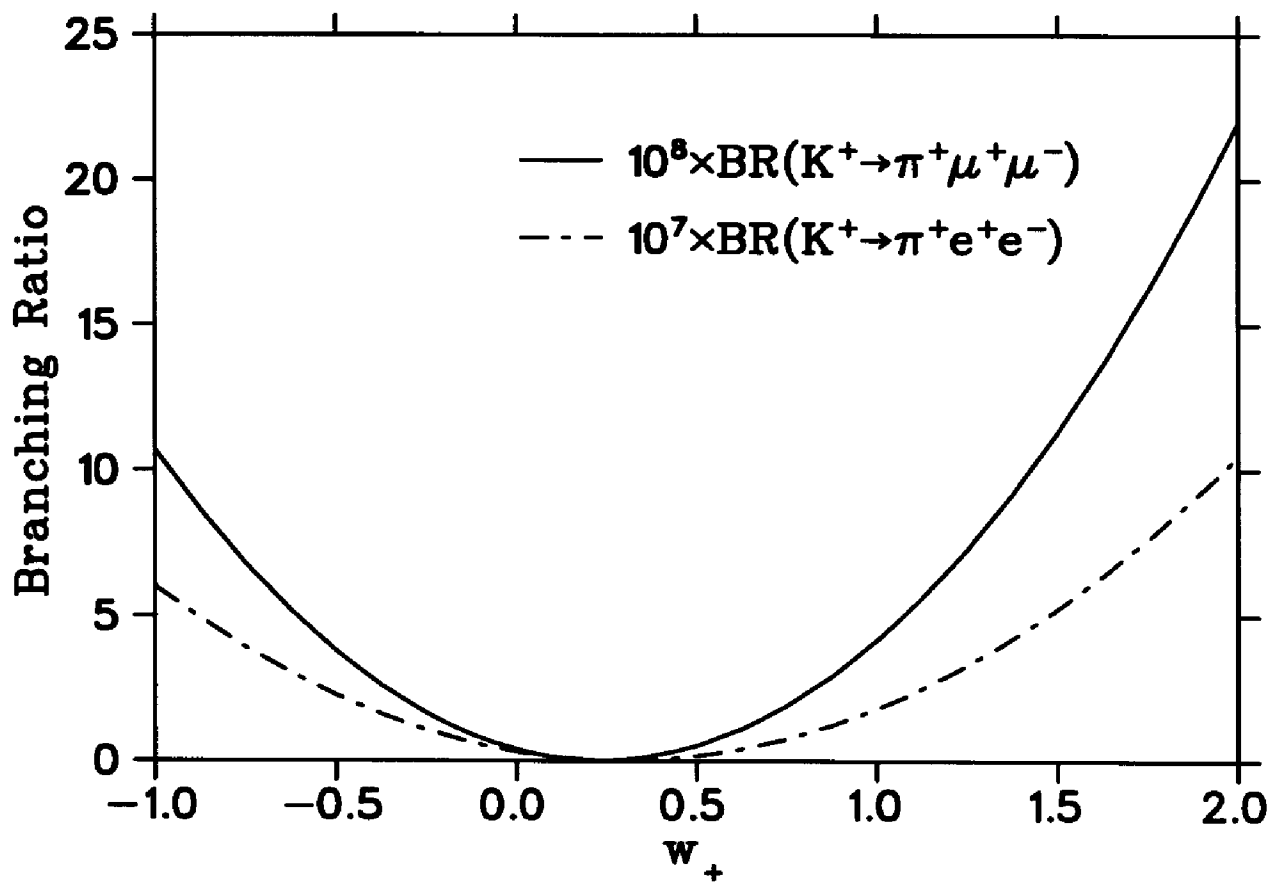


FIG. 2.6: Expected branching ratios of $K^+ \rightarrow \pi^+ \mu^+ \mu^-$ and $K^+ \rightarrow \pi^+ e^+ e^-$ as a function of the coupling constant w_+ .

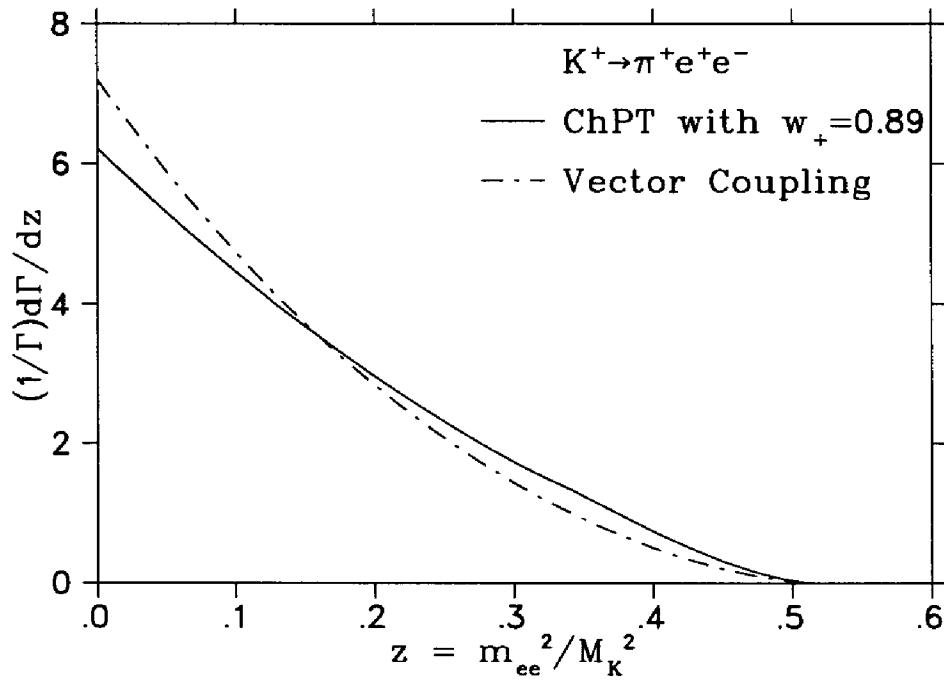


FIG. 2.7: Expected distribution of the e^+e^- invariant mass in the $K^+ \rightarrow \pi^+ e^+ e^-$ decay for vector coupling and for the coupling constant $w_+ = 0.89$.

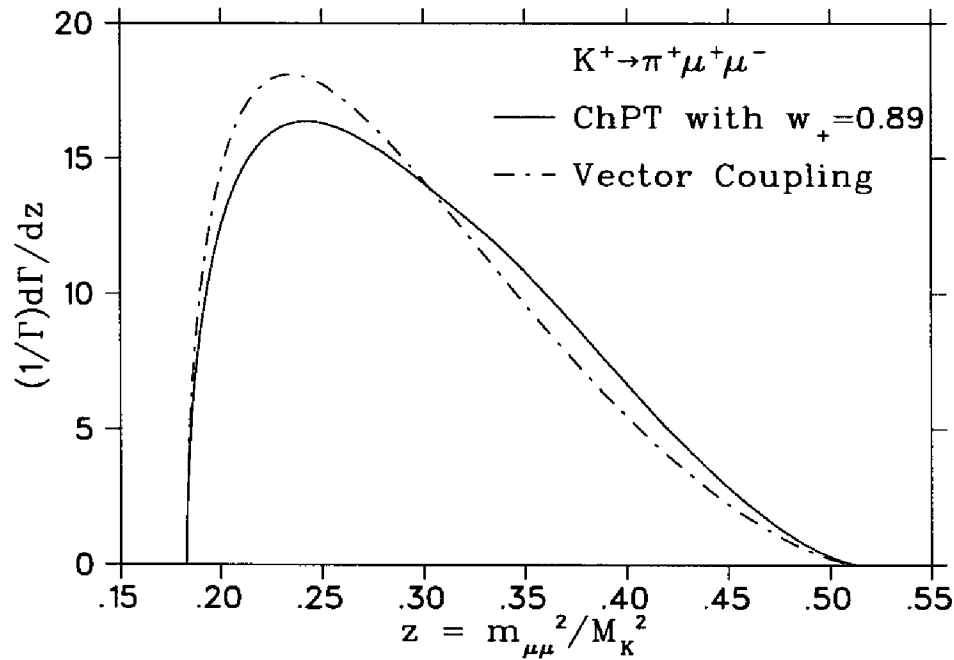


FIG. 2.8: Expected distribution of the $\mu^+\mu^-$ invariant mass in the $K^+ \rightarrow \pi^+ \mu^+ \mu^-$ decay for vector coupling and for the coupling constant $w_+ = 0.89$.

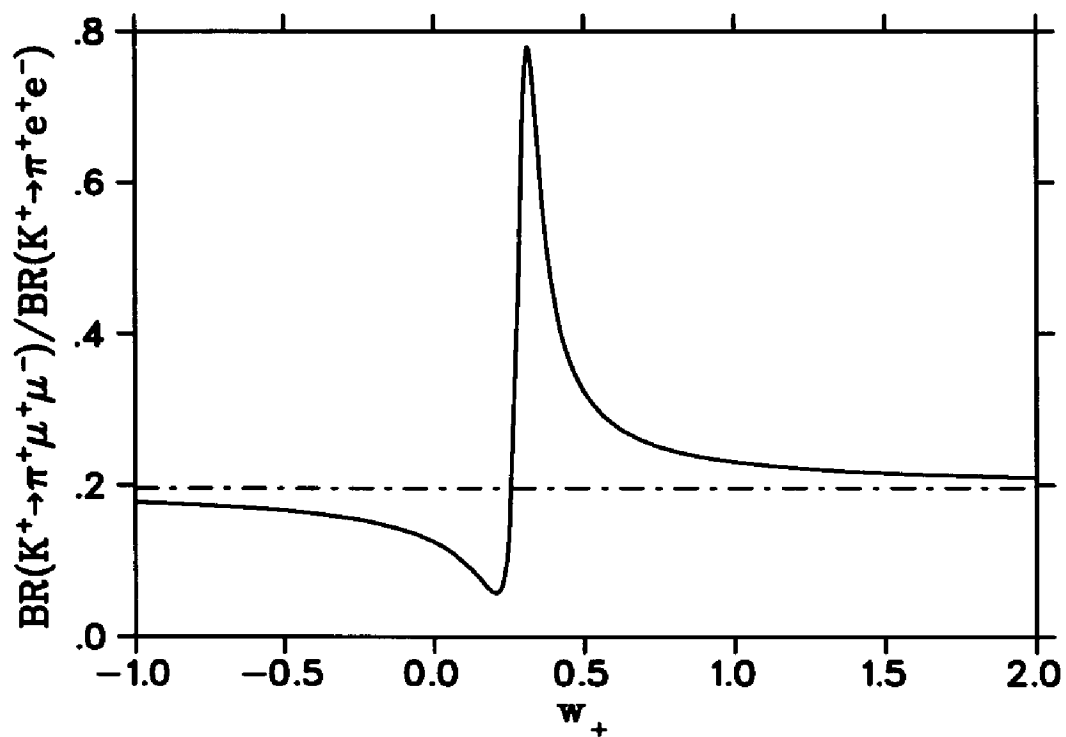


FIG. 2.9: Expected ratio of $BR(K^+ \rightarrow \pi^+ \mu^+ \mu^-)/BR(K^+ \rightarrow \pi^+ \mu^+ e^+ e^-)$ as a function of the coupling constant w_+ . The dotted line is the expected ratio for the vector coupling assumption (0.196).

Chapter 3

Detector

The design of the E787 detector was included in the 1983 proposal “The Search for the Rare Decay $K^+ \rightarrow \pi^+ \nu \bar{\nu}$ ”. The main objective of the design has been to maximize the detection efficiencies for this particular decay (whose signature is an unaccompanied π^+ emitted by a stopped K^+) in the kinematic region between the $K_{\pi 2}$ ($K^+ \rightarrow \pi^+ \pi^0$) and $K_{\mu 2}$ ($K^+ \rightarrow \mu^+ \nu_\mu$) two-body decays [9]. The design includes a 4π photon vetoing capability in order to eliminate the $K_{\pi 2}$ and the radiative $K_{\mu 2}$ backgrounds. The calorimetric part of the detector has a cylindrical geometry which restricts the acceptance for the charged decay particle to only a $\sim 2\pi$ solid angle subtended at the center of the detector. The entire detector is contained within a solenoidal magnet producing a uniform 1 Tesla field along the axis of the cylinder. This field is suitable for the momentum measurement of about 200 MeV/c² particles in the detector’s tracking chamber.

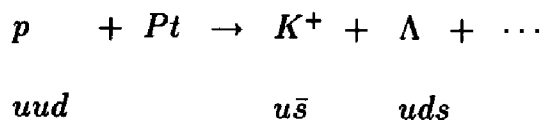
In addition to $\pi \nu \bar{\nu}$, the experiment has implemented triggers to search for other

second order decay modes of the K-meson including $K^+ \rightarrow \pi^+ \mu^+ \mu^-$ and $K^+ \rightarrow \pi^+ \gamma \gamma$. However, the topology of the detector is not optimized for these other modes and limits their corresponding acceptances. In the case of $\pi \mu \mu$, the main limiting factors are the relatively high magnetic field, excessive material within the target, and the absence of a Čerenkov detector along the decay-particles' path in order to positively identify pions and muons. Nevertheless, the very efficient photon rejection capability of the detector, its vertex-finding capability, along with a high rate of kaon decays make it desirable for the E787 experiment to look for such decays.

In the following section, the various subsystems of the detector relevant to the $\pi \mu \mu$ search are described.

3.1 Beam Line

The positive kaons in this study are generated as a 28 GeV proton beam (including up to 6×10^{12} particles per spill) from the Alternating Gradient Synchrotron hits an 89 mm long platinum target. The kaons are produced primarily through the reaction



where the by-products of the reaction can include pions, protons, muons, alphas, or other nuclei. The low-energy particles given off at a production angle of 10.5° are captured and directed towards the secondary beamline for the E787 detector.

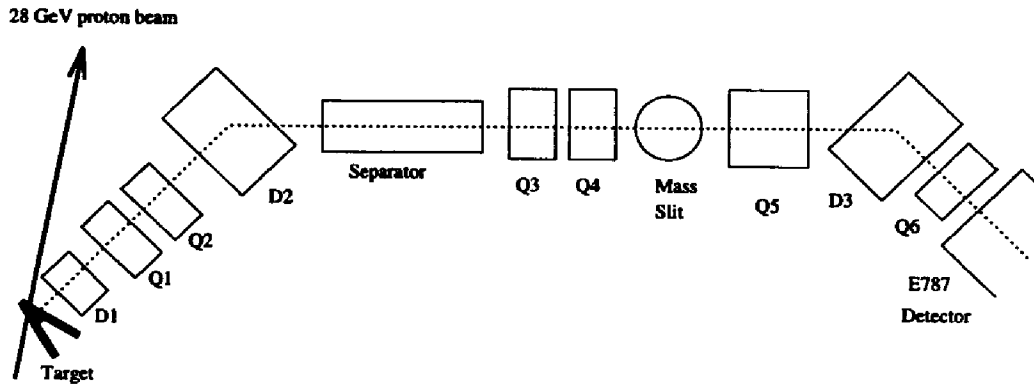


FIG. 3.1: The LESB I beamline at the AGS directs, steers, and selects particles entering the E787 detector.

This Low Energy Separated Beam (LESB I) selects, focuses, and steers the positive particles that have a momentum of about 800 MeV/c. An electromagnetic separator, producing crossed \mathbf{E} and \mathbf{B} fields, disperses the beam both in momentum p and velocity v . After further focusing, a mass slit selects a specific portion of the v - p space, thus choosing the mass to be that of the kaon.

Despite the mass selection, many protons, muons and pions may still enter the detector. Among these, the π^+ is the major source of beam contamination. In 1988 through 1991, fine tuning of the optics of the LESB I resulted in a ratio of 1:3 for K^+ to π^+ .¹ The slow-extraction of the AGS proton beam gives a uniform rate of kaons over the ~ 1.4 sec duration of each spill. The typical rate of kaons reaching the center of the detector was 3×10^5 per spill. Decays of kaons were separated on average by about 3.3 μ seconds. This number is to be compared with the 40 nsec dead-time of the level 0 trigger (see Section 3.6).

¹Implementing an improved and entirely new beamline in 1992 (LESB III) reduced that ratio to 3:1, hence providing a very clean source of kaons entering the detector.

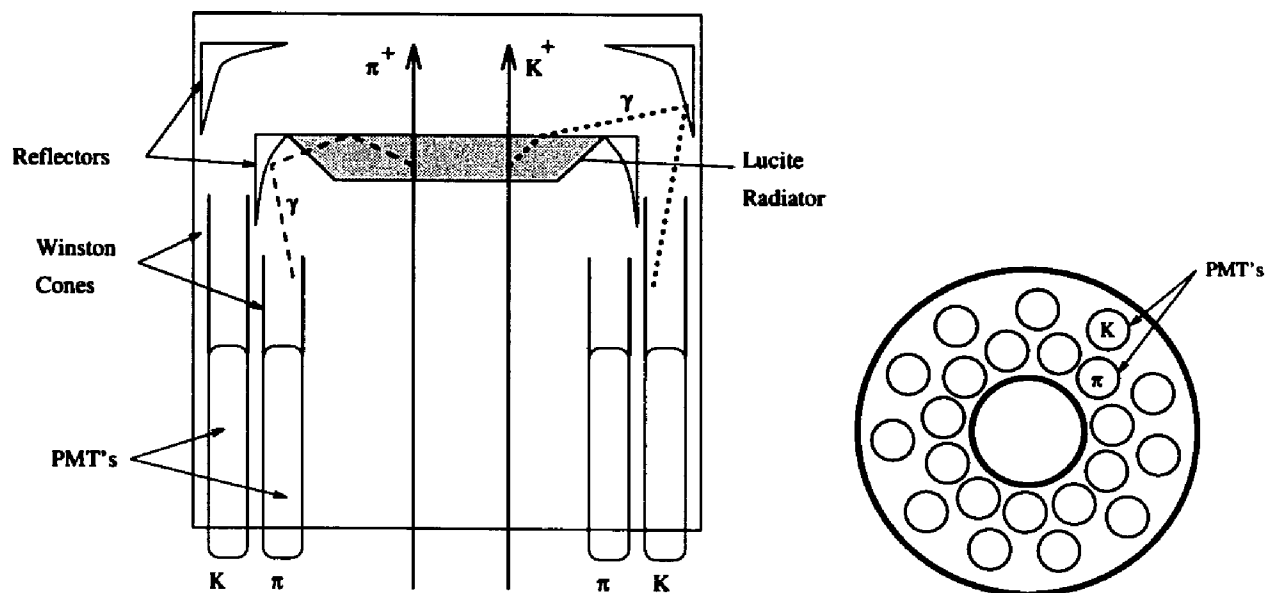


FIG. 3.2: The side and cross-sectional views of the Čerenkov counter.

3.1.1 Čerenkov Counter

In order to tag the kaons and veto the pions in the beam, a double-ring Čerenkov counter is used. This detector takes advantage of the fact that the Čerenkov photons generated by 800 MeV/c kaons and pions within the Lucite radiator have directions that lie on different sides of the critical angle. Therefore the K photons leave the radiator whereas the pion's are internally reflected (Figure 3.2). This allows collection of the light from either particle on separate sets of photomultiplier tubes (PMT's). The multiplicity sum of the discriminated signals from each of the 10 tubes in a given ring is discriminated with a threshold corresponding to 6 struck tubes to establish the passage of a K or a π .

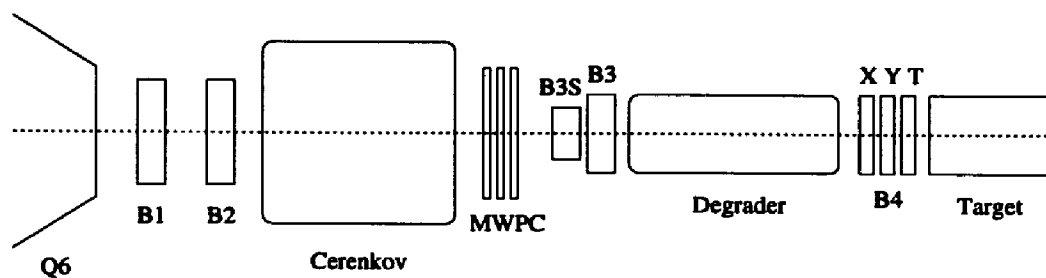


FIG. 3.3: The schematic view of the beam instrumentation between the LESB I beamline and the Target.

3.1.2 Degradation and Beam Counters

Figure 3.3 shows the beam instrumentation between the last quadrupole of LESB I and the Target. In addition to the Čerenkov counter, it includes a series of scintillator counters that are mainly used for beam tuning. The B1 and B2 hodoscopes provide a horizontal profile for the beam. B1 consists of 40 mm high and 35, 30, 21, 21, and 55 mm wide elements going from left to right as seen by the beam. B2 has the same elements in the reversed order such that the gaps between the fingers of each hodoscope is overlapped by the other's. In addition, two counters 12.7 mm high and 203 mm wide are mounted above and below the center of the B2 hodoscope to intercept the small tails of the beam in the vertical direction. Moreover, two L-shaped counters are configured to detect any halo of beam particles that miss any of the above counters. All of these are viewed by Hamamatsu R1548 phototubes and read out by Analogue to Digital Convertors (ADC) and Time to Digital Convertors (TDC).

Immediately downstream of the Čerenkov is a multi-wire proportional chamber (MWPC) that consists of three planes (X, U, V). They include 70, 60 and 60 anode sense wires made of 12 μm Au-plated tungsten. The wires are run vertically in the

X -plane and at $\pm 45^\circ$ in the U - and V -planes. The chamber can provide the profile and multiplicity information on the beam particles.

The B3 and B3S counters are $76 \times 64 \text{ mm}^2$ and $51 \times 38 \text{ mm}^2$, respectively. Also used in beam tuning, their relative rates provides information regarding the convergence of the beam before the entrance to the degrader.

The 800 MeV/ c kaons are slowed down by a 535 mm long degrader. Made of BeO, the degrader combines a high density with a low atomic number in order to have a large braking power while minimizing the effects of multiple scattering.

The B4 counter consists of three layers which are located between the degrader and the front face of the Target. The first two layers, B4Y and B4X, are hodoscopes each including four $25.4 \times 101.6 \text{ mm}^2$ fingers. The third layer, B4T, is a single counter with the same hexagonal shape as the Target's. Its PMT's signal is used as part of the trigger to tag a kaon entering the Target.

3.2 Target

The Target (TG) consists of a set of 378 triangular cells within a hexagon transverse to the incoming kaons (Figure 3.4). Each equilateral triangle (or cell) is 6 mm on a side, and the hexagon is 5.31 cm from center to an edge. Each cell is made of six 2 mm-diameter scintillating fibers. The fibers have a core of S-101 styrene, a $25\text{-}\mu\text{m}$ vinyl-acetate cladding to improve internal reflection, and a 1000 \AA aluminum coating to protect the cladding and to eliminate cross-talk between adjacent fibers. The six fibers in each cell were glued together with 1.2 gr/cm^3 epoxy. Considered

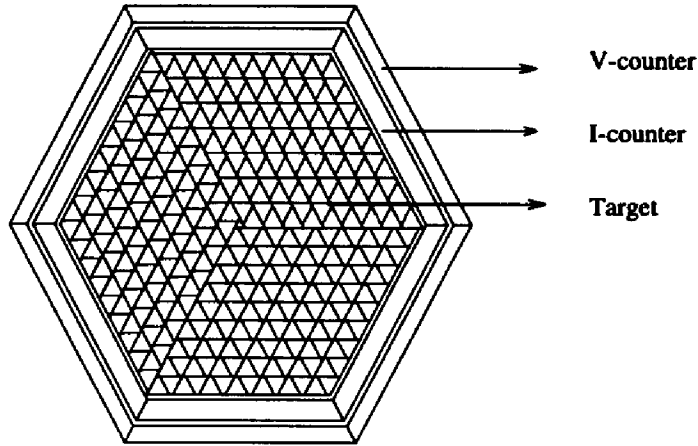


FIG. 3.4: Target, the I-counter, and the V-counter.

the 379th cell, a single fiber in the center of the hexagon fills the gap between the three diamond-shape subsections of the Target (each including 63 cells). Each cell is coupled to a 10 mm diameter Hamamatsu R1635-02 photomultiplier tube with high gain first dynodes for good sensitivity. Light yield is measured to be one photoelectron per millimeter path for a minimum ionizing particle. Each PMT is instrumented with an ADC and a TDC. Event reconstruction uses the time and energy measurements as well as the position information from the highly-segmented target.

3.2.1 The I- and V-Counters

The Target assembly is surrounded by two sets of plastic scintillators as shown in Figure 3.4. The first set consists of six *I-counters*, 240 mm long and 6.4 mm thick, which define the fiducial length of the target. Also, the stopping of the kaon is enforced by requiring a ~ 2 nsec separation between the TG signal from a K^+ and a signal from any I-counter which would be due to the kaon's decay product.

The second set consists of six modules which are 1960 mm long and 5 mm thick. They overlap with the downstream end of the I-counters. This set has been designed for vetoing the hits outside of the fiducial region (hence the name *V-counters*).

Both the I-counters and the V-counters are viewed by EMI 9954KB photomultiplier tubes. The signals from each tube is split and run into ADC and TDC electronics as well as Transient Digitizers (described in 3.4.1).

3.3 Drift Chamber

The cylindrical Drift Chamber (DC) surrounds the Target subtending an approximately 2π sr solid angle for the decay products of the kaon. It consists of five super-layers which include 36, 40, 50, 60 and 70 cells counting outwards. The cross sectional view of a cell is shown in Figure 3.5. Cells in layers 1, 3, and 5 are axial with respect to the cylinder whereas those in layers 2 and 4 have stereo angles of $+3.1^\circ$ and -4.0° respectively to allow for a longitudinal momentum measurement. Cells within a layer are identical, but the cell size varies from layer to layer between 12 and 17 mm in half width. There are 8 anode sense wires within each cell; however, only the 6 middle ones are instrumented with TDC's to avoid the cell-end distortions in the electric field and to reduce the effects of the Lorentz angle. The electric field of ~ 1.5 kV/cm in the drift regions and the magnetic field of 1 Tesla result in a drift velocity of about $50 \mu\text{m/nsec}$ and a Lorentz angle of about 25° . The chamber gas is a 1 atmosphere, 50:50 mixture of Ar:C₂H₆ with Argon bubbled through ethanol at 0 °C. The active volume of the chamber, from 95 and 432 mm in radius and 508 mm

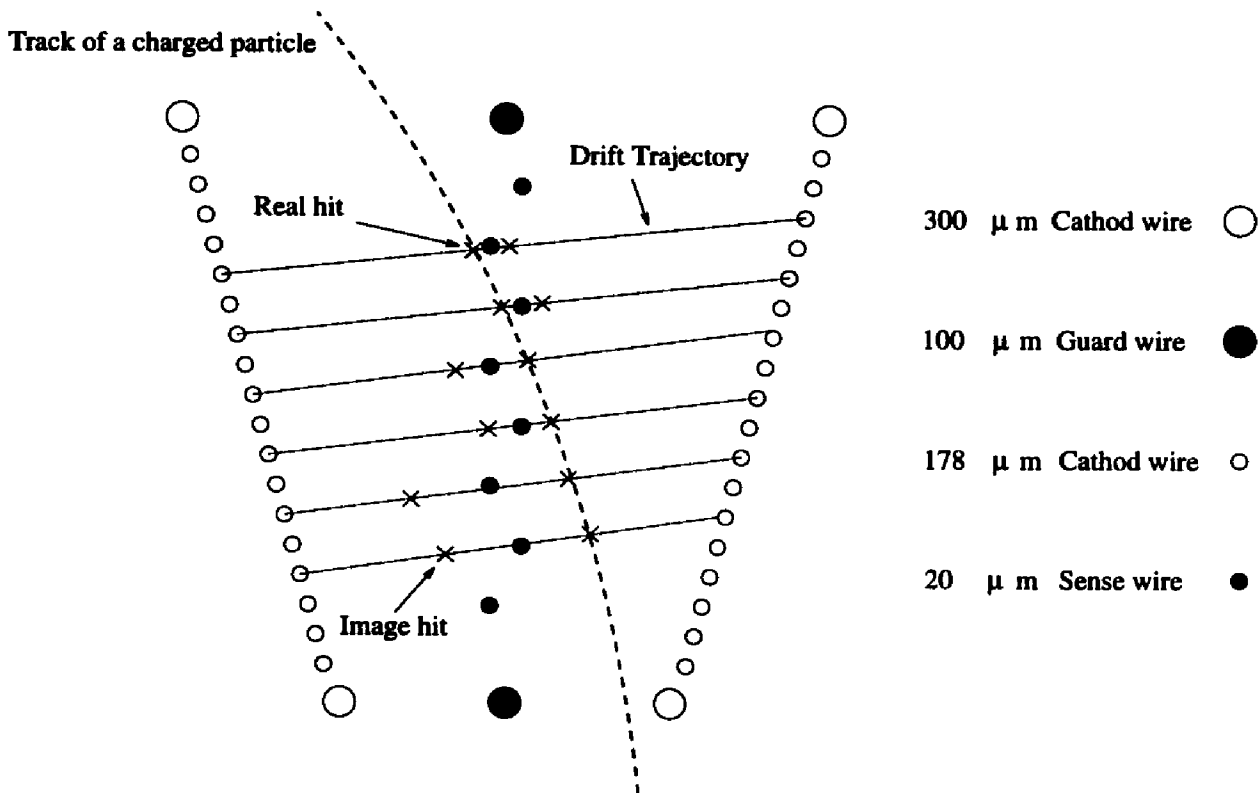


FIG. 3.5: The geometrical drawing of a Drift Chamber cell. The drift trajectories are rough representations of the real paths traversed by the ionization electrons.

in length, is enclosed between two 9.5 mm thick aluminum end-plates, an 80 mgr/cm² thick inner wall, and a 94 mgr/cm² outer wall. Both cylindrical walls are made of graphite-fiber epoxy with a density of 1.70 gr/cm³.

In addition, wires 1 through 4 in the layer 1 cells and wires 3 through 5 in the layer 2 cells (in 1989) were instrumented with ADC modules for dE/dx measurements. In 1990-91, the three ADC channels for each layer 2 cell were connected to wires 2 through 4.

The drift velocity, Lorentz angle, and time offsets (pedestals) are determined by iterative fitting of tracks in the chamber. For the drift velocity, tracks in a zero magnetic field are used. Position resolutions are determined from residuals in a fit,

and their values for axial and stereo wires are about $150 \mu\text{m}$ and 3.0 cm respectively. The momentum resolution is calculated from the width of the distribution for a monoenergetic decay product such as $K_{\pi 2}$ pions after correcting for the momentum loss in the Target. This yields a $\delta P/P$ of 2.12% (from $205 \text{ MeV}/c$ $K_{\pi 2}$ π 's).

3.4 Range Stack

The charged decay products of the kaon come to a stop in a stack of Bicron's BC408 plastic scintillating counters. The azimuth is divided into 24 sectors; each sector is made of 20 layers of 1.82 m long, 19.05 mm thick modules plus an additional innermost 520 mm long, 6.35 mm thick module called the "T-counter". The T-counter defines the fiducial region for the triggering charged particles yielding a $\sim 2\pi$ sr acceptance (covering the $[\frac{\pi}{3}, \frac{2\pi}{3}]$ region in polar angle and the full 2π in azimuth).

In order to simplify the problem of fitting the phototubes in a limited space, the nine innermost 19-mm layers were grouped into three *multiplexed* super-layers: A = {2, 3, 4, 5}, B = {6, 7, 8}, and C = {9, 10}. Each superlayer is viewed by a single phototube at each end. This grouping does not affect the range resolution in the $\pi\nu\bar{\nu}$ search above the $K_{\pi 2}$ peak ($\pi\nu\bar{\nu}(1)$) as the π^+ 's average range would be $> 19 \text{ cm}$. In addition, the choice of four layers for superlayer A was to facilitate a trigger for the $\pi\nu\bar{\nu}$ search below the $K_{\pi 2}$ peak ($\pi\nu\bar{\nu}(2)$). In this region, the π^+ is expected to stop within the multiplexed layers; however, this region could also be flooded by the pions from τ decays ($K^+ \rightarrow \pi^+\pi^+\pi^-$). This problem was addressed by grouping the layers prone to these π 's as superlayer A and requiring a penetration as far as at least

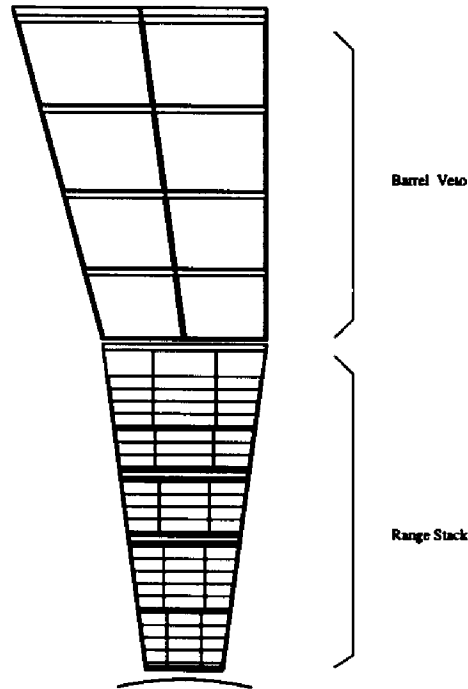


FIG. 3.6: Range Stack and the Barrel Veto

superlayer B in the $\pi\nu\bar{\nu}(2)$ trigger.

The 720 photomultiplier tubes (PMT's) used in the range stack include 28-mm diameter Hamamatsu R1398 tubes for the T-layers and EMI 9954KB tubes for the stopping layers. The light output at each end produces approximately 15 photoelectrons in the PMT per MeV deposited in the scintillator. However, the signal from each PMT is split and delivered to three electronic systems: *i*) the trigger (which uses a discriminated logic pulse) *ii*) the ADC's, and *iii*) the Transient Digitizers (TD's). The latter provide a pulse shape history of the PMT signals as well as precision timing ($\sigma \sim 500$ psec) for the RS. The large dynamic range of the signals from layers A, B, and C are compressed using amplifiers with logarithmic transfer function before being fed into the TD's.

Imbedded in each sector of the RS are two layers of multi-wire proportional cham-

bers (RSPC's) located radially at approximately 635 and 720 mm; *i.e.*, after layers C and 14. They provide axial (z) and azimuthal ($r\phi$) information for the tracks deep inside the RS. The particles satisfying the $\pi\mu\mu$ trigger, however, always stop short of the first RSPC. Therefore the proportional chambers were of no benefit to this analysis.

3.4.1 Transient Digitizers

Positive identification of the pion in a $\pi\nu\bar{\nu}$ event is achieved by requiring the detection of the following chain of decays:

$$\pi^+ \rightarrow \mu^+ \nu_\mu \quad KE_{\mu^+} = 4.12 \text{ MeV}, \quad \tau = 26.03 \text{ nsec}$$

$$\mu^+ \rightarrow e^+ \nu_e \bar{\nu}_\mu \quad KE_{e^+} < 53 \text{ MeV}, \quad \tau = 2197.03 \text{ nsec}$$

Observation of the $\pi^+ \rightarrow \mu^+ \rightarrow e^+$ signature is essential in rejecting the abundant $K_{\mu 2}$ background. In order to achieve a high acceptance in detecting the $\pi^+ \rightarrow \mu^+$ decay and considering the typical signal widths of 30-40 nsec, a sampling rate of $> 3 \times 10^8 \text{ s}^{-1} \approx (\frac{1}{8})^{-1}$ is needed. This allows observation of a shoulder in the stopping π^+ signal – due to the 4.12 MeV muon – even if the pulses are not separated (see Figure 3.7).² Also, considering the 2.2 μsec lifetime of the muon, a memory depth of $\sim 10 \mu\text{sec}$ is desirable to insure a high efficiency in observing the e^+ . To meet these specifications, the E787 experiment has designed and constructed a system

²A routine called FITPI was used to recognize such patterns in the recorded pulses.

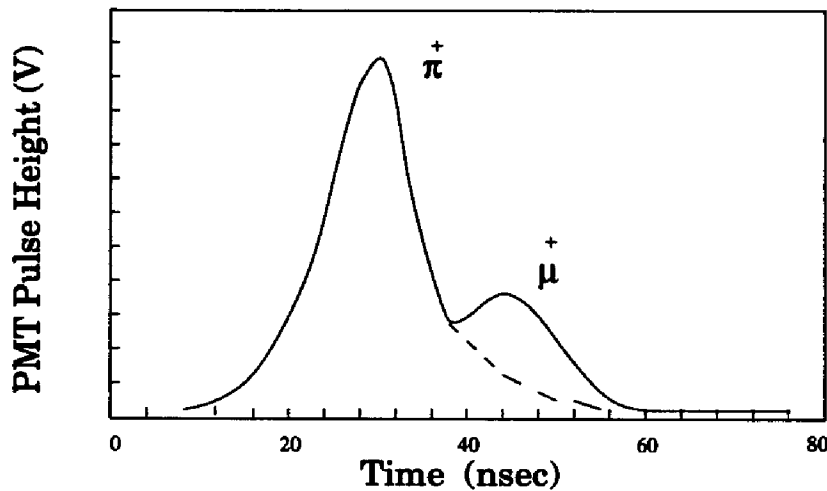


FIG. 3.7: Pulse shapes corresponding to a π to μ decay as recorded by the Transient Digitizers.

of 5×10^8 samples per second with a dynamic range of 8 bits [10]. To lower the total number of channels however the TD branches of PMT signals from the same layers in four adjacent sectors are multiplexed. In addition to the RS, several other detector subsystems, including the IC, Čerenkov, *etc.* have been instrumented with the TD's in order to improve their timing resolution and accidental rejection. A routine called FITPI was used to recognize such a pattern in the recoded pulses.

3.5 Photon Veto

The 4π photon rejection capability of the E787 detector is fulfilled via two main electromagnetic calorimeters: one is the Barrel Veto (BV) which surrounds the Range Stack, and the other one includes two End Caps (EC) which cover the front and back faces of the cylindrical drift chamber. Roughly, $\frac{2}{3}$ of the coverage is obtained from the BV and the rest is due to the EC's. Together the subsystems achieve a $< 10^{-5}$

inefficiency in detecting the $K_{\pi 2}$ γ 's.

3.5.1 Barrel Veto

The Barrel Veto (BV) is 1.90 m in length and covers 2π in azimuth outside the RS. It consists of 48 sectors and 4 layers. Each layer is formed with alternating sheets of lead (1 mm thick) and BC408 scintillator (5 mm thick). The four layers in each sector are made up of 16, 18, 20, and 21 Pb-scintillator sheets. Each sector is slightly skewed with respect to the radial direction in order to prevent the escape of a photon through the inert gaps between adjacent sectors (Figure 3.6). Along the radial direction, the BV is 14.3 radiation lengths thick. The signals from the EMI 9821KB PMT's at each end of the counters are passively split and delivered to ADC and TDC systems as well as an energy-sum unit serving the trigger.

3.5.2 End Caps

Located downstream and upstream from the Drift Chamber are the two End Caps (EC's). They consist of lead-scintillator sheets perpendicular to the detector's axis. Each EC is segmented into 24 azimuthal modules containing 66 petal-shaped lead and NE104 scintillator layers. The systems provides 12.4 radiation lengths along the path of the photons emanating from the target.

The transport of the scintillation light from the petals in each module is made via wave shifters. A 6.5 mm-thick acrylic doped with Bicron's fluorescent BBOT absorbs and re-emits the scintillation photons within 1.6 nsec. The well-matched NE104 and

BBOT modules produce $\sim 8-10$ photoelectrons at the EMI 9954KB PMT's per MeV deposited in the EC. The 24 modules in each EC are enclosed in a welded $700 \mu\text{m}$ thick stainless steel frame. As with the BV, the PMT signals from the PMT's are received by the ADC, TDC and trigger's energy-sum units.

3.6 Trigger

In the search for very rare kaon decays, it is vital to implement efficient on-line event selection. The E787 trigger involves several stages of sophistication and hence decision-making time. The number of stages for the $\pi\mu\mu$ trigger is two: level 0 and level 1. The two levels have ~ 40 nsec and $2 \mu\text{sec}$ of dead-time, respectively. This means that while an event is being examined by a particular level of the trigger, the signals from any other incoming kaons are ignored until a decision is reached. At level 0, a failure of the event to satisfy all the parallel triggers for several decay modes will immediately free the trigger to look at the next event. However, if the examined event passes any one of the conditions, then an additional dead-time signal is generated, prohibiting the examination of further events until a decision by the level 1 is reached.³

3.6.1 Level 0

³If the event qualifies for some other decay modes, such as $\pi\nu\bar{\nu}$ or $\pi\gamma\gamma$, then further checks will be done by yet higher levels of the trigger.

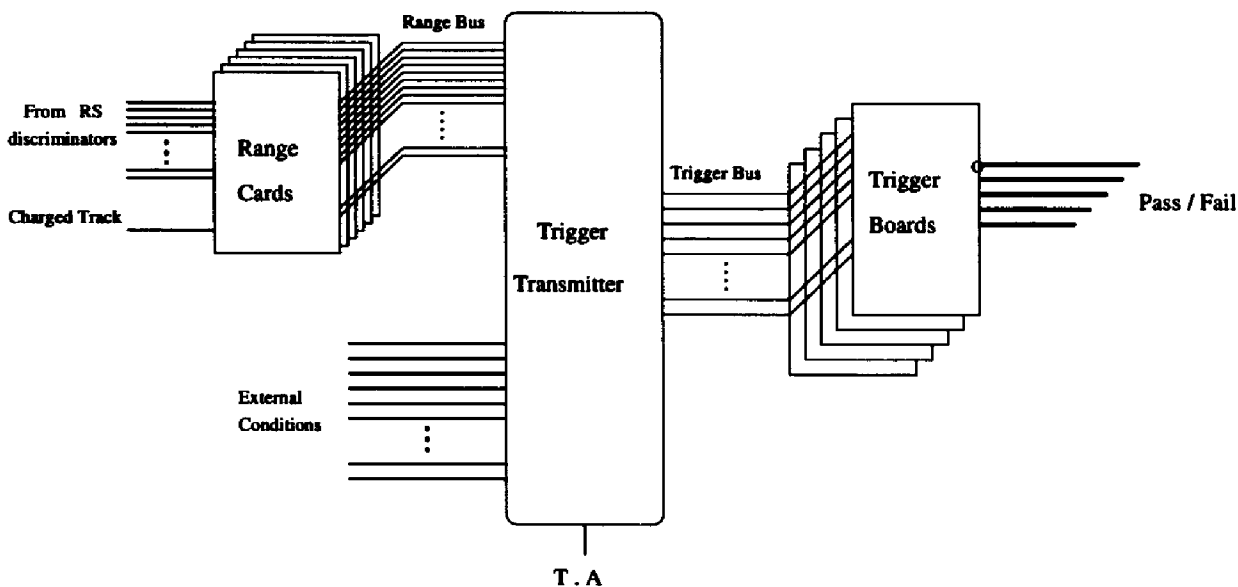


FIG. 3.8: Block diagram of the level 0 trigger.

Figure 3.8 shows a schematic of the level 0 trigger. Each Range Card (RC) receives discriminated signals from the two ends of all layers of one sector of the Range Stack. By ANDing the (T_+ AND T_-) and (A_+ AND A_-) signals (where + and - refer to the upstream and downstream ends of a counter) the module creates a $T \cdot A$ pulse. It should be mentioned that (A_+ AND A_-) is formed on a separate board, called a mean timer, explained below. In addition, the two signals at each end of other layers are also ANDed together to represent a valid hit in that counter. Such a signal is called “ungated” as opposed to pulses that are gated by a “charged track” pulse. The presence of a $T \cdot A$ in a given sector, or any of the two clockwise sectors (looking from downstream), defines the entrance of a charged particle into the RS. Therefore, the $T \cdot A$ output of each RC is delivered to the adjacent two RC’s as a *charged track* signal. This allows tagging hits at each layer as being associated with a charged particle contrary to, say, a photon converting inside the RS.

It should be noted that clockwise is the appropriate direction for a *positive* track in the presence of the magnetic field. This definition accommodates the positive charge of most of the particles from kaon decays. However, in $\pi\mu\mu$ it means that if a negative particle crosses from the entering sector into an adjacent one, the lit layers in the new sector will not be tagged as charged track hits.

The corresponding signals from the 24 Range Cards are ORed together as they are presented onto the Range Bus. These pulses are then delivered to the Trigger Transmitter (TT). In conjunction with additional logic pulses from other sources, the Range Bus signals are latched on the TT according to a separate $T \cdot A$ strobe. The $T \cdot A$ in this case comes from a set of three mean-timers (MT). Each MT, serving 8 sectors, forms the AND of $(T_+ \text{ OR } T_-)$ and $(A_+ \text{ AND } A_-)$ signals for one third of the RS (see Figure 3.9). The combination of the A pulses are performed in such a way that the time of the leading edge of the resulting signal occurs at the average time of the A_+ and A_- pulses. Thus the timing of the A_{MT} pulse is not sensitive to the longitudinal position of the particle in the A-counter.

In addition to the ungated and charged track signals obtained from the the Range Bus, the Trigger Transmitter receives additional signals from other detectors. An example of another type of conditions is the delayed coincidence. In order to ensure the kaon's decay at rest in the lab frame and within the fiducial volume of the target, it is required that at least 2 nsec pass between when the kaons enter the target and when a decay product leaves a trace in any of the I-counters. This online condition, which is reinforced in the offline analysis as well, imposes a $1 - \exp(-2./12.4) = 15.0\%$

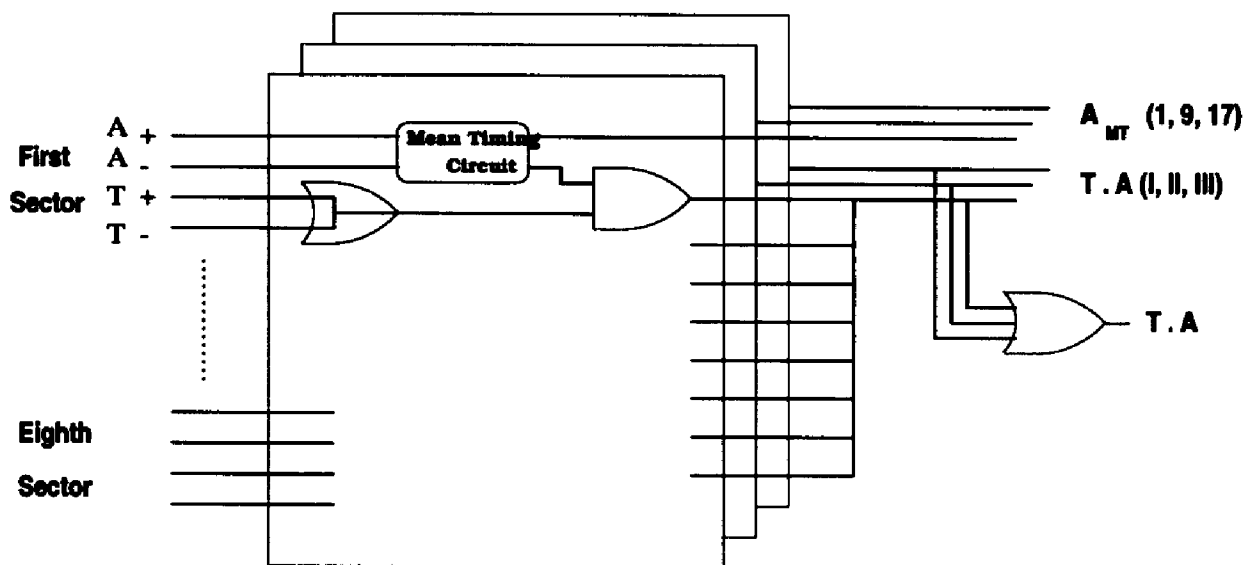


FIG. 3.9: Block diagram of the Mean Timers.

loss of efficiency in detecting any kaon decays ($\tau_{K^\pm} = 12.4$ nsec).

Level 0 for $\pi\mu\mu$ is defined as:

$$\text{Level 0} \equiv (T \cdot A) \cdot K_T \cdot \text{DelCo} \cdot (2T.A's + 3T.A's) \cdot \\ \frac{(C_{CT} + 11_{CT} + 12_{CT} + 13_{CT} + 14_{CT} + 15_{CT} + 16_{CT} + 17_{CT} + 18_{CT})}{(19 + 20 + 21 + BV + ECM + ECP)}$$

where,

$T \cdot A$ = a coincidence between a T-layer and an A-layer in the same sector.

$$K_T = \check{C} \cdot B4 \cdot E_{TG}$$

$$\check{C} = \text{Kaon Čerenkov}$$

$E_{TG} = \sim 0.5$ MeV or more energy in the target

$N_{CT} = \sim 0.5$ MeV or more energy in layer N in the sector that contains a T.A or in any of the two clockwise sectors (looking from downstream)

DelCo = ~ 2 nsec or more between K_T and the earliest hit in an I-counter

BV = ~ 5 MeV or more energy in Barrel Veto

ECP = ~ 10 MeV or more energy in the downstream End Cap

ECM = ~ 10 MeV or more energy in the upstream End Cap

As soon as an event passes the level 0 $\pi\mu\mu$ trigger, the trigger board issues a 50 nsec-long interim inhibit (DT, for Dead Time) signal to the TT which freezes the trigger bus. This allows the LEVEL 0 PASS signal to propagate through a prescaler board. For the rare-decay triggers such as $\pi\nu\bar{\nu}$ and $\pi\mu\mu$ the prescaling factor is set to 1; however, the module allows occasional (up to 1 in 2^{20}) recording of frequent decay modes such as $K_{\mu 2}$ and $K_{\pi 2}$ for monitoring purposes. If passed, the prescaler then extends the DT signal to 2 μ sec and initiates the level 1 trigger.

3.6.2 Level 1

The level 1 trigger deals with relatively more elaborate conditions in the detector whose examination takes more time than the level 0 allows. ⁴ In most cases, a

⁴In a recent upgrade of the trigger system, all of the existing level 1 conditions were moved to level 0.

Memory Look-up Unit (MLU) is used to search for a certain geometrical pattern in the event. The level 1 trigger for $\pi\mu\mu$ is defined as:

$$\text{Level1} \equiv (N_{\text{TG}} > 20) \cdot [(\#\text{IC} > 2) + (\#\text{IC}_{\text{clusters}} > 1)] \cdot \left(\sum_{\text{analog}} [C+11+12+13] < 5. \text{ MeV} \right)$$

where,

N_{TG} = Number of Target elements with $> \sim 0.2 \text{ MeV}$

$\#\text{IC}$ = Number of I-counters with $> \sim 0.2 \text{ MeV}$

$\#\text{IC}_{\text{clusters}}$ = Number of clusters of adjacent I-counter hits

According to a Monte Carlo study, the number of target elements for τ decays ($K^+ \rightarrow \pi^+\pi^+\pi^-$) peak around 17 whereas the $\pi\mu\mu$ decays light about 27 elements. Also, the number of I-counters in a τ decay is rarely more than one whereas the more energetic daughter particles in a $\pi\mu\mu$ decay hit two or more I-counters.

Due to a trigger problem in 1990 and 1991, the 4th I-counter was not contributing to the number of IC modules or clusters. The effect of this glitch on the trigger efficiency is discussed in Section 4.2.2.

Chapter 4

Analysis

The data for this study were collected during 1989, 1990, and 1991 at Brookhaven National Laboratory. The $\pi\mu\mu$ triggers consist of a total of ~ 5.2 million events which were later on separated from the other triggers and written onto forty 8-mm VCR tapes.

4.1 Analysis Strategy

To understand the topology and kinematics of $\pi\mu\mu$ events in our detector, a large number of these decays were generated by the experiment's Monte Carlo simulation program, UMC. The first goal was to estimate the trigger efficiency by applying the online requirements to the simulated events and recording the ones that pass the level 0 and 1 conditions. In such cases, UMC digitizes the energy deposition and timing information similar to the actual ADC's and TDC's. This information is then written out in data banks in the same format as the one used by the data acquisition system.

These simulated events can be analyzed with the same analysis code run on the data.

The trigger acceptance for $\pi\mu\mu$ events is 10.9%.¹ The most important requirement a signal event needs to satisfy in order to be accepted is the two- or three-T·A condition. Recall that the E787 detector has been specifically designed to detect the $\pi\nu\bar{\nu}$ decay in the kinematic region between the $K_{\pi 2}$ and $K_{\mu 2}$ two-body decays. The momentum and range of a pion in this region are around 225 MeV/c and 37 cm, respectively. The magnetic field of 1 Tesla and the amount of scintillator traversed by such pions in the Target are optimized for the detection of a $\pi\nu\bar{\nu}$ pion.

In a $\pi\mu\mu$ decay, the available 142.76 MeV kinetic energy has to be shared by three charged particles all of which will undergo dE/dx losses in the Target plus bending by the magnetic field. As a result, it becomes unlikely for any one of the decay particles to have enough momentum to reach the Range Stack after traversing the Target. Clearly, it is even more unlikely for two or three tracks to get to the RS. According to UMC, 52.5% of $\pi\mu\mu$ events have at least one T·A, and only 16.0% include two or three.

Further studies of the events that survive the trigger revealed that it is very improbable for the softest track to leave the Target. In the events that satisfy the trigger, a large fraction of the total available kinetic energy Q is carried away by the two tracks that give the T·A's. Typically, each of them has a kinetic energy of about 60 MeV in order to make it to the RS. This of course depends on where inside the Target the K^+ decays. If any of the two most energetic daughter particles leaves the

¹In 1990 and 1991 the acceptance was 7.5% due to a hardware problem (see Section 4.2.2).

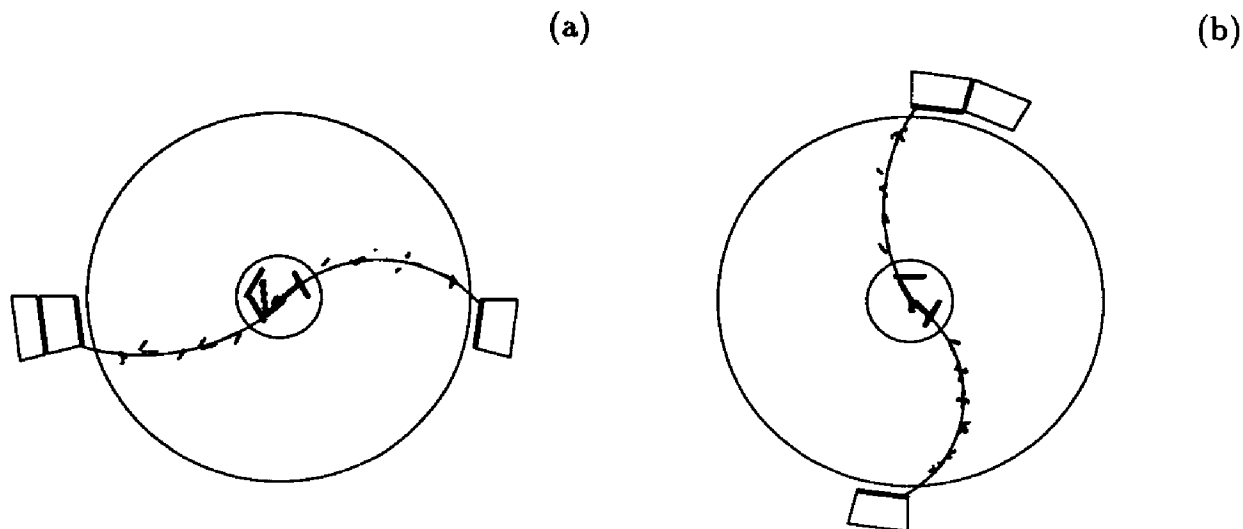


FIG. 4.1: Examples of typical $\pi\mu\mu$ events.

Target without traversing a long path in the scintillator, then it can have a lower energy. In this case, the third particle is left with a relatively larger share of Q ; however, conservation of transverse momentum forces it to have a longer path inside the Target (see Figure 4.1a). On the other hand, if either or both of the two most energetic particles go through larger paths inside the Target before leaving it then they must have received a larger share of the Q -energy hence leaving the third particle with a much lower portion (Figure 4.1b). In both cases, it becomes very difficult for the softest particle to survive after its heavy ionization of the scintillator and thus to leave the Target.

According to UMC, the above scenario happens to 90% of the $\pi\mu\mu$ events that pass the trigger. In the remaining 10%, the softest track may still not be able to travel far inside the Drift Chamber due to the magnetic field.

Several modifications were needed to the existing DC tracking and fitting program which was originally written for the single-track higher-momentum particles of inter-

est to $\pi\nu\bar{\nu}$ analysis. The modifications to the code were designed to accommodate low-momentum multi-track events. These tracks could have certain characteristics including:

1. traversing adjacent cells in each layer,
2. generating larger number of total hits,
3. bending inwards within the Drift Chamber,
4. reaching only the first or second layer,
5. crossing other tracks, and
6. deviating from a circle because of dE/dx losses and multiple scattering in the chamber gas.

These modifications resulted in a $\sim 50\%$ increase in the efficiency of finding three tracks (from 60% to 90%). However, the fact remains that no more than 10% of the events have a third track in the DC. In addition, the fitting of the third track, particularly the longitudinal component of it, becomes inaccurate due to a low resolution. One reason is the deviation of the track from a circle and consequently the inaccuracy in calculating the positions of the stereo hits. The other reason is adjacent-cell crossing by low-P tracks. In this situation, the simple drift model for converting the TDC information into position becomes inaccurate since the ionization electrons coming from the corners of a cell have longer and more complicated paths before reaching the sense wires.

It becomes clear that requiring a momentum measurement for all three daughter particles in a $\pi\mu\mu$ decay introduces a heavy loss of offline acceptance in the very beginning. Therefore, the possibility of an analysis mostly based on the two energetic

tracks was considered. The idea is to extract as much information as possible from the better-measured values of energy and momentum for these tracks plus using other event reconstruction techniques in order to eliminate the sources of background.

The first step is to demonstrate that the two tracks originated from a stopped kaon in the Target. Electric charge conservation then demands the existence of a third charged particle in the event. Sufficient photon and long-range electron rejection can highly suppress the backgrounds due to π^0 Dalitz decays ($\pi^0 \rightarrow \gamma e^+ e^-$) or photon-conversions near the kaon vertex. At this point, the only major sources of three-charged tracks are $K^+ \rightarrow \pi^+ \pi^+ \pi^-$ (τ), $K^+ \rightarrow \pi^+ \pi^- e^+ \nu_e$ (K_{e4}) $K^+ \rightarrow \pi^+ \pi^- \mu^+ \nu_\mu$ ($K_{\mu 4}$), and the $\pi \mu \mu$ decays.

4.2 Monte Carlo

Event simulation in the E787 detector is carried out by a Monte Carlo program called UMC. It includes detailed geometrical and physical information about the major subsystems of the detector. The propagation of the particles through the detector is simulated by following the path of each particle step-by-step while allowing various possibilities (*e.g.* scattering, interactions, decaying, *etc.*) based on their corresponding probability distributions.

As a first step in an event simulation, a K^+ is positioned within the Target according to the measured real beam distribution. The kaon is then pulled back and allowed to propagate through the Target with an initial 50 MeV of kinetic energy. In the code, the kaon can be required to decay only in a particular channel, say $\pi \mu \mu$. The

decay products will be given random four-momenta while obeying the corresponding conservation law and the expected distributions from phase space alone or along with the decay matrix element if known. Each daughter particle is separately propagated within the detector until it stops, decays, leaves the detector, or annihilates in a nuclear interaction. At that point the next particle at the top of the “particles stack” will propagate.

The trigger simulation routine can be invoked at any time during the program to examine the online selection requirements. This allows speeding up studying of the rare processes by vetoing the events as soon as the event is bound to fail a trigger condition.

4.2.1 Energy and Time Smearing

Care must be taken in various calibrations and time windows when the UMC events are being analyzed. The energy and time resolutions in various subsystems are too perfect in UMC. These quantities were smeared by appropriate Gaussian functions in order to simulate the measured resolutions. For this analysis, this task was done as the recorded banks were unpacked into physical quantities. For RS and TG modules, a Gaussian smearing² is applied based on the photostatistics of the module [16]. The equation is

$$E_{\text{Smeared}} = E_{\text{Raw}} + \sqrt{\frac{E_{\text{Raw}}}{N_{\text{p.e.}}}} \cdot \omega$$

²This was shown to be indistinguishable from a Poisson smearing.

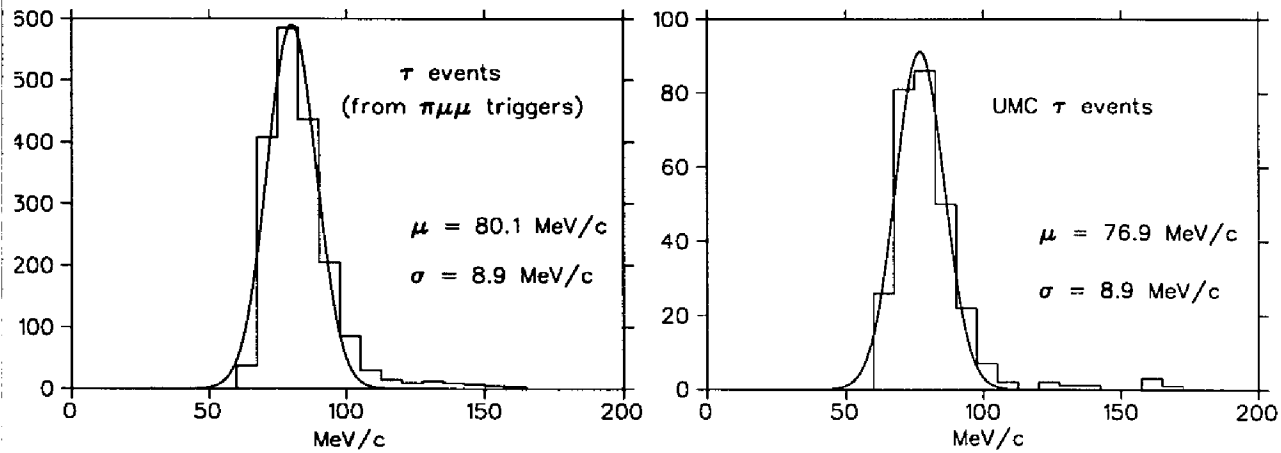


FIG. 4.2: Pion momentum distribution in real and UMC-generated τ decays that satisfy the $\pi\mu\mu$ trigger. The narrow range of their momentum allows a Gaussian fit in order to compare the two resolutions.

where $N_{p.e.}$ is the number of photo-electrons per MeV for the module and ω is a random number drawn from a normal distribution.

It turns out that photoelectron smearing of the RS energy is not enough to simulate the resolution of the π^+ and μ^+ mass plots. It could be conceived that the discrepancy is due to differing momentum resolutions. However examination of the momentum distributions of the real and UMC-generated τ events indicate otherwise. The τ pions need to almost equally share the available Q-value in order to satisfy the $\pi\mu\mu$ trigger. Therefore, their momenta are within a narrow band. Assuming a Gaussian shape, the widths of the distributions for the real and UMC data were measured (Figure 4.2). The results show that the UMC closely simulates the momentum resolution σ_P for the low-P tracks as this value is dominated by multiple scattering in this range.

It is therefore clear that the source of discrepancy in mass resolutions is the RS energy. To obtain similar widths for UMC as in the data, an additional smearing according to an empirical function is performed. The goal here was to simulate the

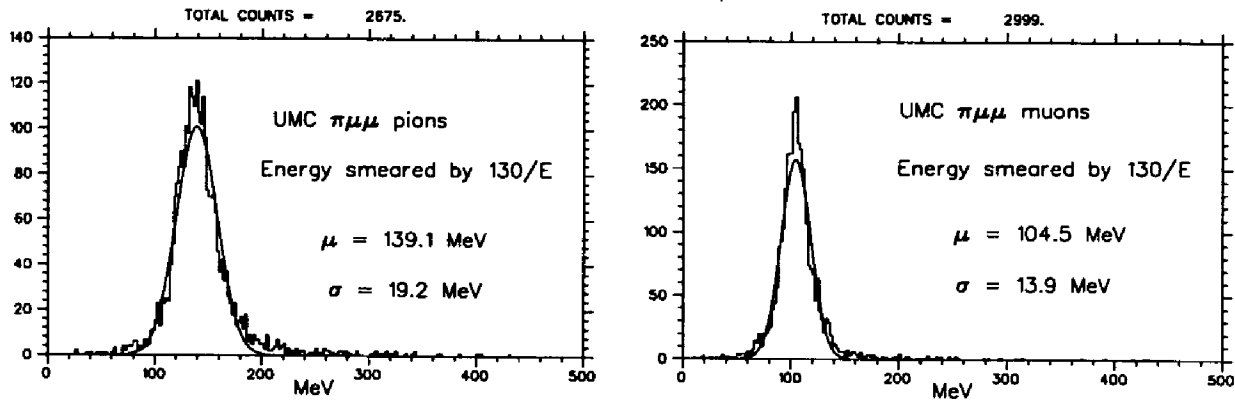


FIG. 4.3: The π^+ and μ^+ masses of UMC $\pi\mu\mu$ events. The Monte Carlo banks were used to identify the particles in each track. In addition to RS photoelectron statistics, a smearing of $130 \text{ MeV}/E_{RS}$ is applied.

widths of both the π^+ and the μ^+ masses using the same function. This was achieved through smearing by $(130 \text{ MeV})/E_{RS}$. Figure 4.3 shows the results.

It is also important to notice that the UMC-generated events nominally do not suffer from accidental hits in various subsystems as these hits are usually due to activity related to previous events or random hits in the detector.

4.2.2 Signal Simulation

Generation of the $\pi\mu\mu$ particles in UMC was based on chiral perturbation theory's parameter $w_+ = 0.89$ for the $K^+ \rightarrow \pi^+\ell^+\ell^-$ decay [7]. Out of the three decay products, the behaviors of π^+ and μ^+ are very well known and implemented in UMC due to the importance of $K_{\pi 2}$ and $K_{\mu 2}$ decays in the $\pi\nu\bar{\nu}$ search. The third particle, μ^- is treated very similar to a μ^+ in its propagation and decay. But a muon capture is *not* simulated in the UMC. This indeed does not pose any major problem since, as described in 4.4.1, the μ^- lifetime in Carbon is still about $2.0 \mu\text{sec}$ — much larger

than the widths of the ADC gates. In other words, only 10% of the stopped muons undergo a capture before they decay (a decay is simulated) and only 4% of these captures occur within the first 80 nsec seen by the ADC gates. One can neglect this 0.4% of the μ^- that are not properly simulated by UMC.

The trigger acceptance is measured through UMC by simulating the online pulse widths and energy thresholds and reconstructing the logical conditions. It was found that in the beginning of the 1990 run a small hardware problem caused the disconnection of the 4th I-Counter from the level 1 IC-pattern recognition module [18]. This problem imposed a large loss of $\pi\mu\mu$ acceptance. This was also simulated in UMC yielding the online acceptance for the 1990 and 1991 data. The results of trigger simulation for $\pi\mu\mu$ events are shown in Table 4.1

Notice that in the UMC trigger the "delayed coincidence" simply requires hits in the I-counters. It does not simulate the actual condition which compares the time separation between the IC and the Čerenkov hits. Thus, the true online trigger acceptance for the $\pi\mu\mu$ events is lower than the values in the last row of Table 4.1. Approximation can be made by requiring that the kaon lives more than 2 nsec in the UMC trigger simulation. This yields an overall trigger acceptance of 0.109 ± 0.001 for 1989 and 0.075 ± 0.001 for 1990/1991. However, the exact delayed coincidence acceptance will be determined from the actual data in each year.

Level 0 Conditions	Events surviving	
Number of stopped kaons	95107	
KT	95043	
2 or 3 T·A	14999	
“Delayed Coincidence”	14957	
$(C_{CT} + 11_{CT} + \dots + 18_{CT})$	14469	
$(19 + 20 + 21)$	14438	
\overline{LOBV}	14434	
$\overline{LOECM + LOECP}$	14423	
Level 1 Conditions	Events surviving	
$N_{TG} > 20$	13380	
I-counter pattern cut	12212	8383
$\Sigma(C + 11 + 12 + 13) < 5 \text{ MeV}$	12086	8304
Acceptance	0.127 ± 0.001	0.087 ± 0.001

Table 4.1: Acceptance for $\pi\mu\mu$ trigger for the 1989 and also 1990/1991 data. Note that the “Delayed Coincidence” in UMC simply requires a hit in the I-Counter.

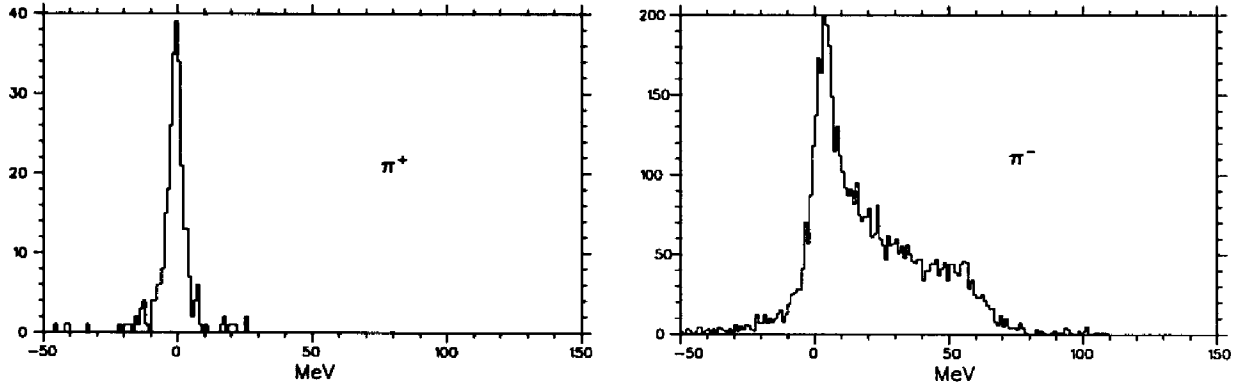


FIG. 4.4: Excess energy in the RS stopping counter for π^+ and π^- tracks.

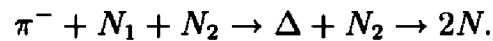
4.2.3 Background Simulation

Among the decay products of the major backgrounds to $\pi\mu\mu$, *i.e.*, the K_{e4} and τ decays, only the π^- was not properly handled by the existing code. A study of the behavior of this particle was needed for an appropriate simulation of the background. The presence of ample τ decays both in the $\pi\mu\mu$ and $\pi\nu\bar{\nu}(2)$ triggers provides a useful source for studying the π^- . The empirical distribution of a stopped π^- energy deposition, along with several published measurements, was used in implementing a simple model for the stopped π^- .

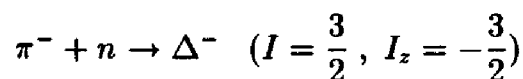
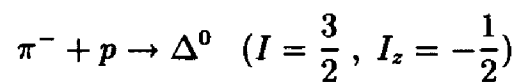
Figure 4.4 shows the measured excess energy E_{exp} deposition for both the π^+ and π^- in the RS. E_{exp} was calculated based on the measured momentum of the pion in the DC. These pions were selected from the distinct τ peak in the Pass2 output (Figure 4.8) with additional dE/dx cuts applied in the DC in order to reject any electrons from π^0 . The figures clearly indicate the difference between a positive and a negative pion. In the case of a π^+ , after it loses all its kinetic energy a (π^+, e^-) atom is formed until the pion decays. However, a slow π^- is immediately captured by a

nucleus to form an atom. The typical time for this process is less than 1 nsec [21]. During this time X-rays and Auger electrons are emitted. Both their energies however are below the ADC threshold leaving them undetected. The pionic atoms are mostly formed with a C nucleus as the capture rate is proportional to Z^3 [22]. The line width Γ_{1S} for a π^- absorption by ^{12}C nucleus in a pionic atom is 2.88 KeV [23] making the lifetime for this transition 2.3×10^{-19} sec. In other words, the absorption of a stopped π^- in the scintillator happens instantaneously in the experiment's time scale. The exponential shape of the excess energy plot indicates the fraction of the 139.6 MeV rest mass that is deposited *locally* as a result of this process. The remaining energy is carried away by neutrons and photons.

The energy spectra of neutrons and charged particles emitted after a π^- absorption have been measured [24, 25]. Following the approach of reference [24] the π^- capture by a finite nucleus is, in first approximation, considered similar to pion capture by an alpha particle. In this model the pion capture occurs as



Hence it is assumed that the pion is absorbed by a pair of nucleons as in a deuteron nucleus. The actual interaction however is with either a proton or a neutron. These reactions are



$$\pi^- + N_1 + N_2 \xrightleftharpoons{(\sigma)} \Delta + N_2 \xrightleftharpoons{(\sigma')} 2N$$

$\Delta + N_2$	resulting pair	No. N_1	Relative σ	No. N_2	Relative σ'	Net Number of channels
$\Delta^0 + n$	nn	2	1	2	1	4
$\Delta^0 + p$	np	2	1	1	2	4
$\Delta^- + p$	nn	2	3	2	3	36

Table 4.2: Relative rates for nn or np direct production in a pion capture. The relative cross sections are calculated from isospin Clebsch-Gordon coefficients.

The relative rates can be calculated based on the relative cross sections for the above interactions, the corresponding isospin Clebsch-Gordon coefficients, and the possible numbers of N_1 and N_2 . These values are tabulated in Table 4.2. Therefore,

$$\text{Relative number of processes yielding two neutrons} = 40$$

$$\text{Relative number of processes yielding a neutron and a proton} = 4$$

Thus the average numbers of "direct" neutrons and protons are:

$$\langle N_n^{\text{direct}} \rangle = \frac{2 \cdot 40 + 1 \cdot 4}{40 + 4} = 1.91$$

$$\langle N_p^{\text{direct}} \rangle = \frac{1 \cdot 4}{40 + 4} = 0.09$$

The 1.91 value for $\langle N_n^{\text{direct}} \rangle$ is consistent with the measured number 1.74 ± 0.28 .

As the two nucleons fly away after the capture, they excite the other nucleons within the Carbon atom. This results in the emission of additional low-energy neutrons,

protons, and other light nucleons [25]. The process is known as *nuclear evaporation*. After these collisions the two direct nucleons carry away 75.6 ± 4.8 MeV of the pion's rest mass energy. The remaining energy is received by the evaporation products. It should be noticed that each nucleon's removal costs about 8 MeV. Therefore, the process continues until the available energy drops below the 8 MeV threshold.

In the UMC model, a pair of nucleons are first generated as the π^- comes to rest. These nucleons (95.5% of the times a nn pair and 4.5% of the times a np pair) each carry about 37.8 ± 3.39 MeV kinetic energy. The rest of the pion rest mass is then passed to a nuclear evaporation routine which generates p and n as they penetrate the potential barriers at the surface. Notice that the model is not able to generate all the charged products of a π^- absorption such as d , t , ${}^4\text{He}$, and ${}^3\text{Li}$. Nevertheless, the low energy protons created by the evaporation routine can more or less simulate the local energy deposition of these slow nucleons. Finally, as the available kinetic energy drops below the 8 MeV threshold, the model crudely generates one or two 4 MeV photons to take into account the gamma rays after evaporation is no longer possible.

4.3 Pass2

Pass1 was an attempt to reduce the size of the data via achieving high rejection through a very conservative analysis code. The remaining events were written onto nine 8-mm tapes. The Pass2 code was an extension of Pass1 with some cuts made tighter and with complete two-track reconstructions in the TG-RS-DC. Therefore, the following discussion will entirely refer to the Pass2 code which already includes

Pass1.

The main goals of Pass2 were:

1. Establish the presence of a stopped kaon in the Target.
2. Efficient photon/electron vetoing.
3. Track reconstruction in the TG-DC-RS systems.

4.3.1 Target Analysis

There are several requirements to be satisfied by an event for a successful reconstruction of the decay in the Target. The essential feature of the target analysis code (called SWATH) is to use an extrapolation of the DC tracks back into the TG. Here the track is required to run through some "kaon blob" defined as a cluster of triangles with prompt TDC timings (with respect to the kaon Čerenkov time) and relatively high ADC values (characteristic of a heavily ionizing kaon coming to a stop as it travels along the z-axis). The next step is to identify the triangles traversed by the decay particles. Due to the delayed coincidence requirement at the trigger level, these elements have later TDC hits. They also have lower ADC values since the T.A requirement restricts the decay products to travel transversely while almost minimally ionizing. In addition to the energy and time of the triangles, their proximity to the extrapolated DC track is also used to identify the Target-track elements. A likelihood calculation based on the three pieces of information provides the deciding factor [17]. In this method, the distributions of energy, time, and distance to the DC track

are used for assigning to each candidate triangle likelihoods of belonging to a "pion track".³ The product of these likelihoods is then calculated and cut on.

In the $\pi\mu\mu$ triggers, care should be taken in the above procedure since the triangles from other trajectories might be close enough to a given track and be considered as candidates. Also the heavily ionizing third particle, which usually stops in the Target, might have too much energy and thus look like a kaon blob especially if the kaon decayed early. The code tries to distinguish such cases.

The above procedure is repeated for each DC track. First, any one of the RS-DC matches is required to have a kaon blob and a pion track. Next, the time-difference between the pion and kaon tracks is calculated. This time must be greater than 2.0 nsec to reinforce the trigger delayed coincidence requirement. This is designed to eliminate the in-flight decays of the kaon and hence to allow the kinematic study of the decay.

In order to establish the fact that the K^+ produced at least two charged particles, it is required that the same kaon triangles be found independently for both (or all) extrapolated DC tracks. Therefore $K_{\pi 2}$ decays of two simultaneous kaons, for example, can be eliminated.

As mentioned earlier, photon conversion from a $\pi^0 \rightarrow \gamma\gamma$ decay is a major source of background in the $\pi\mu\mu$ trigger. Most of the conversions happen in the Target thus satisfying the level 1 requirements in the trigger. In order to reduce the number of such events, connectivity between the pion track cells and the kaon blob as well as

³"Pion track" is used as a generic name. It refers to the tracks in the Target caused by decay pions, muons, or electrons.

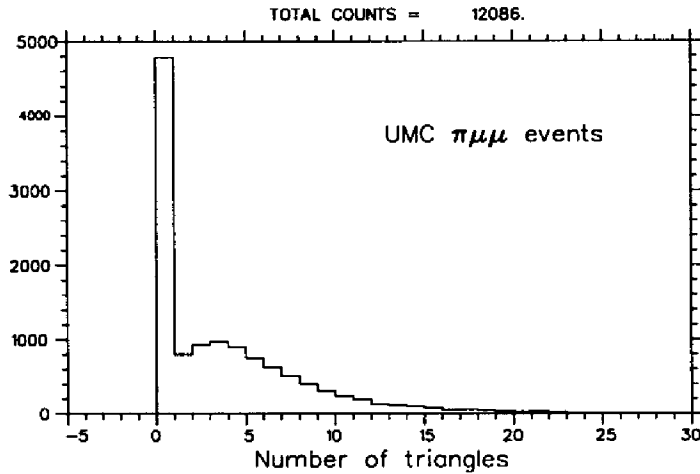


FIG. 4.5: Distribution of the number of TG triangles in the third track for the UMC-generated $\pi\mu\mu$ events. Some single-cell tracks were missed by the Target routine resulting in the dip above the spike.

continuity of hit cells along each one of the pion tracks is required.

It is possible for the pion triangles near the kaon blob to initially be assigned to more than one extrapolated DC track. Once the event has successfully passed the above requirements for individual tracks, the common pion cells are re-assigned only to the track they are closest to.

After the pion cells associated with the DC tracks are identified, there is an attempt made to find all the triangles whose TDC times are consistent with the pions'. These are usually the cells along the track of the third particle, although they might sometimes be due a showering photon. In $\pi\mu\mu$ events that pass the trigger, the number of such triangles for the softest track is small on the average. Figure 4.5 shows their distribution for UMC events. These cells are grouped into clusters. Events with more than five such clusters are vetoed as they indicate a showering photon. In the remaining events, these clusters represent the "stub" left by the third track.

4.3.2 Photon and Neutron Rejection

The largest contribution to $\pi\mu\mu$ triggers comes from $K_{\pi 2}$ decays in which the π^0 undergoes either a Dalitz decay ($\pi^0 \rightarrow \gamma e^+ e^-$) or a $\pi^0 \rightarrow \gamma\gamma$ decay followed by a photon conversion ($\gamma \rightarrow e^+ e^-$) in the TG, DC, or the T-counter. The second largest source of $\pi\mu\mu$ triggers are $K_{\mu 3}$ decays ($K^+ \rightarrow \pi^0 \mu^+ \nu_\mu$) followed again by a photon conversion or a Dalitz decay. In such cases, the two- or three-T-A requirement is easily satisfied. The remaining photon may not always be vetoed by the other trigger conditions because of high energy thresholds or timing mismatches. Another source of a large isolated amount of energy in the detector is the neutrons from the nuclear absorption of a π^- . These are abundantly produced by the τ as well as the rarer $K_{e 4}$ decays.

In Pass2, any amount of energy in the BV, EC, or outer layers of the RS (layers 11 through 21) greater than 1.0 MeV causes the event to be rejected. In addition, the presence of energies larger than 1.0 MeV in the inner layers of the RS, not associated with a DC track, is also considered as originated by a photon or neutron. Since rates are high in all of the detector subsystems, it is important to adjust the time windows within which the energy is measured, so that accidental hits cannot cause too much inefficiency. The half-width of the time windows and the positions of their centers (i.e. their offset) with respect to the T-A time have been determined based on the time distribution of the largest-energy module in each subsystem in $\pi\mu\mu$ triggers. The code, called INTIME, used the values tabulated in Table 4.3.

	Subsystem	Barrel Veto	End Cap	Range Stack
1989	offset	1.4 nsec	2.3 nsec	0.6 nsec
	window	5.0 nsec	6.0 nsec	3.5 nsec
1990	offset	0.4 nsec	0.5 nsec	0.4 nsec
	window	5.0 nsec	6.0 nsec	3.5 nsec
1991	offset	2.0 nsec	2.0 nsec	0.3 nsec
	window	5.0 nsec	6.0 nsec	3.5 nsec

Table 4.3: Time offsets and window half-widths used by the code INTIME.

4.3.3 Electron Rejection (in Pass2)

In addition to vetoing photons, one can try to detect electrons and subsequently reject the event. This is basically achieved by detecting large energies in the RS. The $\pi\mu\mu$ trigger already rejects electrons that penetrate deep inside the RS. In the Pass2 code, the total “INTIME” kinetic energy in the inner layers of the RS is restricted to less than 120 MeV. This corresponds to higher total kinetic energies for the RS-reaching heavy particles after taking into account the saturation effects (see Section 4.4.1). Considering the fact that the total kinetic energy available to all three particles in a $\pi\mu\mu$ decay is 142.76 MeV, this is a safe cut to quickly get rid of events with electrons. Figure 4.6 shows the RS energy spectrum for UMC $\pi\mu\mu$ events.

It is also possible for electrons to enter the End Cap directly from the Target or through the DC. The low-threshold cut on the INTIME energy in the EC is also a way of rejecting such electrons.

Monte Carlo studies indicate that only 0.6% of $\pi\mu\mu$ events deposit more than 1 MeV either in the BV or in the EC. These mostly have electrons coming from the

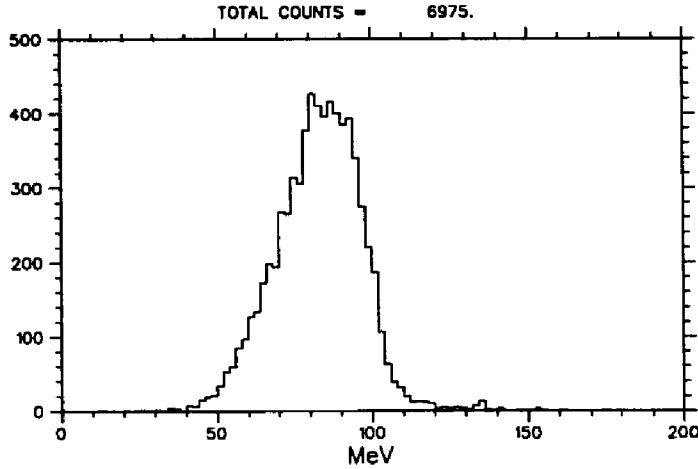


FIG. 4.6: Energy distribution in RS layers T through C for the UMC-generated $\pi\mu\mu$ events. Events with more than 120 MeV are rejected.

early decays of the muons or the pion. Within the 100 nsec gate of the ADC, 5% of the muons will decay to an electron ($\tau_\mu = 2197$ nsec). Within the same time window 98% of the pions decay ($\tau_\pi = 26.030$ nsec) mostly via $\pi^+ \rightarrow \mu^+ \nu_\mu$. This decay muon has also a chance of decaying to an electron within the ADC gate even though this chance is reduced by the pion lifetime. Such events cannot be accepted since the kinematics of the $\pi\mu\mu$ decay cannot be reconstructed based on the measured quantities; hence, it is still desirable to veto such electrons. In fact, when the π and μ decays are prevented in UMC, the number of $\pi\mu\mu$ events with more than 1 MeV INTIME energy in the EC or BV is reduced by a factor of 2.

In 0.2% of $\pi\mu\mu$ events, the softest particle can penetrate through the DC endplates, enter the EC, and deposit the rest of its energy. The very large rejection of photons and electrons achieved by vetoing on the EC energy justifies the negligible loss of acceptance for such $\pi\mu\mu$ events.

Pass2 CUTS	Estimated Rejection
2 or 3 prompt T·A	1.3
RS inner layers ($T \rightarrow C$) energy < 120 MeV	2.1
RS outer layers (11 \rightarrow 21) energy < 1 MeV	2.1
BV energy < 1 MeV	1.3
EC energy < 1 MeV	1.7
2 or 3 RS-DC matched tracks	1.6
Momentum of RS-DC tracks < 170 MeV/c	4.1
TG reconstruction	3.1
RS inner layer energy not associated with a track < 1 MeV	1.5

Table 4.4: Summary of Pass2 cuts with their estimated rejections.

4.3.4 Pass2 Output

Table 4.4 gives a summary of the $\pi\mu\mu$ Pass2. The Target reconstruction requirements are outlined in Table 4.5

Inspection of the total energy spectra of the three year data sets at this point indicated a hardware problem in the level 1 trigger condition in the 1991 data. As Figure 4.25 shows, there is an excessive number of τ surviving at the end of the 1991 Pass2. The problem was due to the slipping threshold applied to the Target discriminators sum. This threshold had fallen slightly in 1990 and considerably in 1991. Recall that the $N_{TG} > 20$ is designed to veto the τ , and the position of the cut is near the peak of the N_{TG} distribution for the τ (Figure 4.7). In the same distribution for UMC $\pi\mu\mu$, the cut appears on the low tail. Therefore, a lower threshold for N_{TG} would allow many more τ to pass the trigger while increasing the $\pi\mu\mu$ acceptance

Target Reconstruction Cuts	Estimated Rejection
2 or 3 SWATH tracks	1.8
Offline delayed coincidence	1.0
Same kaon blob associated with the tracks	1.1
Time of pion tracks within 6 nsec of each other	1.1
Maximum gap between kaon and "pion" cells < 1.8 cm	1.3
Maximum gap within "pion" tracks < 1.8 cm	1.1
Maximum gap between a "pion" track and the corresponding TG edge < 1.8 cm	1.0
Too many DC tracks through the kaon vertex	1.0
Consistent I-counter hits along the tracks	1.0
Too many disconnected energy clusters	1.0

Table 4.5: Summary of the Target-tracks requirements. Notice that most of these cuts have low rejections and are mainly used for event reconstruction.

only slightly.

The fix to the problem was based on the online number of Target elements B_NTGT used in the $\pi\nu\bar{\nu}$ trigger. Evidence suggests that the value at which the $N_{TG} > 20$ threshold was originally set corresponded to $B_NTGT \geq 9$. Hence that requirement ($B_NTGT \geq 9$) was simply added at the end of Pass2. This indeed gets rid of the excess τ observed in 1991. It also unifies the $\pi\mu\mu$ acceptance for the three years as far as $N_{TG} > 20$ is concerned.

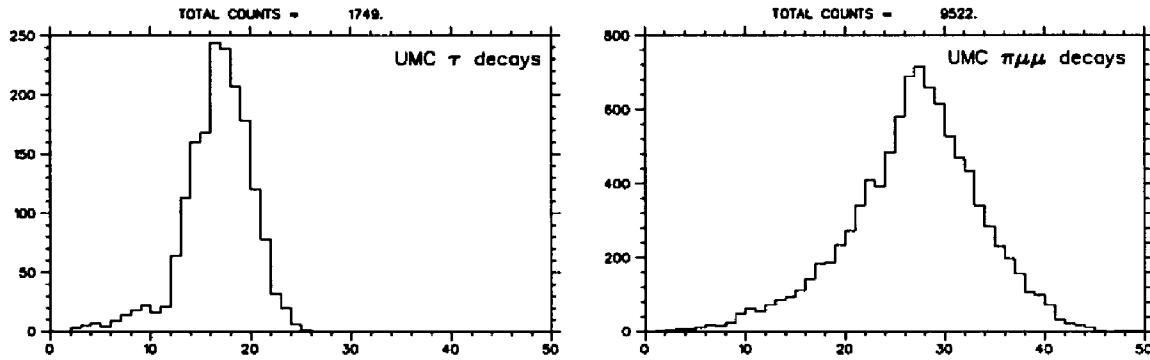


FIG. 4.7: Distribution of the number of Target elements in UMC-generated τ and $\pi\mu\mu$ events.

4.4 Pass3

The main goal of Pass3 is to extract the $\pi\mu\mu$ signal. Pass2, by design, retained parts of the main backgrounds to $\pi\mu\mu$, *i.e.*, the τ and K_{e4} ($K^+ \rightarrow \pi^+\pi^-e^+\nu_e$) decays. Pass3, on the other hand, includes particle identification cuts for rejecting electrons as well as kinematic reconstruction specifically designed for a $\pi\mu\mu$ decay. The Pass3 code was yet another extension of Pass2. The main features of the *added* code are:

1. mass measurement for the RS reaching tracks,
2. combination of charges,
3. conservation of momentum (kinematic cuts).

4.4.1 Mass Measurement

Mass measurement on the RS-reaching tracks turns out to be a very strong tool in rejecting electrons emanating from π^0 or K_{e4} . Knowing the kinetic energy K and the

momentum P of a particle, one can calculate the mass:

$$m = \frac{P^2 - K^2}{2K} \quad (\text{with } c = 1)$$

Thus, one needs to calculate the kinetic energy of the particle in the DC, where its momentum is measured. This is done by finding the total unsaturated energy deposited in the RS as the particle comes to a stop and then correcting for the energy loss in the outer wall of the DC. The very small energy loss in the DC gas can be ignored. All corrections for calculating K in the DC (where P is measured) require an assumption about the identity of the particle. Slightly different values for the mass is obtained based on given particle-id hypotheses. For each track, two masses were calculated with pion and muon hypotheses, and the mass cuts were applied to them separately.

In Pass3, two different mass cuts were applied:

1. The positive track should be consistent with a π or μ distribution,
2. The negative track should be consistent with a μ distribution.

Because of a later requirement accepting only positive RS-DC-TG tracks, the mass cut on the negative particle is unimportant in this analysis. Nevertheless, the requirement will be explained in the interest of a possible study on the events with the $+ -$ combination of tracks.

Pions

The first step in designing the mass cuts was to produce clean samples of pions and muons that behave similarly to the $\pi\mu\mu$ decay products; *i.e.*, that mostly stop in layers A and B. Pions of this nature are easily found in the Pass2 output. The total energy of Pass2 events includes a sharp peak around 75 MeV which corresponds to the Q-value of a τ decay (= $493.6 - 3 \times 139.6 = 74.9$ MeV). Due to the very low energy available to all three particles, only the τ events from a very restricted corner of the phase space can survive the trigger. They usually have two tracks which equally share most of the available Q-value in order to reach the RS leaving very little energy for the third track. In addition, the kaon needs to be close to an edge of the Target letting the two particles escape the TG before losing too much energy. But this is not enough: if the two energetic particles are both positive, then the magnetic field can force one of them to traverse a much longer path inside the Target before it can leave. Such a track may not reach the RS in order to satisfy the trigger. Therefore, most of the τ events in Pass2 output consist of a $\pi^+\pi^-$ pair (Figure 4.8). This is actually very useful for studying different aspects of both particles and for comparing and contrasting them.

The low kinetic energy of the τ pions makes them stop shortly after they enter layer A in the RS. The small amount of generated light limits the energy and mass resolution of these pions as compared to $\pi\mu\mu$ in which the pions stop in layers A and B, equally. K_{e4} decays provide a source of pions with a momentum similar to that of $\pi\mu\mu$ (see Figure 5.3). These pions were identified using FITPI (see Section 3.4.1) in

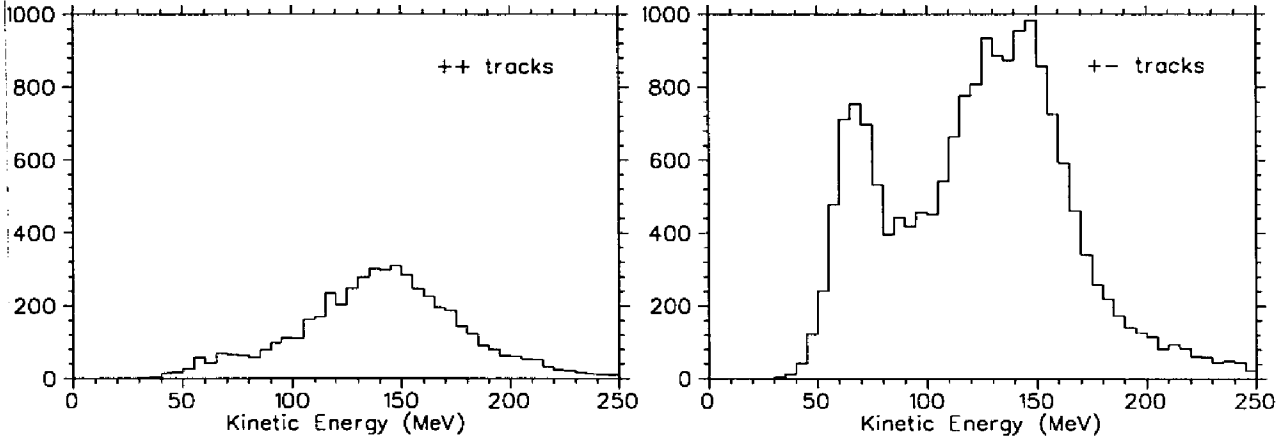


FIG. 4.8: Total kinetic energy distribution for the Pass2 output events with ++ and +- combination of charges.

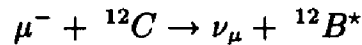
the Pass2 ++ events with $140 < E_{tot} < 200$ MeV.

As a positive pion comes to a stop in the scintillator, it forms an atom with an electron until it undergoes the $\pi^+ \rightarrow \mu^+ \nu_\mu$ two-body decay with the μ^+ carrying 4.12 MeV in kinetic energy. The heavily ionizing muon comes quickly to rest after travelling only 3 mm. Then, in turn, it forms a muonic atom with an electron until the $\mu^+ \rightarrow e^+ \nu_e \bar{\nu}_\mu$ decay occurs. The kinetic energy in a π^+ track, measured within the ADC 100 nsec gate, usually includes the $\pi \rightarrow \mu$ decay. It is therefore necessary to subtract the corresponding kinetic energy from the measured RS energy in a π^+ -track hypothesis.

Muons

The mass cuts for μ^+ and μ^- in $\pi\mu\mu$ were designed based on measurements from $K_{\mu 3}$ decays. This mode includes μ^+ that are kinematically similar to $\pi\mu\mu$ muons. Since there are no abundant sources of μ^- in our detector, the cut designed based on $K_{\mu 3}$ positive muons was also applied to any negative tracks in Pass3; hence, the

mass of each negative particle was calculated with a muon-hypothesis. As a negative muon comes to rest in the scintillator (consisting of equal numbers of Hydrogen and Carbon atoms), it has a $(\frac{Z_C}{Z_H})^3 = (\frac{6}{1})^3$ higher chance of getting trapped by a Carbon nucleus—as opposed to Hydrogen—and to form a muonic atom. Muon capture in a (C, μ) atom happens via the reaction:



The total capture rate is measured to be $(44 \pm 10) \times 10^3 \text{ sec}^{-1}$ [11]. Since the life-time for a muon decay is $2.2 \mu\text{sec}$, only $\sim 10\%$ of muons in (C, μ) atoms live long enough to undergo a capture. In fact, the effective mean life of a stopped μ^- in the scintillator is $2.020 \pm 0.020 \mu\text{sec}$. Therefore, we can safely attribute all of the measured energy in a μ^- RS-track to the stopping particle's kinetic energy. Hence a mass cut designed for positive muons can also be applied to the negative tracks.

The $K_{\mu 3}$ decays were extracted from the $\pi\gamma\gamma(2)$ trigger ⁴ after the following cuts:

1. One track consistent through Target, Drift Chamber, and Range Stack (RS-DC-TG track).
2. $P_{\text{track}} < 185 \text{ MeV}/c$ in order to reject the $K_{\pi 2}$ pions. (see Figure 4.9).
3. Two photon clusters whose invariant mass is near $m_{\pi^0} = 135.0 \text{ MeV}$.
4. A reconstructed missing mass near $m_\nu = 0 \text{ MeV}$. The reconstruction is based on

⁴ $\pi\gamma\gamma(2) \equiv (T \cdot A) \cdot K_T \cdot \text{DelCo} \cdot \text{BV} \cdot (C + 11 + \dots + 20 + 21 + \text{ECM} + \text{ECP})$.

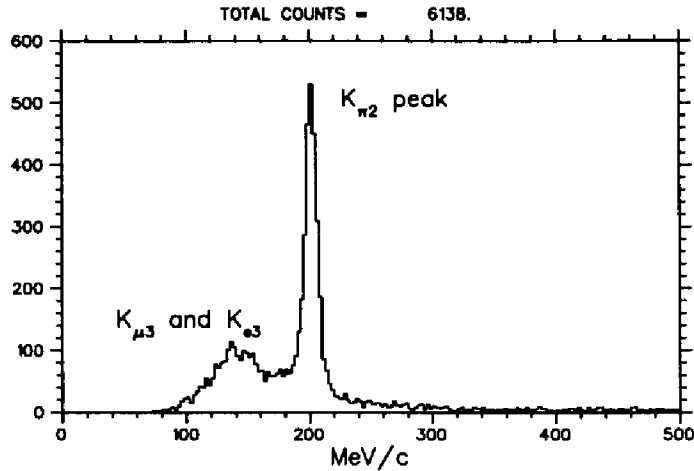


FIG. 4.9: Momentum distribution of reconstructed events in $\pi\gamma\gamma(2)$ triggers (after correction for energy loss in the Target).

the TG-corrected momentum of the track at the vertex with a muon hypothesis and using the reconstructed π^0 four-momentum.

This yielded a clean sample of low-momentum muons in the range stack.

Protons

In order to have a consistent picture for any necessary empirical corrections to the RS-energy based on the measured masses, a sample of protons was also used. These come from the following chain [12]:

$$K^+ \rightarrow \pi^+ \pi^0$$

$$\pi^+ + d \rightarrow p + p.$$

The quasi-deuterium represents the interacting nucleons within the Carbon nucleus.

The 205.1 MeV/c π^+ has a 10 mbarn cross section in deuterium for the above reaction.

The resulting protons have momenta between 384 and 589 MeV/c. Such protons also come to rest within the A or B layers in the range stack thus providing another excellent source for testing and calibrating the measured energy for low- KE particles in the RS.

Saturation

Only a fraction of the kinetic energy lost by a charged particle in a scintillator is converted into fluorescent energy [13]. The remainder is dissipated non-radiatively, primarily in the form of lattice vibrations or heat. The fraction of the energy which is converted to light (the scintillation efficiency) depends on both the particle type and its energy. The scintillator's light yield for heavy charged particles is usually smaller as compared to electrons and is also non-linear at high initial energies. This is called the *saturation effect*. The response of organic scintillators to charged particles can best be described by the *Birks' equation*. It assumes that a high amount of ionization along the path of a charged particle leads to quenching from the damaged molecules and a consequent lowering of the scintillation efficiency. Furthermore, it is assumed that in the absence of quenching the light yield is proportional to energy loss,

$$\frac{dL}{dx} = S \frac{dE}{dx}$$

where $\frac{dL}{dx}$ is the fluorescent energy emitted per unit path length, $\frac{dE}{dx}$ is the actual energy loss for the charged particle, and S is the normal scintillation efficiency. Then

in the presence of quenching,

$$\frac{dL}{dx} = \frac{S \frac{dE}{dx}}{1 + K_B \frac{dE}{dx}}$$

K_B is called the *Birks' constant* and is experimentally treated as an adjustable parameter which gives the best fit to the data. In the scintillators used in the RS, the manufacturer's specified value of the Birks' constant is 0.013. However, a reasonable value of 0.010 has been widely used in the experiment's analyses and calibrations.

In measuring the true kinetic energy E of the particle in the RS, it is necessary to "unsaturate" the measured energy L . The saturation effect is mostly important as a charged particle is coming to rest and hence is heavily ionizing. For $\pi\mu\mu$ triggers, the low-momentum particles come to a stop soon after they enter the RS making the saturation effects very noticeable.

The saturation effect was studied extensively for all three heavy particles, p , π and μ . The goal was to verify that a correct measurement of the masses in a known sample of each particle can be made. This was done by calculating the mass from P and K , determining the peak position of the gaussian distribution, and comparing it to the expected value.

With a Birks' constant of 0.01, it was found to be necessary to add 2.5 MeV to the saturated energy of each track in order to obtain the correct peak position for all three masses. The consistency among the three samples by using this method was grounds for adopting addition of 2.5 MeV as an empirical correction to the true

Particle	Expected mass (MeV)	Peak Position (MeV)	sigma (MeV)
π^+	139.6	141.9	21.0
μ^+	105.7	105.0	12.0
p^+	938.3	949.7	137.5

Table 4.6: Expected and measured masses for the π^+ , μ^+ , and p^+ samples.

kinetic energy of each track.

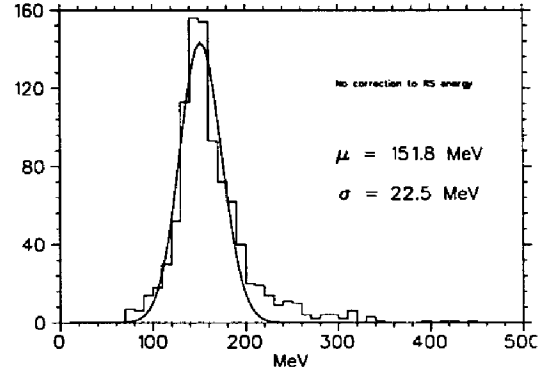
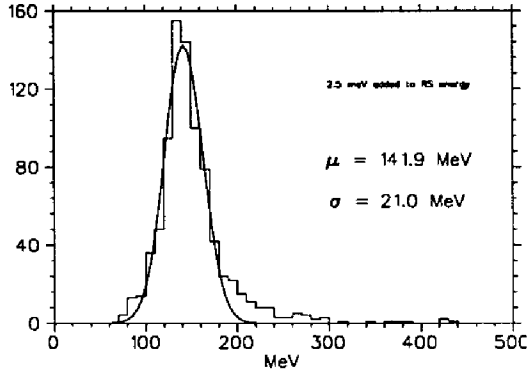
Spectra

Figure 4.10 shows the results of the mass measurements before and after the 2.5 MeV correction. Unsaturation based on the corresponding particle-id hypothesis was included in all measurements. The results are summarized in Table 4.6.

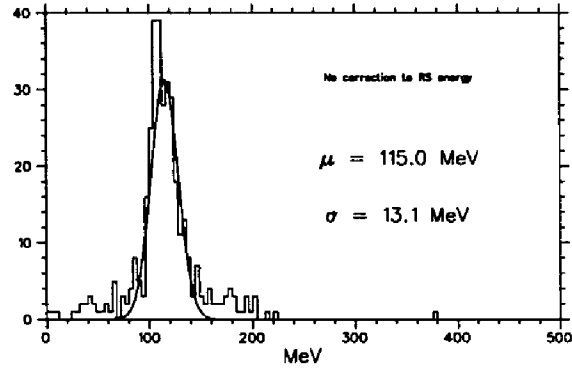
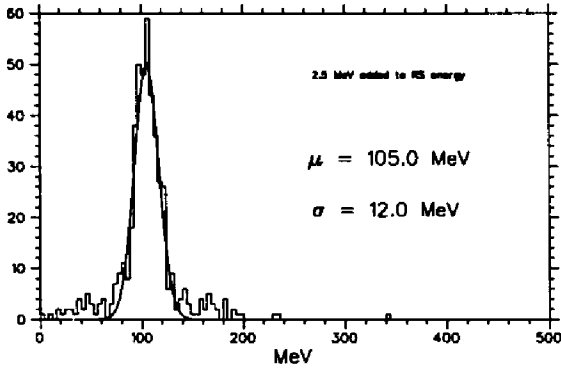
Cuts

The electron cut required the measured mass of any track (negative or positive) to be greater than $60 \text{ MeV}/c^2$. The mass was calculated twice based on both a pion and a muon hypothesis, and the same cut was applied for each value. For a muon, the mass is over-estimated with a pion hypothesis. Therefore muons with μ -hypothesis masses slightly above $60 \text{ MeV}/c^2$ are not eliminated by either cut. On the high tail of the mass distributions, another cut was placed on positive tracks at $190 \text{ MeV}/c^2$, again, based on both hypotheses. The negative tracks were required to be below $135 \text{ MeV}/c^2$ to be consistent with a μ^- . These cuts confined the positive and negative tracks roughly within $[m_\mu - 3\sigma_\mu, m_\pi + 3\sigma_\pi]$ and $[m_\mu - 3\sigma_\mu, m_\mu + 3\sigma_\mu]$, respectively.

PIONS



MUONS



PROTONS

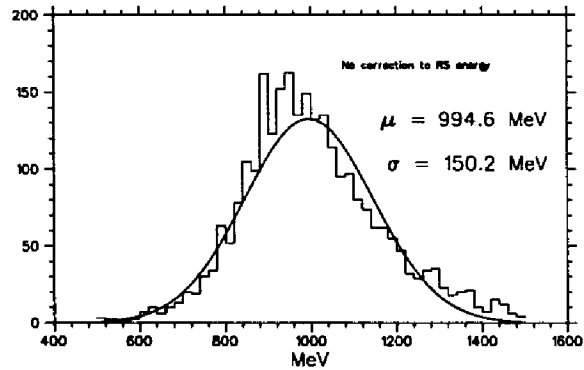
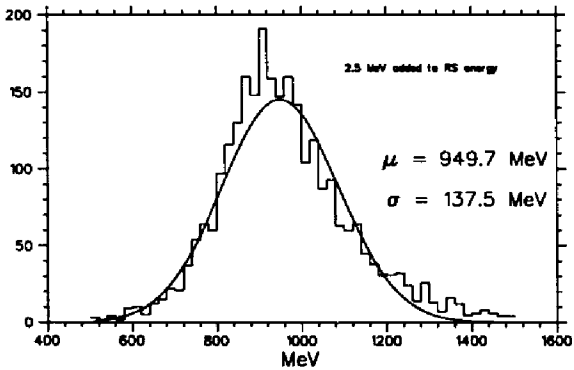


FIG. 4.10: Measured mass of for the π^+ , μ^+ , and p^+ samples with and without the 2.5 MeV correction. The gaussian fits are for the comparison purpose.

Decay	++ Branch	+- Branch	
$\pi\mu\mu$	$\pi^+\mu^+$	$\pi^+\mu^-$	$\mu^+\mu^-$
K_{e4}	π^+e^+	$\pi^+\pi^-$	$e^+\pi^-$
τ	$\pi^+\pi^+$	$\pi^+\pi^-$	$\pi^+\pi^-$

Table 4.7: Combinations of particles in the ++ and +- branches for the three major decays in Pass3.

No reasonable measurement of the mass can be made if two DC tracks end up in the same RS cluster. This scenario almost always occurs with a pair of positive and negative tracks. Events of this type were rejected before calculating the mass.

4.4.2 Combination of Charges

The mass cuts reduced the total sample by a factor of ~ 2 . In particular, the number of Dalitz decays were greatly lowered since at least one of the e^+e^- pair was subject to a mass measurement. In addition, the positive-track mass cut has a large rejection for the K_{e4} events in which the e^+ reached the RS. The negative-track mass cut, on the other hand, does not have a high rejection for π^- . That is because a π^- deposits a considerable amount of energy in its stopping counter and thus looks like a lighter particle when its kinetic energy is compared to its momentum (see the detailed discussion for the π^- in 4.2.3). This allows many K_{e4} events in which the $\pi^+\pi^-$ pair reached the RS to escape the mass cut.

Table 4.7 contains the possible combinations of charged particles for the main decay modes present at this point. It shows that for either of the K_{e4} or τ backgrounds in the +- branch there is always a π^- for which a solid mass measurement is not

Branch	Rejection of the K_{e4}	Efficiency	(for $\pi\mu\mu$)
++	~ 22 (from mass cut on e^+)	31% requiring ++	93.9% from mass cuts
+-	1.7 (from mass cut on e^+ and π^-)	69% requiring +-	91.5% from mass cuts

Table 4.8: $\pi\mu\mu$ acceptance and K_{e4} rejection in the ++ and +- branches.

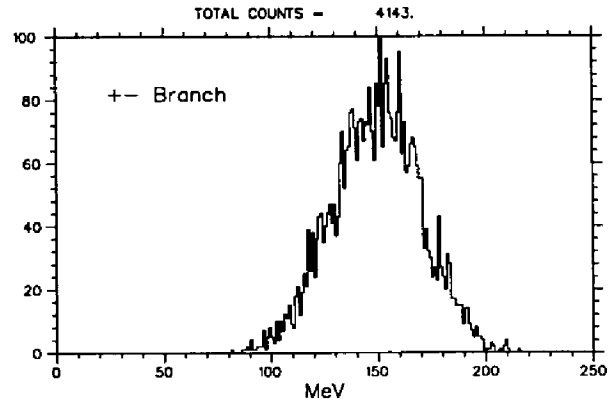
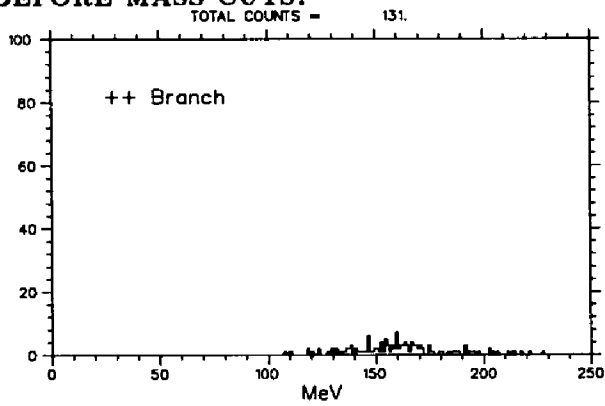
possible. However, in the ++ branch, the mass cuts can vastly eliminate the K_{e4} by rejecting the e^+ . Therefore, it was required in Pass3 that both of the RS-DC-TG tracks be positive. This condition imposes a large efficiency loss for $\pi\mu\mu$; according to UMC, only 1/3 of $\pi\mu\mu$ events will satisfy this requirement. However the enormous suppression of K_{e4} as a major source of background is certainly worth the 69% loss of acceptance. The effects of this cut are summarized in Table 4.8. Clearly, this requirement has no major effect on the τ background since the ++ branch of τ was immune to the applied mass cuts.

Figures 4.11 and 4.12 illustrate the number of $\pi\mu\mu$ and K_{e4} UMC events in each branch both before and after the applied mass cuts. As the total numbers of counts indicate, the K_{e4} background in the Pass2 output will be suppressed by three orders of magnitude after the mass cuts and the ++ requirement.

4.4.3 Conservation of Momentum

There are fewer quantities one can measure for the third track if it does not leave the Target. There is certainly no momentum measurement available, and the kinetic energy is uncertain because of the short range of the particle. This causes a greater

BEFORE MASS CUTS:



AFTER MASS CUTS:

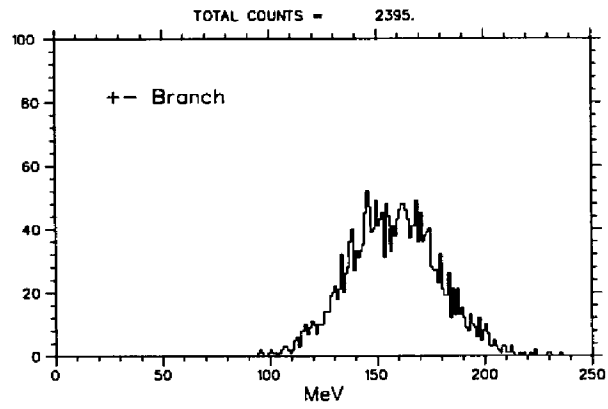
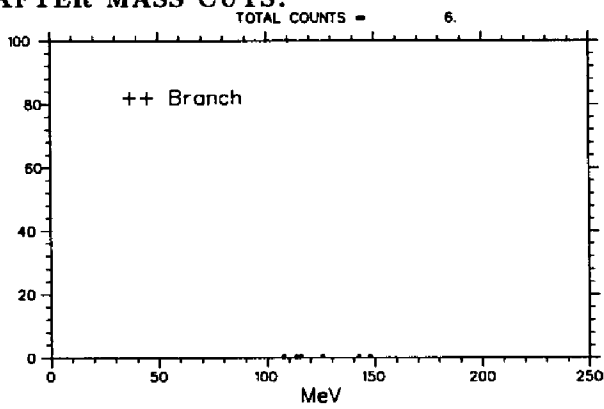


FIG. 4.11: Total kinetic energy distribution of UMC-generated K_{e4} before and after mass cuts.

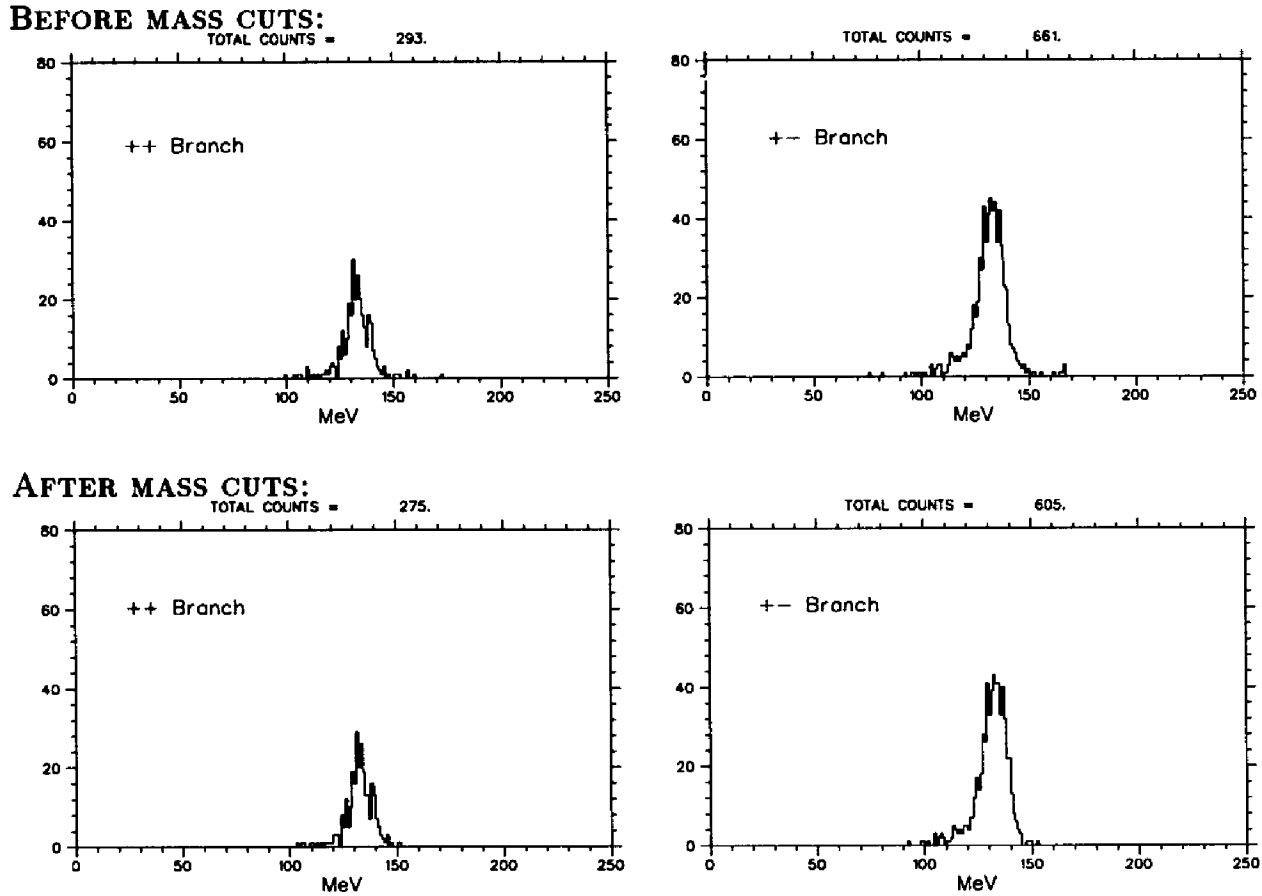


FIG. 4.12: Total kinetic energy distribution of UMC-generated $\pi\mu\mu$ before and after mass cuts.

portion of the energy to overlap the kaon blob and hence increases the error. Nevertheless, one can measure the kinetic energy and also the transverse initial direction of the third track by taking advantage of the fine segmentation of the Target. Using these quantities, one can then make a consistency check with the expected values of such quantities from the two analyzed tracks, a stopped kaon, and the energy-momentum conservation law. This is equivalent to a kaon invariant mass reconstruction.

Based on conservation of momentum for a kaon decay at rest and the momentum measurement for the two energetic tracks, one can derive the *expected* direction and momentum of the third decay product. For the $\pi\mu\mu$ events in the $++$ branch, this particle is a μ^- . Therefore, it is also possible to calculate the expected kinetic energy of this track using m_μ . Cuts can then be placed on the differences between the expected and measured values of direction and kinetic energy. These cuts can both eliminate the events in which some momentum was carried away by a neutrino (in case of K_{e4}) and those in which a π^- deposited too much energy in the Target (in cases of both K_{e4} and τ).

Missing Momentum for Three DC-track Events

The most direct application of a momentum conservation is in the rare cases where three DC tracks were present. In such situations, one can calculate the vector sum $\vec{p}^{(all)}$ of the three momenta and compare it with $\vec{0}$. Any significant difference can then be attributed to a neutrino. Because the softest track is more likely to have penetrated only as far as the first couple of layers in the DC, its longitudinal component of

momentum $\vec{P}_z^{(3)}$ is not well-measured. This introduces large uncertainties in $\vec{P}^{(all)}$ and can cause efficiency loss. The transverse momentum of all three tracks on the other hand is better measured. Thus it is more reliable to compare $\vec{P}_t^{(all)}$ with $\vec{0}_t$.

Let $f(p_t)$ be the distribution of the events in the transverse momentum space.

Then

$$dN = f(p_t) \cdot d^2 p_t$$

where dN is the number of events in a $d^2 p_t$ slice of this space. Thus,

$$dN = f(p_t) \cdot 2\pi p_t dp_t$$

$$\begin{aligned} \Rightarrow f(p_t) &= \frac{1}{2\pi} \frac{dN}{p_t dp_t} \\ &= \frac{1}{\pi} \frac{dN}{d(p_t^2)}. \end{aligned}$$

Therefore it is more sensible to study the distribution of events in the transverse momentum space by plotting p_t^2 . Figure 4.13 shows the histogram of $(P_t^{(missing)})^2$

where

$$\begin{aligned} P_t^{(missing)} &= \left| \vec{0}_t - (\vec{P}_t^{(1)} + \vec{P}_t^{(2)} + \vec{P}_t^{(3)}) \right| \\ &= \left| \vec{P}_t^{(1)} + \vec{P}_t^{(2)} + \vec{P}_t^{(3)} \right|. \end{aligned}$$

A cut was applied at 3600 corresponding to $P_t^{(missing)} = 60 \text{ MeV}/c$

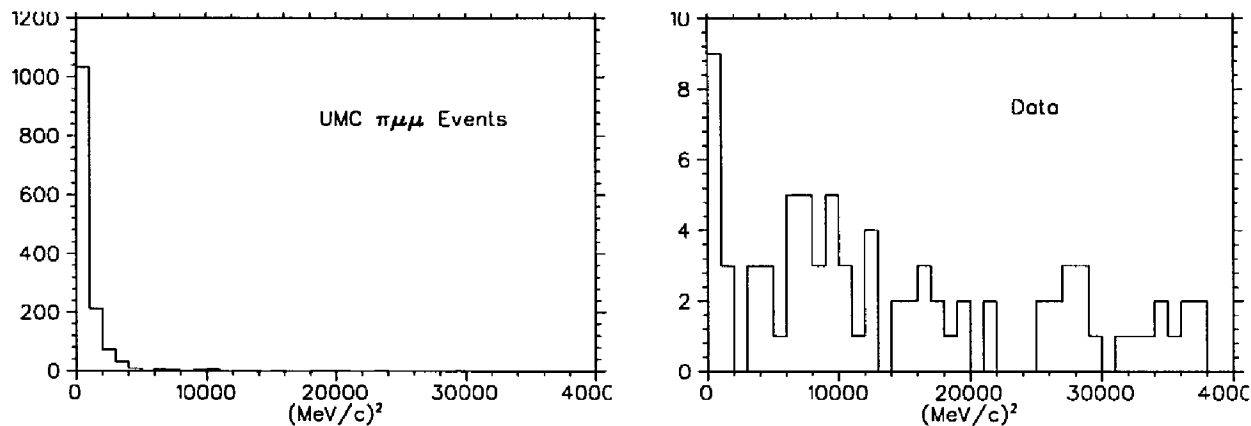


FIG. 4.13: Difference between measured and expected transverse momentum squared for the UMC-generated $\pi\mu\mu$ events and the data.

Expected Transverse Direction of Target Stub

Although it is not possible to measure the momentum of the third track when it remains in the Target (leaving a *stub*), one can use a measurement of its transverse direction and compare it to the expected value from conservation of momentum. For a K_{e4} event at this point, the expected direction defines the superposition of $\vec{P}_t^{(e^+)}$ and $\vec{P}_t^{(\nu_e)}$. Since only the e^+ can leave a trace, a significant difference between $\vec{P}_t^{(e^+)}$ and $\vec{P}_t^{(expected)}$ is observed for a large $\vec{P}_t^{(\nu_e)}$ (see Figure 4.14). A cut on this difference can eliminate many surviving K_{e4} events.

The transverse direction $\bar{\theta}$ was determined from the average of the azimuthal angles θ_i of the cells in the TG-stub weighted by the distance between the cell and the vertex, d_i .

$$\bar{\theta} = \frac{\sum_i \theta_i \cdot d_i}{\sum_i d_i}.$$

UMC studies confirm that this weighting scheme reduces the difference between the expected and measured directions in a $\pi\mu\mu$ sample.

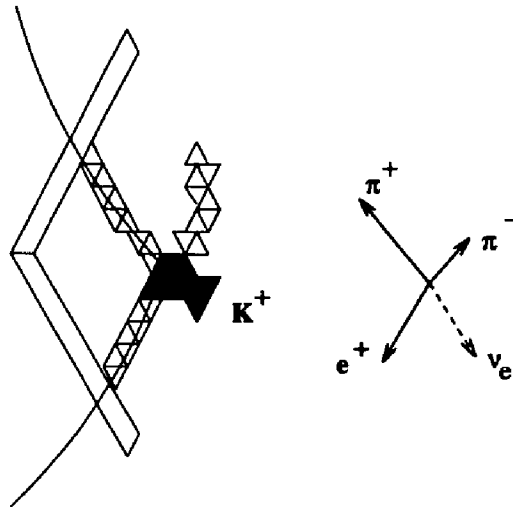


FIG. 4.14: Schematic K_{e4} event with an observable missing transverse momentum due to a large $\vec{P}_t^{\nu_e}$.

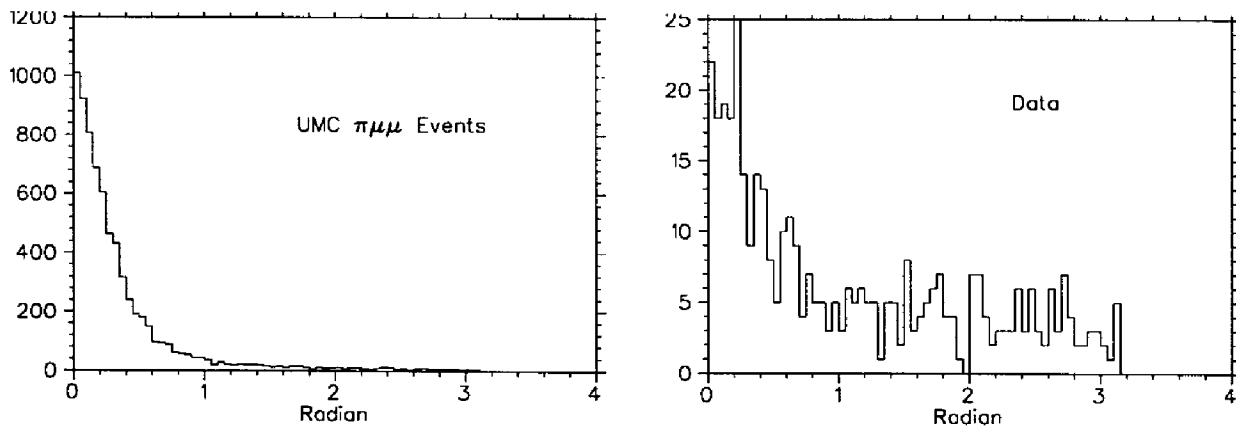


FIG. 4.15: Difference between measured and expected angle of the TG stub for the UMC-generated $\pi\mu\mu$ events and the data. Events above 0.9 radian were cut.

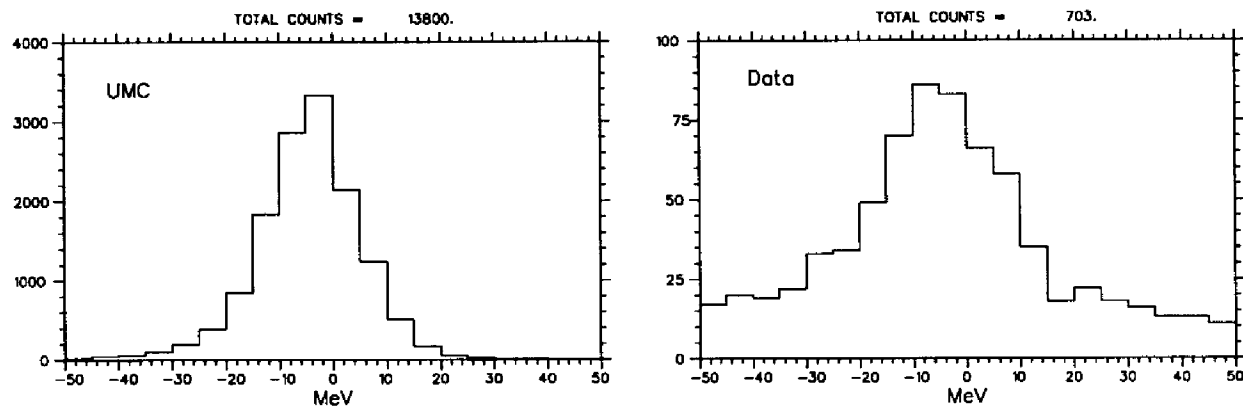


FIG. 4.16: Difference between measured and expected kinetic energy of the TG stub for the UMC-generated $\pi\mu\mu$ events and the data.

Figure 4.15 shows the distribution of the difference between the measured and expected values of θ in the two-track events. Events with more than 0.9 radian discrepancy in either direction were cut.

Kinetic Energy of the Target Stub

In a $\pi\mu\mu$ event with two DC-TG tracks, $\vec{P}_t^{(expected)}$ represents $\vec{P}_t^{(\mu^-)}$. Therefore, one can calculate the expected kinetic energy of the μ^- . This value can be compared with the measured energy in the Target stub and any I-counter associated with it. The difference between the observed and expected energies provides an effective tool against the π^- that deposit substantial energy after their nuclear absorption. Figure 4.16 shows the corresponding difference for the data and UMC events. The cut accepts values within $[-30,20]$ MeV.

Pass3 CUTS	Estimated Rejection
Mass of any RS-DC track $> 60 \text{ MeV}/c^2$	2.16
Mass of the negative RS-DC track $< 135 \text{ MeV}/c^2$	1.24
Mass of the positive RS-DC track $< 190 \text{ MeV}/c^2$	1.14
++ combination of charges	4.18
Kinetic energy of the TG stub $\in [-30, 20] \text{ MeV}^\dagger$	1.15
P_{missing} in events with 3 DC-TG matched tracks $< 60 \text{ MeV}/c$	1.02
Angle of the TG stub within 0.9 radian of the expected direction †	1.10

Table 4.9: Summary of Pass3 cuts with their rejections estimated from part of the 1989 data. \dagger Events with two DC-TG matched tracks.

4.4.4 Pass3 Summary

Table 4.9 includes a summary of the Pass3 cuts along with their estimated rejections.

The total energy spectra of the final events in each year are shown in figure 4.17.

Each plot shows a large $\pi\mu\mu$ signal as a peak around 140 MeV with small levels of background. The signal will be discussed in detail in 4.6. The total number of $\pi\mu\mu$ events must be calculated by performing a fit and a background subtraction.

Therefore the sources and approximate level of this background has to be understood before the signal can be extracted.

4.5 Background

The main sources of background in the final sample are the other kaon decay modes which result in more than one charged particle in the final state. In the following

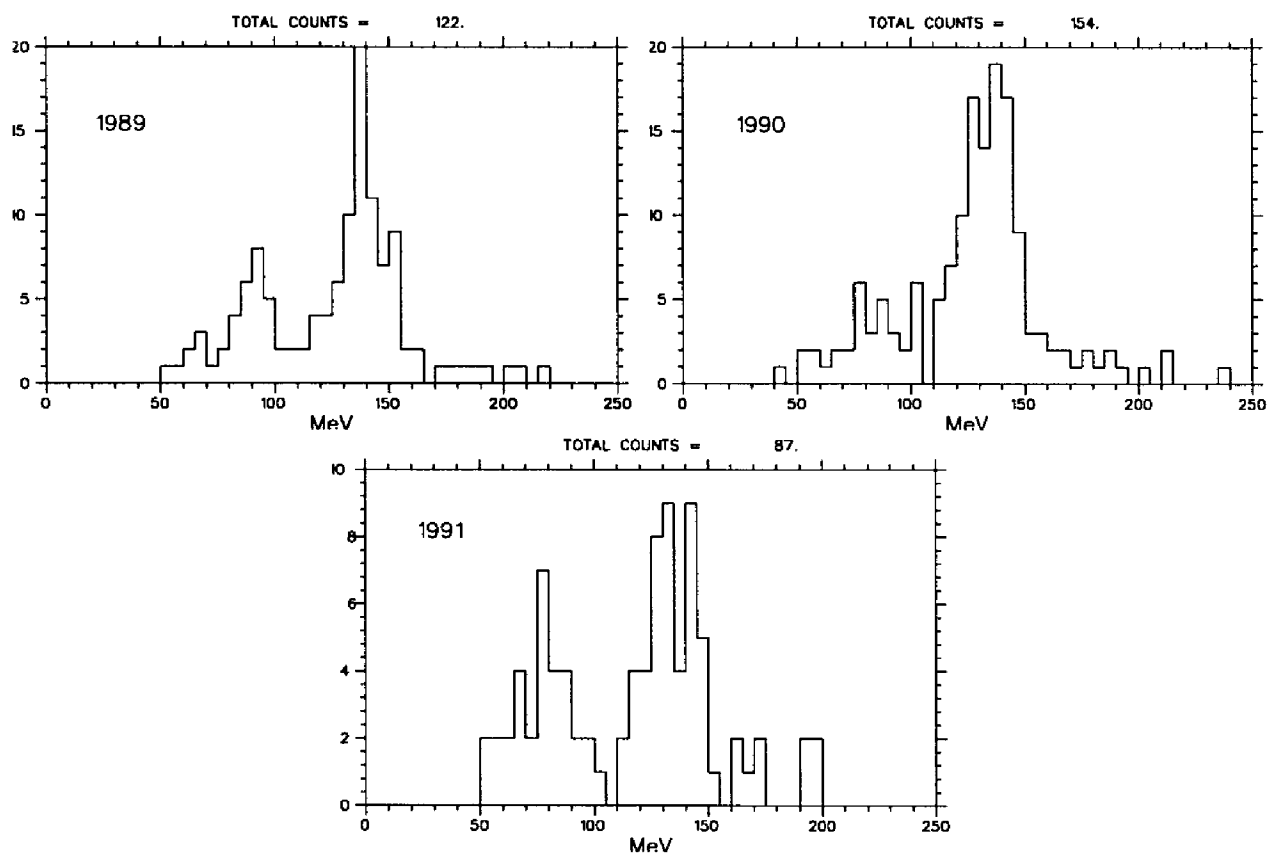


FIG. 4.17: Total kinetic energy distribution for the Pass3 output events.

Mode	B.R.	Pass Level 1	Absolute Level	%
$K^+ \rightarrow \mu^+ \nu_\mu$	6.351×10^{-1}	0	0	0
$K^+ \rightarrow \pi^+ \pi^0$	2.117×10^{-1}	$(1.92 \pm 0.16) \times 10^{-4}$	$(4.06 \pm 0.33) \times 10^{-5}$	71.6
$K^+ \rightarrow \pi^+ \pi^+ \pi^-$	5.59×10^{-2}	$(3.59 \pm 0.62) \times 10^{-5}$	$(3.80 \pm 0.27) \times 10^{-6}$	6.70
$K^+ \rightarrow \pi^0 e^+ \nu_e$	4.82×10^{-2}	$(2.78 \pm 1.13) \times 10^{-5}$	$(1.34 \pm 0.55) \times 10^{-6}$	2.36
$K^+ \rightarrow \pi^0 \mu^+ \nu_\mu$	3.18×10^{-2}	$(3.04 \pm 0.28) \times 10^{-4}$	$(9.65 \pm 0.89) \times 10^{-6}$	17.0
$K^+ \rightarrow \pi^+ \pi^0 \pi^0$	1.73×10^{-2}	$(9.88 \pm 7.00) \times 10^{-6}$	$(1.71 \pm 1.21) \times 10^{-7}$	0.30
$K^+ \rightarrow \mu^+ \nu_\mu \gamma$	5.46×10^{-3}	$(1.26 \pm 0.15) \times 10^{-4}$	$(6.87 \pm 0.84) \times 10^{-7}$	1.21
$K^+ \rightarrow \pi^0 e^+ \nu_e \gamma$	2.72×10^{-4}	$(1.97 \pm 1.14) \times 10^{-5}$	$(5.37 \pm 3.10) \times 10^{-9}$	0.009
$K^+ \rightarrow \pi^+ \pi^0 \gamma$	2.75×10^{-4}	$(1.41 \pm 0.34) \times 10^{-4}$	$(3.89 \pm 0.94) \times 10^{-8}$	0.07
$K^+ \rightarrow \pi^+ \pi^+ \pi^- \gamma$	1.0×10^{-4}	$(9.11 \pm 4.55) \times 10^{-6}$	$(9.11 \pm 4.55) \times 10^{-10}$	0.002
$K^+ \rightarrow \pi^+ \pi^- e^+ \nu_e$	3.91×10^{-5}	$(9.28 \pm 0.14) \times 10^{-3}$	$(3.63 \pm 0.10) \times 10^{-7}$	0.64
$K^+ \rightarrow \pi^+ \pi^- \mu^+ \nu_\mu$	1.4×10^{-5}	$(1.88 \pm 0.15) \times 10^{-4}$	$(3.24 \pm 0.26) \times 10^{-9}$	0.006
$K^+ \rightarrow \pi^+ \mu^+ \mu^-$	$< 2.3 \times 10^{-7}$	(0.109 ± 0.001)	$< 2.5 \times 10^{-8}$	< 0.04
Total		Rate	5.7×10^{-5}	

Table 4.10: $\pi\mu\mu$ trigger acceptance for various K^+ decay modes using the full (1989) trigger. The last column shows the expected percentage of each decay mode present in the $\pi\mu\mu$ triggers.

discussion, it is demonstrated that the size of the background level due to the major sources is small enough to allow a background subtraction to be explained in Section 4.6.3.

UMC was used to study the contributing modes after the level 1 trigger. The ten highest-rate decay channels of K^+ were simulated and their acceptance in $\pi\mu\mu$ trigger was measured. The K_{e4} and $K_{\mu4}$ decay modes were also included. The results are shown in Table 4.10.

4.5.1 K_{e4}

As explained in Section 4.4.2, the level of K_{e4} decays is greatly reduced after the mass cuts and the $++$ requirement. Trigger acceptance for K_{e4} UMC events was measured to be $(9.28 \pm 0.14) \times 10^{-3}$ in 1989 and $(7.13 \pm 0.16) \times 10^{-3}$ in 1990/1991. In obtaining these values, the crude π^- simulation described in Section 4.2.3 was included in UMC. The acceptance also includes a 2 nsec cut on the K^+ decay time in order to simulate the online delayed coincidence (see Section 4.2.2). From 25584 UMC-generated K_{e4} decays which passed the $\pi\mu\mu$ trigger, all but one event were rejected by the Pass3 requirements (see Table 4.11). With 8.2×10^{10} and 22.1×10^{10} stopped kaons in 1989 and 1990/1991 respectively (see Table 5.1), one obtains the following estimate for the K_{e4} level in the final sample:

$$\begin{aligned}
 \text{Number of } K_{e4} &= (\text{Stopped Kaons}) \cdot (\text{Trigger Acceptance}) \cdot (\text{Branching Ratio}) \cdot \\
 &\quad (\text{Pass3 Acceptance}) \cdot \epsilon_{\text{recon}} \\
 &\simeq \left((8.2 \times 10^{10})(9.28 \times 10^{-3}) + (22.1 \times 10^{10})(7.13 \times 10^{-3}) \right) \cdot \\
 &\quad (3.9 \times 10^{-5}) \left(\frac{1}{25584} \right) (0.65) \\
 &= 2.3
 \end{aligned}$$

where $\epsilon_{\text{recon}} \simeq 0.65$ includes factors such as the accidental loss, offline delayed coincidence, and DC reconstruction efficiency.

Cut	# events surviving		Rejection	
Events entering	25584		-	
Pass2	4281		6.0	
Mass cuts	2401		1.8	
++ branch	6		400	
++ branch		131		33
Mass cuts		6		22
Momentum conservation cuts	1		~6	

Table 4.11: Rejection of various stages of the analysis for UMC- K_{e4} events. The effects of applying the mass- and branching-cuts in two different orders are shown separately.

4.5.2 $K_{\mu 4}$

Trigger acceptance for $K_{\mu 4}$ UMC events was measured to be $(1.88 \pm 0.15) \times 10^{-4}$ in 1989 and $(1.11 \pm 0.12) \times 10^{-4}$ in 1990/1991. Running Pass3 on the UMC-generated events the expected acceptance for $K_{\mu 4}$ was 0.014 ± 0.005 . Hence

$$\begin{aligned}
 \text{Number of } K_{\mu 4} &= (\text{Stopped Kaons}) \cdot (\text{Trigger Acceptance}) \cdot (\text{Branching Ratio}) \cdot \\
 &\quad (\text{Pass3 Acceptance}) \cdot \epsilon_{\text{recon}} \\
 &\simeq \left((8.2 \times 10^{10})(1.88 \times 10^{-4}) + (22.1 \times 10^{10})(1.11 \times 10^{-4}) \right) \cdot \\
 &\quad (1.4 \times 10^{-5})(0.014)(0.65) \\
 &= 5.0
 \end{aligned}$$

Thus, about 5 events are expected to appear in the final sample. The maximum Q-value for this decay is 108.86 MeV. However because of the kinetic energy carried away

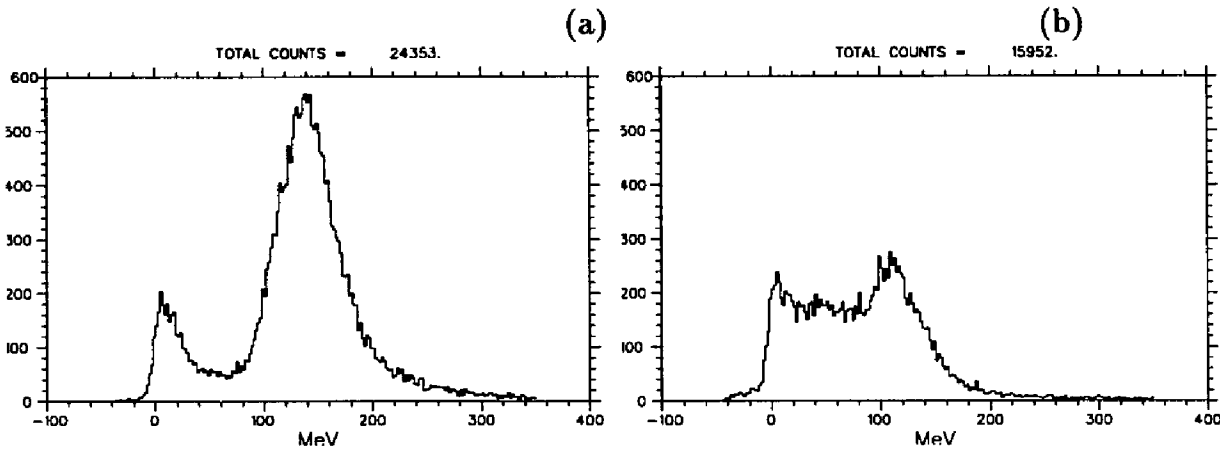


FIG. 4.18: Mass of the positive and negative tracks in the Pass2 output. Pion and muon hypotheses are used for the positive and negative particles, respectively.

by the neutrino the bulk surviving $K_{\mu 4}$ events are expected to appear underneath the τ peak although the presence of the π^- in the Target can extend the total energy. This tail is similar to what is expected for the τ events.

4.5.3 Dalitz/ γ Conversions

As indicated in Table 4.10, most of the $\pi\mu\mu$ triggers ($\sim 92\% = 4.8$ million) are due to π^0 Dalitz decays or photon conversions. These decay channels (to be abbreviated as Dalitz modes) are greatly eliminated by the photon-veto and RS-energy cuts in Pass2 as described in Section 4.3. Figure 4.18 shows the calculated mass of the positive and negative tracks in the Pass2 output. From Figure 4.18a, the number of e^+ with a measured mass below 60 MeV can be estimated at about 3000. The electron peak is not centered at zero because *i*) the pion hypothesis—including the 4.12 MeV subtraction—was used in the calculation and *ii*) the higher energy electrons have already been eliminated by means of the $RS_{\text{inner}} < 120$ MeV cut (Table 4.4). The number of e^- is much harder to estimate because of the π^- tracks with nuclear

absorption excess energies which reduce the calculated mass. However, the height of the electron peak being equal to that of the positrons suggests a similar number of e^- tracks in the Pass2 output. Even though a fraction of the e^+ is due to the K_{e4} decays, the majority of the positive and all of the negative electrons are due to π^0 origins. In any case, only the number of e^+ is relevant to the background level in the final ++ sample.

The expected number of $K_{e4} e^+$ in plot 4.18a can be estimated as following: from Table 4.11 the number of K_{e4} after Pass2 is expected to be:

$$\begin{aligned} \text{Number of } K_{e4} \text{ after Pass2} &\simeq \left((8.2 \times 10^{10})(9.3 \times 10^{-3}) + (22.1 \times 10^{10})(7.1 \times 10^{-3}) \right) \cdot \\ &\quad (3.91 \times 10^{-5}) \left(\frac{1}{6.0} \right) (\epsilon_{\text{recon}}) \\ &= 6331 \end{aligned}$$

According to Figure 4.19a, 420 out of 4201 of the positive tracks are “light” e^+ , *i.e.*, electrons with calculated masses < 60 MeV. Thus one expects about $6331 \times \left(\frac{420}{4201} \right) = 633$ “light” e^+ tracks from K_{e4} in plot 4.18a. In other words, about 2400 “light” e^+ are from the other modes, namely $K_{\pi 2}$, $K_{\mu 3}$, $K_{e 3}$, or other photon conversion sources.

This number is an overestimate of this background for two reasons:

1. Some of the $m < 60$ MeV tracks are due to muons from $K_{\mu 3}$ or pion decays (see Figure 5.4).

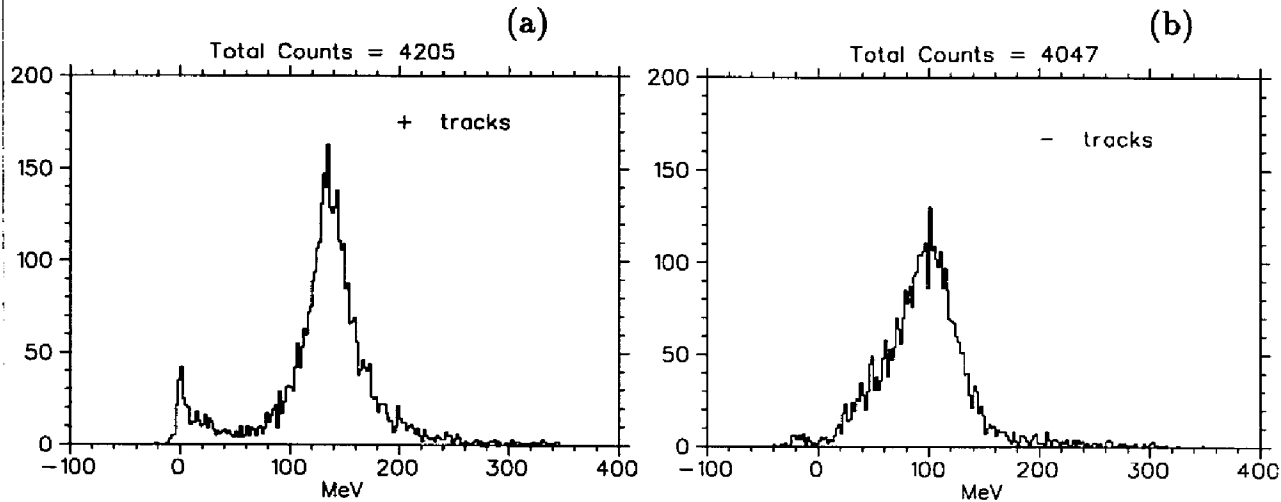


FIG. 4.19: Mass distribution of the positive and negative tracks in the UMC- K_{e4} Pass2 output. Pion and muon hypotheses are used for the positive and negative particles, respectively.

2. K_{e3} events (with two e^+ in the $++$ branch) are counted twice.

The Dalitz electrons after the strict timing and momentum cuts of Pass2 are very similar to K_{e4} e^+ in terms of their low range in the RS. According to the K_{e4} results in Table 4.11, the rejection of mass cut at this point is 22 for the $++$ branch. In other words, 22 represents the ratio of “light” to “heavy” electrons. A sample of UMC- $K_{\pi 2}$ Dalitz decays was generated. These were speeded up by forcing all π^0 to undergo a Dalitz decay, requiring a T·A after the π^+ stopped, and vetoing the event as soon as the energy sum in BV or EC exceeded the trigger thresholds. A hand scan of 47 UMC-Dalitz decays indicated that about 20% of them have 3 RS-reaching tracks, clearly two of them being electrons. The remaining 80% are two track events. Since all the particles in the Dalitz modes are relatively energetic, no suppression of the $++$ branch due to dE/dx losses in the Target should be expected. Therefore, the fraction of events in the $++$ branch is about 1/3 of the two track events, similar to

what is seen in the UMC- $\pi\mu\mu$ events. Hence,

$$\text{Number of Dalitz events after Mass cuts} < 2400 \cdot \left(\frac{0.2}{22^2} + \frac{0.8}{3 \times 22} \right) \simeq 30.$$

In order to estimate the kinematic rejection, Pass3 was run on the UMC sample with the timing and momentum cuts relaxed. This allowed 12 events to pass the mass- and branching-cuts. From these, only half survived the kinematic requirements. Thus,

$$\text{Final number of Dalitz events} < 15.$$

In all of the surviving UMC events, $E_{tot} > 200$ MeV.

4.5.4 τ

Tau decays constitute the largest source of background in the final sample. In fact, the main factor distinguishing the τ from $\pi\mu\mu$ is the former's small Q-value. The low-momentum of the pions in a τ decay is the foremost reason for its suppression by several orders of magnitude. This is mostly achieved through the 2 T·A and $N_{TG} > 20$ requirements at the trigger level as well as the ++ branching in the analysis (see Figure 4.8).

Because the Q of τ decays is only 74.94 MeV, their visible energy is safely lower than the $\pi\mu\mu$ peak. However, two effects can extend the total energy in a τ event:

1. An early decay-in-flight of one of the pions can allow the track to reach the RS more easily. To calculate the maximum additional kinetic energy K_μ in the lab

frame assume that the μ^+ is ejected right along the trajectory of the π^+ . In that case the kinetic energy of the muon is

$$\begin{aligned} K_\mu &= E_\mu - m_\mu \\ &= \gamma_\pi(E'_\mu + \beta_\pi p'_\mu) - m_\mu \end{aligned}$$

Assuming that each π^+ carries a kinetic energy of $K_\pi \simeq Q_\tau/2 = 37.5$ MeV,

$$\beta_\pi = 0.62 \quad , \quad \gamma_\pi = 1.27.$$

In the rest frame $p'_\mu = 29.8$ MeV/c and $E'_\mu = 109.7$ MeV,

$$\Rightarrow K_\mu = 57.2 \text{ MeV.}$$

Therefore, an early decay of a τ pion can increase the event's total energy to $K_\pi + K_\mu \simeq 37.5 + 57.2 = 94.7$ MeV. Even if both pions decay in flight along their corresponding trajectories, the total kinetic energy will be about $2 \times 57.2 = 114.4$ MeV.

2. The π^- in the Target can leave additional energy due to its nuclear absorption. This can also extend the total energy in the event. This case is discussed in detail in Section 4.6.

The large suppression of the τ by the trigger makes it formidable to generate enough UMC events without imposing early restrictions in the code. The following conditions allowed creating a relatively large sample of $++\tau$ events:

- Requiring the two π^+ to each have more than 35 MeV in kinetic energy.
- Requiring the π^+ transverse momenta to be almost along the azimuthal direction so that they can leave the Target before losing too much energy.
- Forcing the kaon to stop outside a circle of radius 3 cm in the Target.
- Propagating the second π^+ only if the first one or its decay products give a T·A.
- Carrying on the time-consuming π^- simulation only if 2 T·A is satisfied.

The above requirements on the kinematic quantities of the pions selects only 1.8×10^{-4} of the area in the Dalitz plot. In addition, the Target constraint takes only 0.52 of all the kaons in a nominal K^+ beam distribution. Among the accepted initial events, 5.5×10^{-3} pass the full 1989 $\pi\mu\mu$ trigger. In other words, the acceptance of the $\pi\mu\mu$ trigger for the τ , with the above conditions, is

$$\epsilon_{\tau} = (1.8 \times 10^{-4}) \cdot (0.52) \cdot (5.5 \times 10^{-3}) = 5.1 \times 10^{-7}.$$

This value is based on the assumption that none of the events discarded by the above restrictions would have passed the trigger. The 1990/1991 trigger acceptance is lower by $\sim 30\%$.

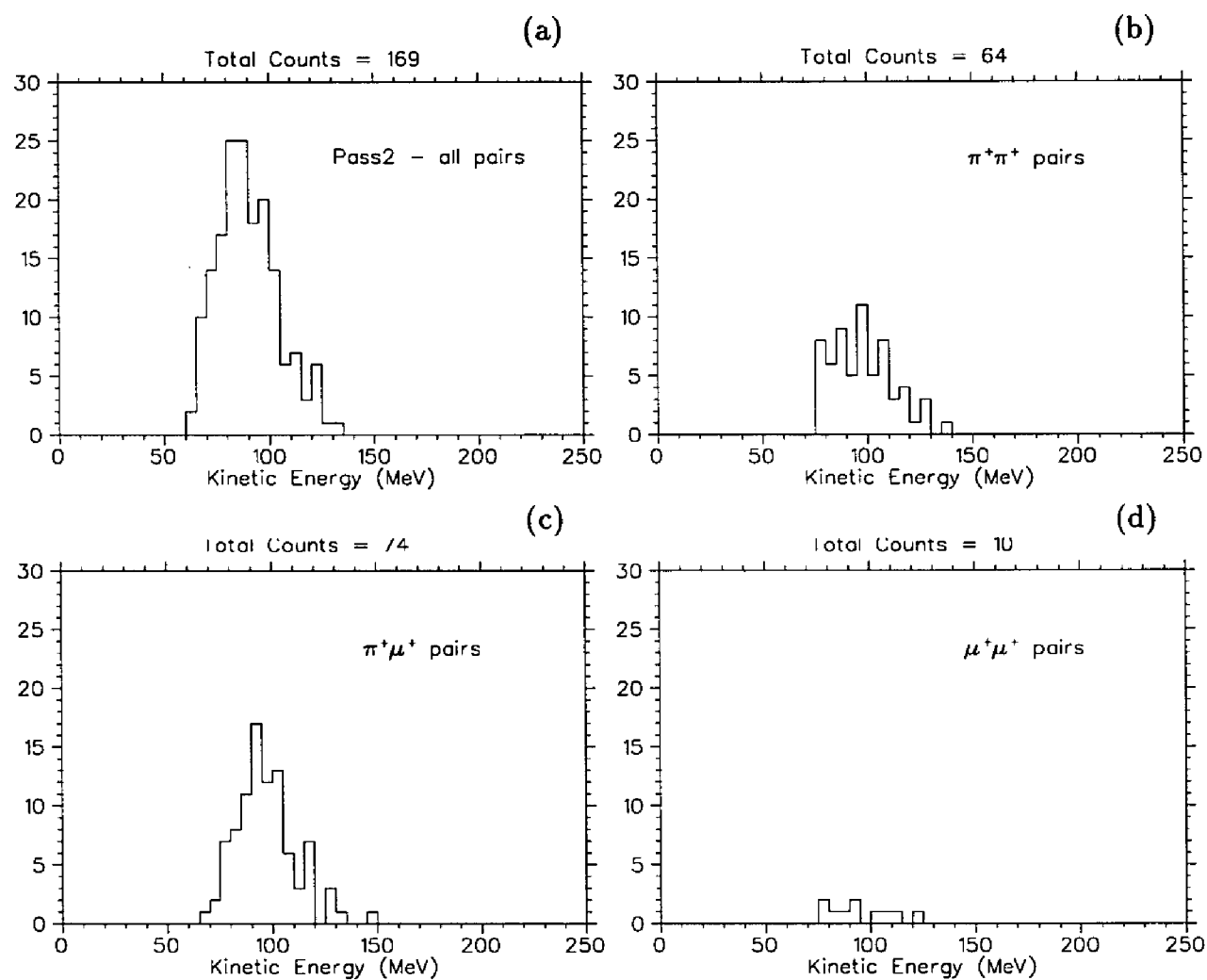


FIG. 4.20: Total kinetic energy distribution of the UMC-generated τ events after Pass2 for (a) all, (b) $\pi\pi$, (c) $\pi\mu$, and (d) $\mu\mu$ pairs.

A sample of 775 τ events passing the $\pi\mu\mu$ trigger was generated in this manner. Figure 4.20(a) shows the energy distribution of the surviving events after Pass2. Figures 4.20(b), (c), and (d) indicate the τ events that consist of $\pi\pi$, $\pi\mu$, or $\mu\mu$ pairs, respectively. Note that the implemented π^- model has a limited capability in simulating the local energy deposition after the absorption. However, UMC can reliably indicate the extension of the total energy spectrum due to the π^+ decays-in-flight. As 4.20(c) reveals, this early decay is an essential mechanism for allowing a vast number of τ to survive. Nevertheless, the additional released kinetic energy extends their spectrum into the $\pi\mu\mu$ signal region only slightly.

44 events in this sample survived the Pass3 cuts. Therefore, the expected level of this background in the final sample is:

$$\begin{aligned}
 \text{Number of } \tau &= (\text{Stopped Kaons}) \cdot (\text{Trigger Acceptance}) \cdot (\text{Branching Ratio}) \cdot \\
 &\quad (\text{Pass3 Acceptance}) \cdot \epsilon_{\text{recon}} \\
 &\simeq \left((8.2 \times 10^{10})(5.1 \times 10^{-7}) + (22.1 \times 10^{10})(3.6 \times 10^{-7}) \right) \cdot \\
 &\quad (0.0559) \left(\frac{44}{775} \right) (0.65) \\
 &= 250 \pm 36.
 \end{aligned}$$

This is the expected number of τ in the absence of a π^- full simulation. The total energies of the final UMC- τ events are between 50 and 110 MeV. In the data, the final number of events within that range is only 104. This indicates that additional rejection of the τ —not simulated by UMC—has occurred. With real data, further

Year	Number of events in Pass3 output
1989	123
1990	154
1991	87
Total	364

Table 4.12: Number of output events in Pass3.

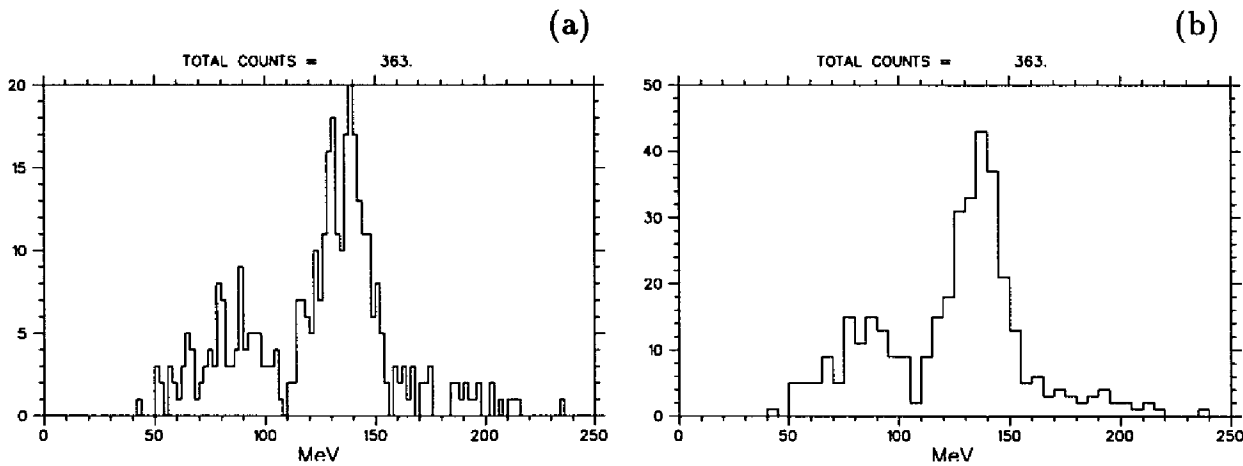


FIG. 4.21: Total kinetic energy distribution for the Pass3 output events for all three years plotted in (a) 2-MeV and (b) 5-MeV bins.

reduction from the E_{stub} cut is expected due to local energy deposition of the π^- .

4.6 Signal

Table 4.12 shows the number of events surviving after Pass3. The total energy E_{tot} spectra of the output events in each year are plotted in Figure 4.17. Figure 4.21 shows the three-year total energy spectrum plotted in 2-MeV and 5-MeV bins. E_{tot} is the sum of the track energies in the Range Stack, I-counter and the Target. They include the following corrections:

1. The track corresponding to the higher calculated mass is assumed to be due to a pion. UMC studies show that this assumption is correct in 78.9% of the times (see Section 4.6.2). Thus, the energy calculated based on a pion hypothesis will be used for the track. This energy includes the following corrections:

(a) adding the 2.5 MeV empirical correction described in Section 4.4.1.

(b) subtracting 3.0 MeV as saturated $\pi \rightarrow \mu$ energy release,

(c) unsaturating the energy with a pion hypothesis,

(d) correcting for the energy loss in the DC cylindrical walls.

For the track corresponding to the lower measured mass the energy calculated based on a muon-hypothesis is added. The procedure is as described in the above with the exception of the $\pi \rightarrow \mu$ correction.

2. The measured Target energies in the two RS-DC-TG tracks are subject to an empirical correction. These corrections, which simply serve as a re-calibration measure, have been determined by studying the energy-range correlations for a sample of τ decays. The method is based on using the path length in the Target, as determined by the DC-track extrapolation back into the TG, in order to calibrate the observed energy in the Target tracks [19]. The correction factors for each year are tabulated in Table 4.13.

3. Since the particles that reach the RS are nearly minimum ionizing in the Target (momenta > 70 MeV/c), no unsaturation corrections are necessary to their measured TG energies. However, unsaturation effects become significant for

Year	TG energy correction factor
1989	1.218 ± 0.002
1990	1.366 ± 0.002
1991	1.048 ± 0.002

Table 4.13: Correction factor for the measured energy in the Target tracks.

the heavily ionizing third track. If the Target stub is not associated with a DC track, then it is assumed that it has come to a stop within the TG or IC. In that case, the stub's energy is corrected and then unsaturated (along with any associated I-counter) based on a μ^- hypothesis.

The spectrum of E_{tot} after Pass3 indicates a large peak at about 137 MeV corresponding to the Q-value of the $\pi\mu\mu$ decay. The position of the peak is about 6 MeV below the actual Q-value of 142.76 MeV. The missing energy is mostly hidden within the kaon blob in the Target. As the kaon decays, the products travel some distance within the Target cells that were already lit by the stopping kaon. The ADC values of these cells represent the sum of the two energies, and it is not possible to separate them. This effect lowers the total measurable decay energy. One can crudely estimate the amount of this "missing" energy as following: a stopping kaon typically illuminates about 4 Target triangles. The corresponding area is $4 \times 0.21 \text{ cm}^2 \simeq 0.84 \text{ cm}^2$. For a rough estimate of the decay products' pathlength within the kaon blob, its shape can be approximated as a circle of radius 0.5 cm (to obtain the same area). Then with decay vertex at the center, the total path length traversed by the three charged particles is 1.5 cm. Assuming a $3 \text{ MeV/cm } \frac{dE}{dx}$, an average of 4.5 MeV of

the tracks' energies is expected to be lost within the kaon blob. This value is clearly higher for tracks with non-zero longitudinal components. A more accurate determination of the expected $\pi\mu\mu$ E_{tot} peak position is obtained from the UMC-generated events (see Figure 4.28, for example).

A smaller peak corresponding to the τ decays stands at about 80 MeV. The peak appears at an energy higher than the 74.94 MeV Q-value of τ for two reasons:

1. Even though both pions have deposited 4.12 MeV in the RS as they decayed into muons, this amount has been subtracted only from one of the tracks because of the $\pi^+\mu^+$ assumption.
2. The π^- is likely to locally deposit extra energy after its nuclear absorption in the Target.

The latter fact is responsible for the extension of the τ events even as far as $Q_\tau + m_{\pi^-}$ in the total energy spectrum. As Figure 4.4 indicates, the tail of the excess energy is a vanishing exponential. Nevertheless some τ events can manage to appear in the $\pi\mu\mu$ signal region (between 110 and 160 MeV). These events can survive the $E_{expected}$ cut (described in 4.4.3) in two ways:

1. The expected momentum, and hence kinetic energy, of the stub can be overestimated due to the inaccuracy in the P_z of the other two tracks. This allows events with too much energy in the stub to leak in. In such cases, the extra energy appears in the E_{stub} as well as E_{tot} . Figure 4.22 shows scatter-plots of these quantities for the Pass3 and the UMC events. The data events with

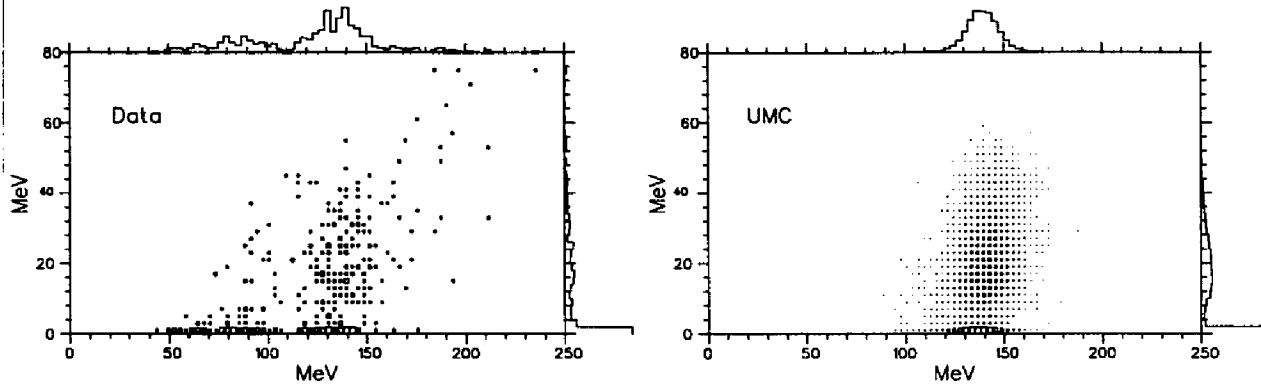


FIG. 4.22: E_{stub} versus E_{tot} for the data and UMC- $\pi\mu\mu$ Pass3 output events.

$E_{\text{stub}} > 50$ MeV are in this category.

2. The splash of energy from the π^- overlaps the target tracks for the other two tracks. In this case, the extra energy does not appear in E_{stub} while E_{tot} is still contaminated. These events appear in the lower right portion of the data plot in Figure 4.22. In this case, the dE/dx of the first two tracks will have higher values. Figure 4.23 shows the corresponding distribution for the data and the Monte Carlo. The high tail in the data (particularly above 6 MeV/cm) is caused by the π^- splashes over the swaths.

Even though the origin of the background underneath the signal in the final spectrum is believed to be mostly due to the interacting π^- , it was decided not to apply further energy cuts in the Target to reduce them. The reason is that the additional requirements would be of the form of energy cuts on individual Target tracks. This can always raise the legitimate issue of bias in the analysis: applying cuts on various components of energy in an event, one cannot justify a peak in the *total energy* spectrum as the signal.

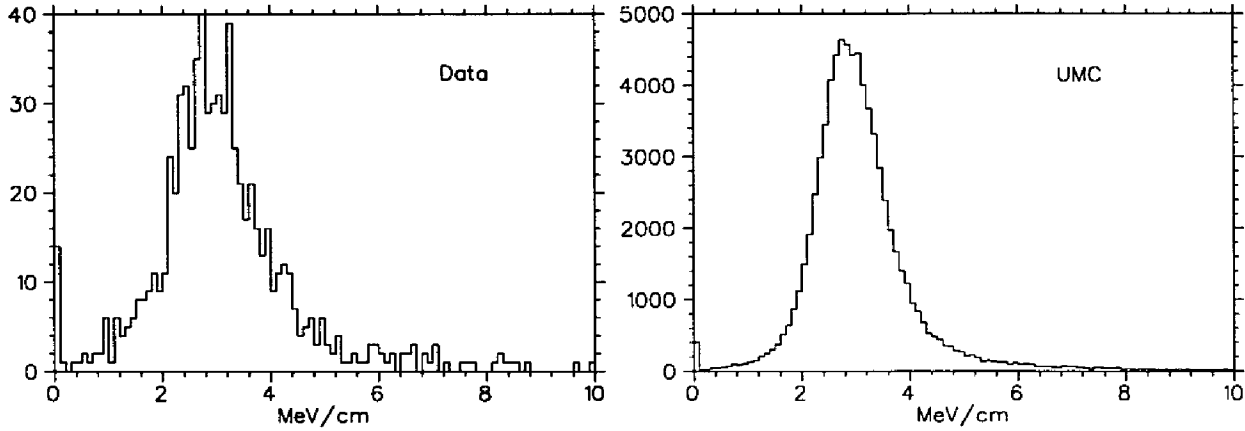


FIG. 4.23: dE/dx in the two energetic Target tracks for the data and the UMC- $\pi\mu\mu$ Pass3 output events.

Nevertheless, additional cuts on dE/dx and E_{stubb} can provide a cleaner sample of $\pi\mu\mu$ events in the signal region for further studies. Though not included in Pass3, the following cuts can be used to “purify” the events in the $\pi\mu\mu$ region:

- $\frac{dE}{dx} < 4.8$ MeV/cm for the first two tracks.
- $E_{\text{stubb}} < 48$ MeV.

Figure 4.24 shows the spectrum of the final events after the above cuts (compare to Figure 4.21).

From the total number of stopped kaons and the overall acceptance for each year (see chapter 6), one can calculate the expected ratio of final $\pi\mu\mu$ events for the three data sets:

$$\text{Expected ratio of } \pi\mu\mu \text{ events} = 1 : 1.20 : 0.60$$

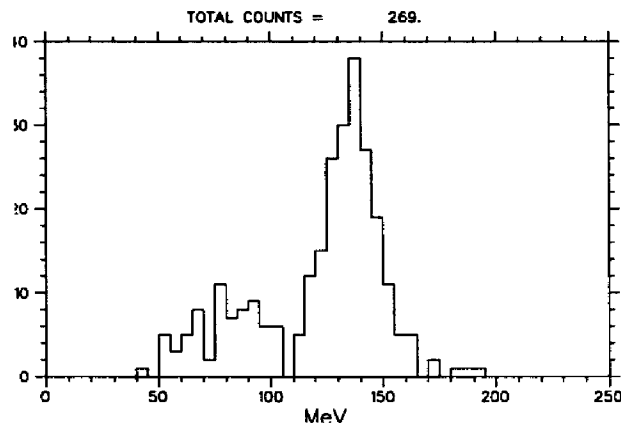


FIG. 4.24: Total kinetic energy distribution for the Pass3 output events after the “purification” cuts on Target energies.

The actual numbers of events within the [110,160] MeV range in the Pass3 outputs are

$$\begin{aligned} \text{Number of events in the signal region} &= 75 : 104 : 47 \\ &= 1 : 1.39 : 0.63. \end{aligned}$$

The number of events in the signal region, which includes some background, is only a rough representation of the true number of $\pi\mu\mu$ decays. The actual number of signal events for all three years will be determined from a fit as described in 4.6.3.

4.6.1 Stability of the Signal

As demonstrated in Figures 4.21 and 4.24, the π^- energy cuts in the Target have little effect on the $\pi\mu\mu$ peak. This indicates that the signal is indeed stable with respects to the cuts that, according to UMC, should not significantly affect the $\pi\mu\mu$ particles. The level 1 trigger hardware problem in the 1991 data had the benefit of

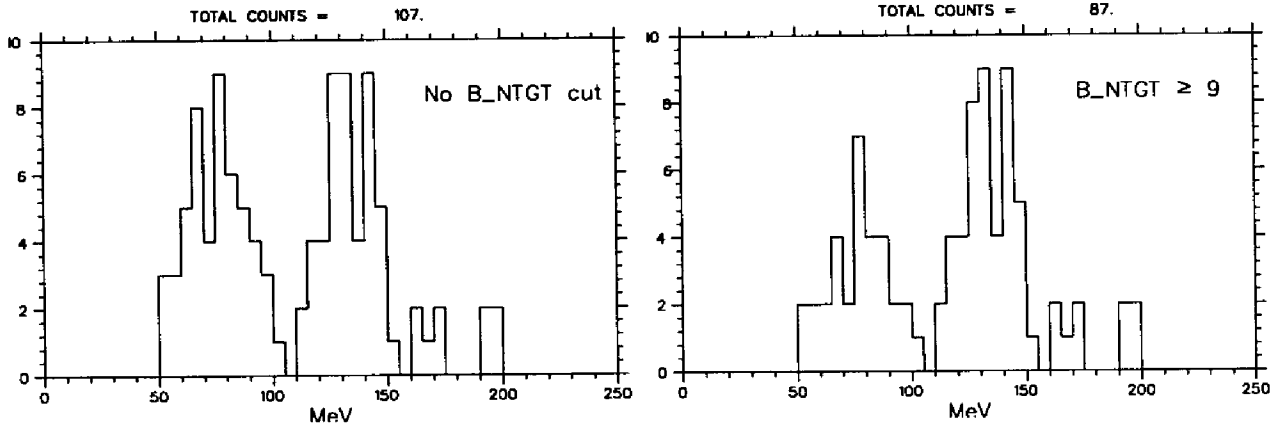


FIG. 4.25: Total kinetic energy distribution of the 1991 events with and without the $B_NTGT \geq 9$ cut. The requirement is expected to have little effect on true $\pi\mu\mu$ events.

providing another measure for studying the stability of the signal. As explained in Section 4.3.4, a change in the $N_{TG} > 20$ cut should have little effect on the acceptance for $\pi\mu\mu$ events according to UMC whereas the τ can noticeably leak in as a result of a lower threshold. Figure 4.25 shows the spectrum of the final events for the 1991 data with and without the $B_NTGT \geq 9$ condition which was designed to compensate for the slipping threshold. As the plots indicate, the number of events in the $\pi\mu\mu$ signal region was hardly affected by the cut.

4.6.2 FITPI Study of the Final Sample

As a check on the identity of the RS-DC-TG tracks in the final events, they were subject to a $\pi^+ \rightarrow \mu^+$ pulse fit in the stopping counters using the Transient Digitizers (see Section 3.4.1). The code performing the fit is called FITPI. Three conditions were examined: i) both tracks passed FITPI, ii) the “heavier” particle (as determined from the calculated mass) passed, and iii) the “lighter” particle passed. The E_{tot} spectrum of the final events that satisfy each condition are plotted in Figure 4.26.

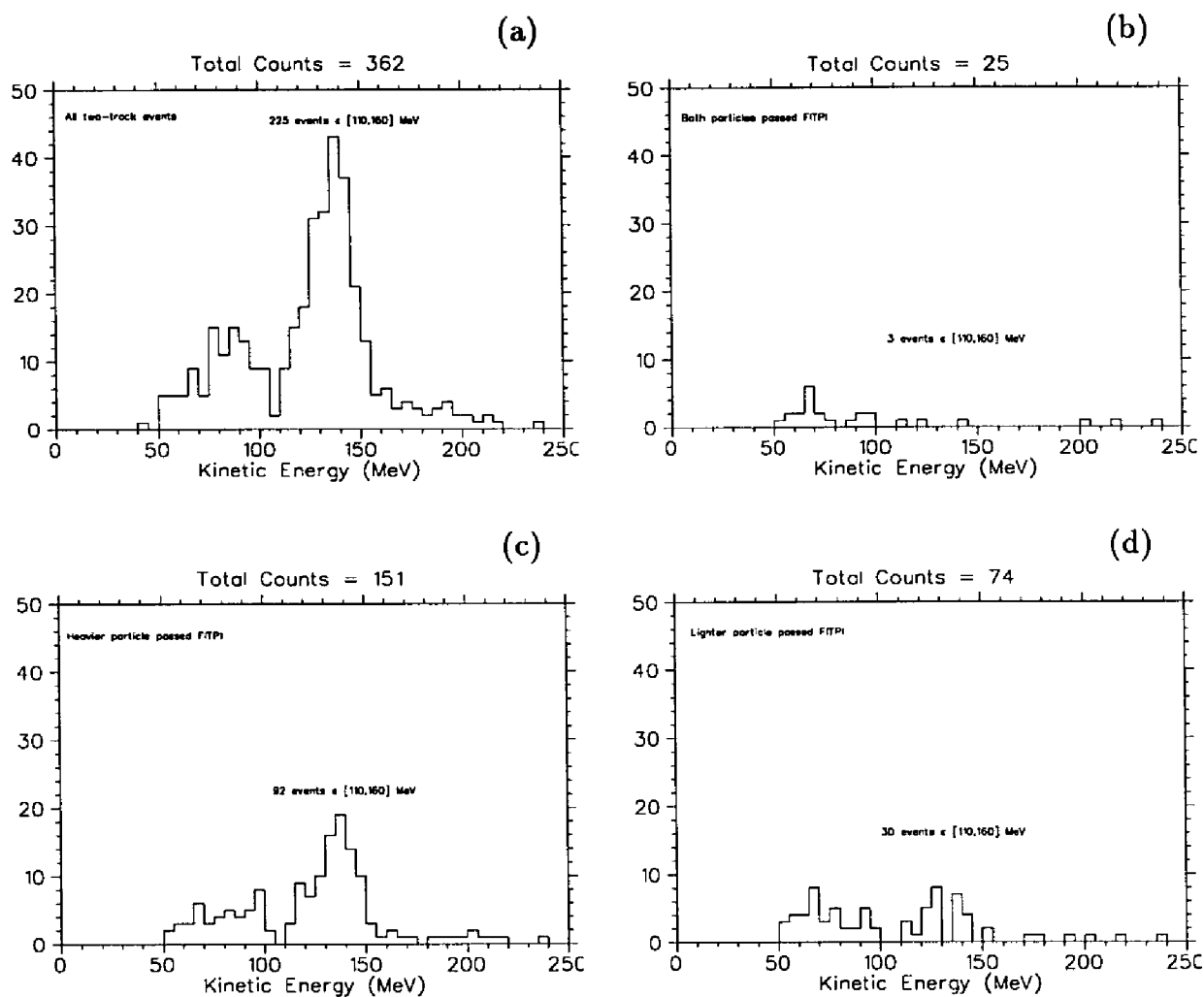


FIG. 4.26: Energy spectrum for a) all two-track events, and also events in which b) both particles, c) the heavier one, and d) the lighter one passed FITPI.

A quantitative study can be made using the numbers on these plots. This is based on the assumption that all the events consist of a $\pi^+\pi^+$ pair (from tau decays), a $\pi^+\mu^+$ pair (from $\pi\mu\mu$, τ , or $K_{\mu 4}$ decays), or $\mu^+\mu^+$ pair (from early $\pi \rightarrow \mu$). Through fitting, the most likely number of each pair was calculated.

A few values need to be specified first: the efficiency ϵ_π of FITPI for correct identification of a pion stopping in layers A or B is roughly one-half. However, the estimated number of each pair is a sensitive function of ϵ_π . The exact value of this number for pions stopping in the inner RS layers cannot be easily obtained from the τ or K_{e4} samples since the identity of the stopped particle cannot be independently verified.⁵ Decays in flight of the pion for example cannot be singled out and discounted. Therefore, it was decided to allow ϵ_π to also be determined from the fit. This was made possible by the availability of four independent measurements in Figure 4.26.

The rejection R_μ of FITPI for muons is about 50. This number was estimated from $K_{\mu 2}$ muons stopping in the deeper RS layers. In applying FITPI to the heavier or the lighter particle, the goal is to use the measured value of mass to distinguish between pions and muons. However, due to the finite resolutions of the mass measurements, there is a certain probability for mis-identification. This probability is measured with UMC-generated $\pi\mu\mu$ events after reproducing the observed mass resolutions using proper RS energy smearing. By checking the true identity of each particle using the UMC banks, the fraction of correct identifications f was measured to be 78.9%.

⁵For deeper layers of the range stack, the monoenergetic pions from $K_{\tau 2}$ decay are used.

Here is a summary of the above definitions:

$$R_\mu \simeq 50$$

$$f = 0.789$$

The four equations describing the number of events in the plots are:

$$\left\{ \begin{array}{l} N_{\text{all}}(\epsilon_\pi, N_{\pi\pi}, N_{\pi\mu}, N_{\mu\mu}) = N_{\pi\pi} + N_{\pi\mu} + N_{\mu\mu} \\ N_{\text{both}}(\epsilon_\pi, N_{\pi\pi}, N_{\pi\mu}, N_{\mu\mu}) = \epsilon_\pi^2 N_{\pi\pi} + \frac{\epsilon_\pi}{R_\mu} N_{\pi\mu} + \frac{1}{R_\mu^2} N_{\mu\mu} \\ N_{\text{heavier}}(\epsilon_\pi, N_{\pi\pi}, N_{\pi\mu}, N_{\mu\mu}) = \epsilon_\pi N_{\pi\pi} + (f\epsilon_\pi + \frac{1-f}{R_\mu}) N_{\pi\mu} + \frac{1}{R_\mu} N_{\mu\mu} \\ N_{\text{lighter}}(\epsilon_\pi, N_{\pi\pi}, N_{\pi\mu}, N_{\mu\mu}) = \epsilon_\pi N_{\pi\pi} + ((1-f)\epsilon_\pi + \frac{f}{R_\mu}) N_{\pi\mu} + \frac{1}{R_\mu} N_{\mu\mu} \end{array} \right.$$

A fitting was performed as a way to “solve” the above non-linear four equations and four unknowns. The function to be minimized in the fit was defined as

$$\chi^2 = \frac{(N_{\text{all}} - N_{\text{all}})^2}{N_{\text{all}}} + \frac{(N_{\text{both}} - N_{\text{both}})^2}{N_{\text{both}}} + \frac{(N_{\text{heavier}} - N_{\text{heavier}})^2}{N_{\text{heavier}}} + \frac{(N_{\text{lighter}} - N_{\text{lighter}})^2}{N_{\text{lighter}}}$$

where N_{all} , N_{both} , N_{heavier} , and N_{lighter} are the observed number of events in each plot or in certain regions of them.

For the total number of events:

$$\left\{ \begin{array}{l} N_{\text{all}} = 362 \\ N_{\text{both}} = 25 \\ N_{\text{heavier}} = 151 \\ N_{\text{lighter}} = 74 \end{array} \right.$$

The fitted values are

$$\left\{ \begin{array}{l} \epsilon_{\pi} = 0.55 \pm 0.18 \\ N_{\pi\pi} = 72.4 \pm 41.9 \\ N_{\pi\mu} = 249.4 \pm 66.0 \\ N_{\mu\mu} = 40.2 \pm 89.6 \end{array} \right. \quad \chi^2 = 9.4 \times 10^{-8}$$

yielding

$$\left\{ \begin{array}{l} N_{\text{all}} = 362.0 \\ N_{\text{both}} = 25.0 \\ N_{\text{heavier}} = 151.0 \\ N_{\text{lighter}} = 74.0 \end{array} \right.$$

One can use the above procedure to obtain a fit with the number of events within

the signal region ($E_{tot} \in [110, 160]$ MeV) in each plot

$$\left\{ \begin{array}{l} N_{\text{all}} = 225 \\ N_{\text{both}} = 3 \\ N_{\text{heavier}} = 92 \\ N_{\text{lighter}} = 30 \end{array} \right.$$

The fitted values for the $\pi\mu\mu$ signal region are

$$\left\{ \begin{array}{l} \epsilon_{\pi} = 0.54 \pm 0.21 \\ N_{\pi\pi} = 2.9 \pm 7.7 \\ N_{\pi\mu} = 211.6 \pm 51.1 \\ N_{\mu\mu} = 10.7 \pm 36.3 \end{array} \right. \quad \chi^2 = 3.2 \times 10^{-2}$$

which yield

$$\left\{ \begin{array}{l} N_{\text{all}} = 225.1 \\ N_{\text{both}} = 3.1 \\ N_{\text{heavier}} = 92.6 \\ N_{\text{lighter}} = 29.1 \end{array} \right.$$

The value of $N_{\pi\mu}$ in the signal region, 211.6 ± 51.1 , approximately represents the number of $\pi\mu\mu$ decays (196.0 ± 16.7) which will be derived in the next section through a fitted background subtraction. It should be noted that the number of $\pi\mu$ pairs obtained here includes the $\pi\mu$ pairs from the τ events after a π^+ decay-in-flight. The above results provide another consistency check of the observed signal based on

a particle identification tool not used in the analysis.

4.6.3 Extracting the Signal

The number of $\pi\mu\mu$ events in the final sample is extracted by performing a background subtraction on the energy spectrum. This is done based on the observation that the final events are in three classes: 1) non-interacting τ forming a gaussian around its Q, 2) $\pi\mu\mu$ events also forming a gaussian, and 3) the remaining events mostly consisting of τ and $K_{\mu 4}$ events with an interacting π^- in the TG and also some Dalitz events. The latter class is represented in the fit by a second-degree polynomial as a general function. The low level of this background and the unclarity of its exact nature are reasons for assuming the polynomial term.

The function for a weighted fit was:

$$y(x) = a + bx + cx^2 + \frac{\alpha}{\sqrt{2\pi}\sigma_1} e^{-\frac{(x-\mu_1)^2}{2\sigma_1^2}} + \frac{\beta}{\sqrt{2\pi}\sigma_2} e^{-\frac{(x-\mu_2)^2}{2\sigma_2^2}} .$$

The fitted values are

$$a = -0.90 \quad \pm 0.50$$

$$b = 0.052 \quad \pm 0.016$$

$$c = -2.0 \times 10^{-4} \quad \pm 0.6 \times 10^{-4}$$

$$\alpha = 980.2 \quad \pm 83.3$$

$$\mu_1 = 135.8 \quad \pm 0.89 \quad \frac{\chi^2}{\text{No. degrees of Freedom}} = \frac{29.4}{50 - 9} = 0.72$$

$$\sigma_1 = 10.4 \quad \pm 0.78$$

$$\beta = 330.1 \quad \pm 60.1$$

$$\mu_2 = 84.0 \quad \pm 2.34$$

$$\sigma_2 = 11.8 \quad \pm 2.38$$

The results of the fit are shown in Figure 4.27. The number of $\pi\mu\mu$ events based on the fitted value of α is:

$$N_{\pi\mu\mu} = \frac{\alpha}{\text{bin size}(5 \text{ MeV})},$$

that is,

$$N_{\pi\mu\mu} = 196.0 \pm 16.7$$

Figure 4.28 shows the total energy spectra for the UMC-generated $\pi\mu\mu$ events and the background subtracted data where the background BG is defined as

$$BG(x) = a + bx + cx^2 + \frac{\beta}{\sqrt{2\pi}\sigma_2} e^{-\frac{(x-\mu_2)^2}{2\sigma_2^2}}.$$

To examine how sensitive the extracted number of events is with respect to the assumed shape of the background, a different function was fitted to the final spectrum.

The function was defined as

$$y(x) = a(x - b)^2 e^{-\frac{(x-b)}{c}} + \frac{\alpha}{\sqrt{2\pi}\sigma_1} e^{-\frac{(x-\mu_1)^2}{2\sigma_1^2}} + \frac{\beta}{\sqrt{2\pi}\sigma_2} e^{-\frac{(x-\mu_2)^2}{2\sigma_2^2}}$$

The fitted values are:

$$a = 2.3 \times 10^{-3} \pm 1.4 \times 10^{-3}$$

$$b = 15.9 \pm 5.7$$

$$c = 45.3 \pm 7.1$$

$$\alpha = 993.5 \pm 83.5$$

$$\mu_1 = 135.9 \pm 0.9$$

$$\sigma_1 = 10.5 \pm 0.8$$

$$\beta = 317.2 \pm 73.8$$

$$\mu_2 = 84.1 \pm 2.5$$

$$\sigma_2 = 11.5 \pm 2.9$$

$$\frac{\chi^2}{\text{No. degrees of Freedom}} = \frac{32.2}{50 - 9} = 0.79$$

Figure 4.29 shows the results of the fit along with its individual components. The first term $a(x - b)^2 e^{-\frac{x-b}{c}}$ is an approximate form to represent a decaying tail. It peaks at $b + 2c = 106.5$ MeV and has a decay constant of $c = 45.3 \pm 7.1$. The number of $\pi\mu\mu$ events based on this function is

$$N_{\pi\mu\mu} = 198.7 \pm 16.7$$

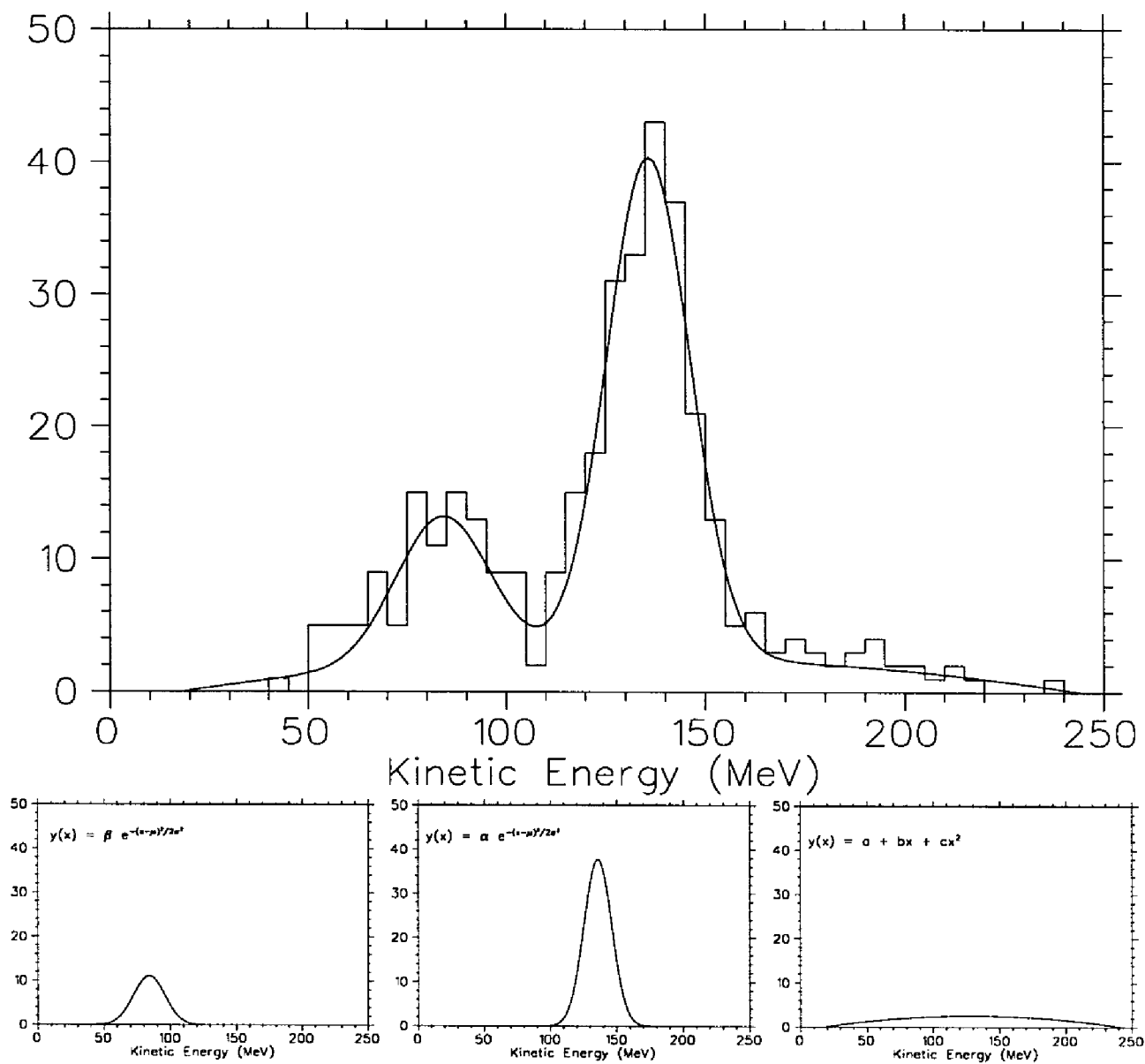


FIG. 4.27: Total kinetic energy distribution of the final events with a fit composed of two Gaussians and a second-degree polynomial.

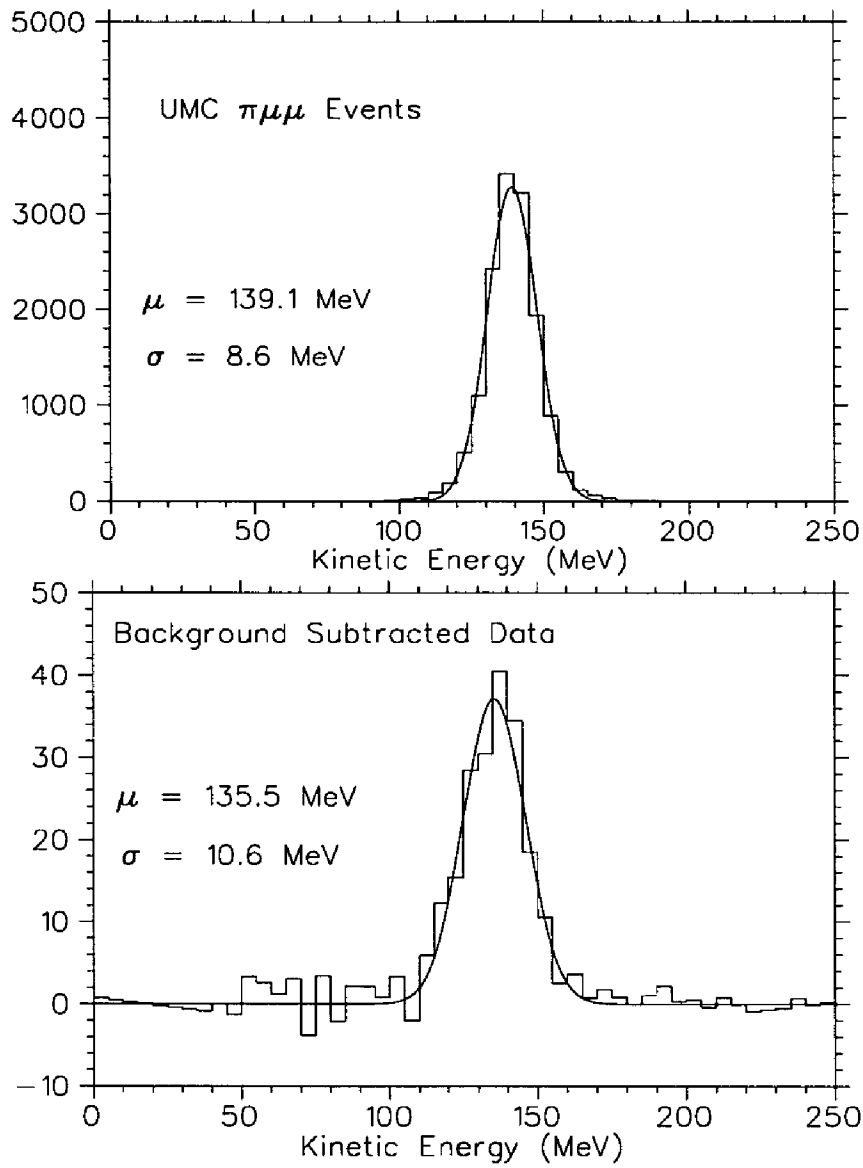


FIG. 4.28: Total kinetic energy distributions of the UMC-generated $\pi\mu\mu$ events after Pass3 and also the data events after background subtraction.

which is only 1.4% higher than the original value.

Allowing two gaussians to represent the signal and the tau peaks apparently results only in small variations in the background level as different functions for the background are tried. However, in order to obtain a safer upper limit for this level, one can assume a smearing of the tau events into the signal region starting from the top of the tau peak. The following function

$$y(x) = ae^{-\frac{x-b}{c}} + \frac{\beta}{\sqrt{2\pi}\sigma} e^{-\frac{(x-\mu)^2}{2\sigma^2}}.$$

was fitted to the final energy spectrum *only* in the 75 to 250 MeV region. As Figure 4.30 indicates, a weighted fit results in 178.5 ± 15.9 $\pi\mu\mu$ events. In other words, 17.5 events out of the central 196.0 $\pi\mu\mu$ events could be due to the background. Therefore, 17.5 (*i.e.*, 8.9%) will be used as the systematic error in the observed number of events.

As another consistency check, the initial function (two gaussians and a polynomial) was fitted to the spectrum of the “purified” sample (see Figure 4.24). According to UMC, the purification cuts have an *estimated* combined efficiency of 0.842 ± 0.003 . Therefore, the expected number of $\pi\mu\mu$ events in this sample is

$$\text{Expected } N_{\pi\mu\mu}^{\text{purified}} \simeq (196.0 \pm 16.7) \cdot (0.842 \pm 0.003) = 165.1 \pm 11.9.$$

Figure 4.31 shows the spectrum of the data along with a non-weighted fit. The results

are:

$$\begin{aligned} a &= -0.35 & \pm 0.81 \\ b &= 0.022 & \pm 0.021 \\ c &= -8.7 \times 10^{-5} & \pm 8.8 \times 10^{-5} \\ \alpha &= 887.5 & \pm 49.0 \\ \mu_1 &= 136.0 & \pm 0.43 \\ \sigma_1 &= 10.6 & \pm 0.49 \\ \beta &= 320.4 & \pm 71.4 \\ \mu_2 &= 81.8 & \pm 2.43 \\ \sigma_2 &= 17.1 & \pm 2.99 \end{aligned}$$

which yield the measured number of purified $\pi\mu\mu$ events:

$$N_{\pi\mu\mu}^{\text{purified}} = 177.5 \pm 9.8.$$

Figure 4.32 shows the decay time of the kaons in the purified $\pi\mu\mu$ sample. The measured decay time of 11.68 ± 0.97 nsec is consistent with kaon life time of 12.371 ± 0.029 nsec.

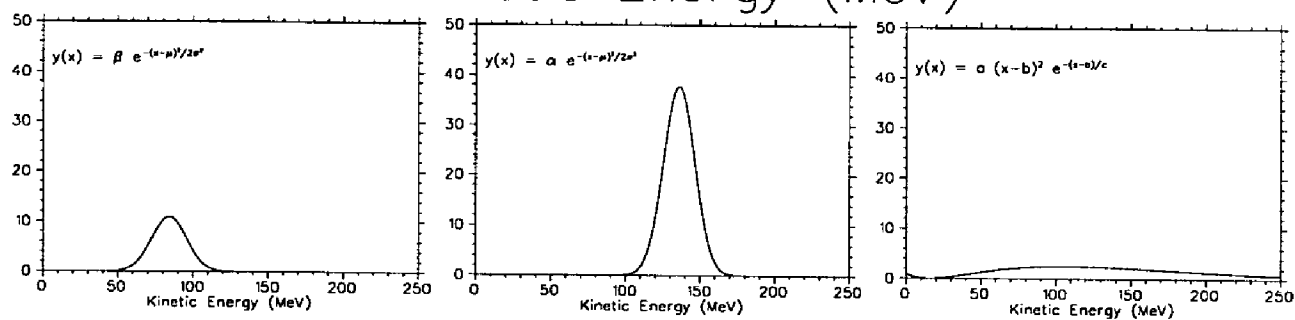
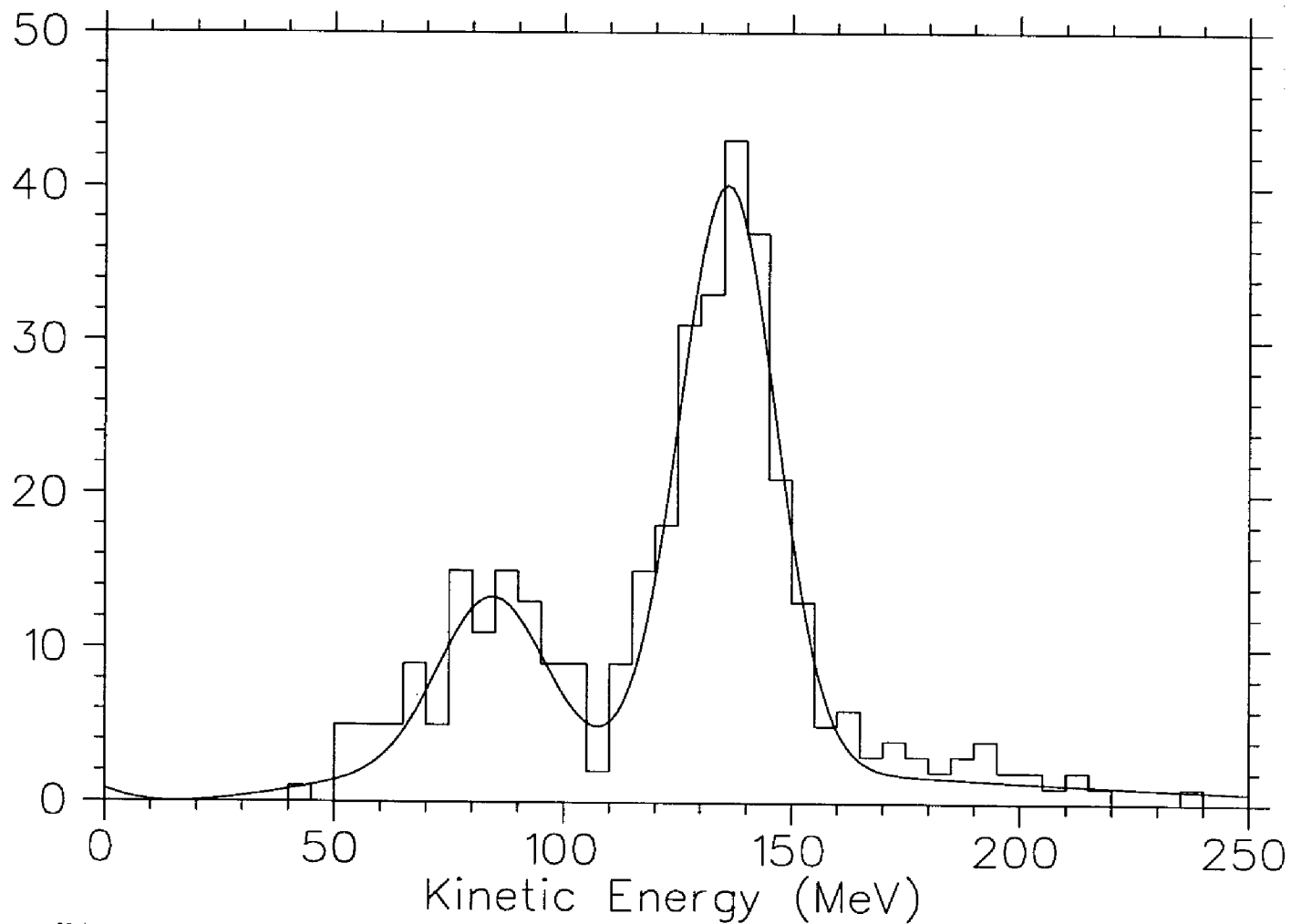


FIG. 4.29: Total kinetic energy distribution of the final events with a fit composed of two Gaussians and an exponential term.

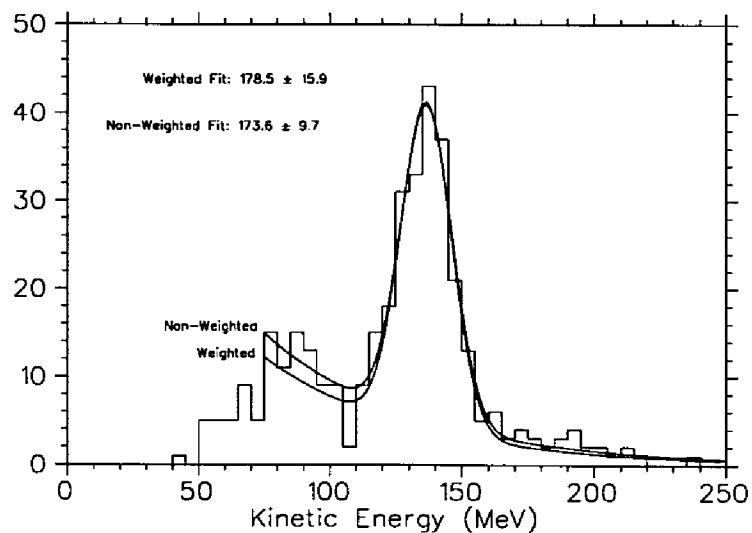


FIG. 4.30: Total kinetic energy distribution of the final events with a fit composed of a gaussian and an exponential in the [75,250] MeV region.

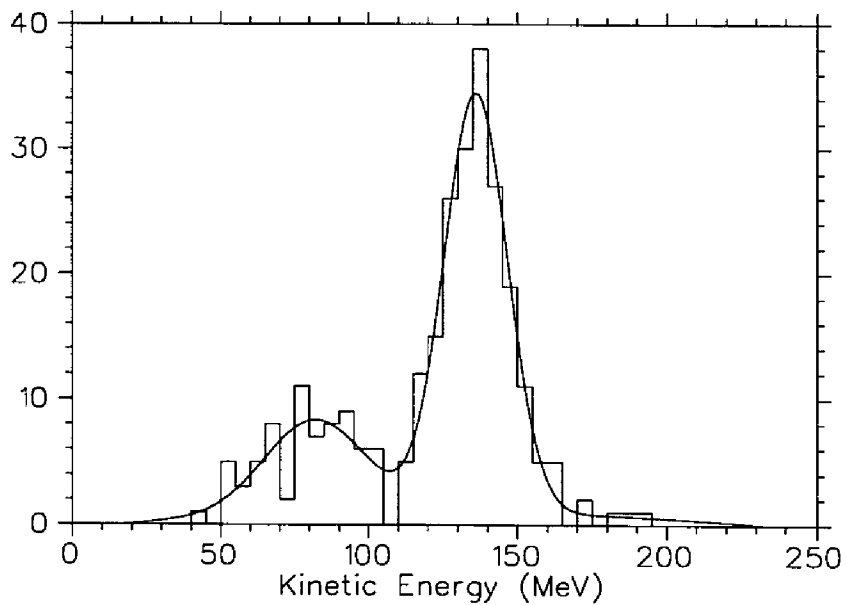


FIG. 4.31: Total kinetic energy distribution of the "purified" final events with a fit composed of two gaussians and a second-degree polynomial.

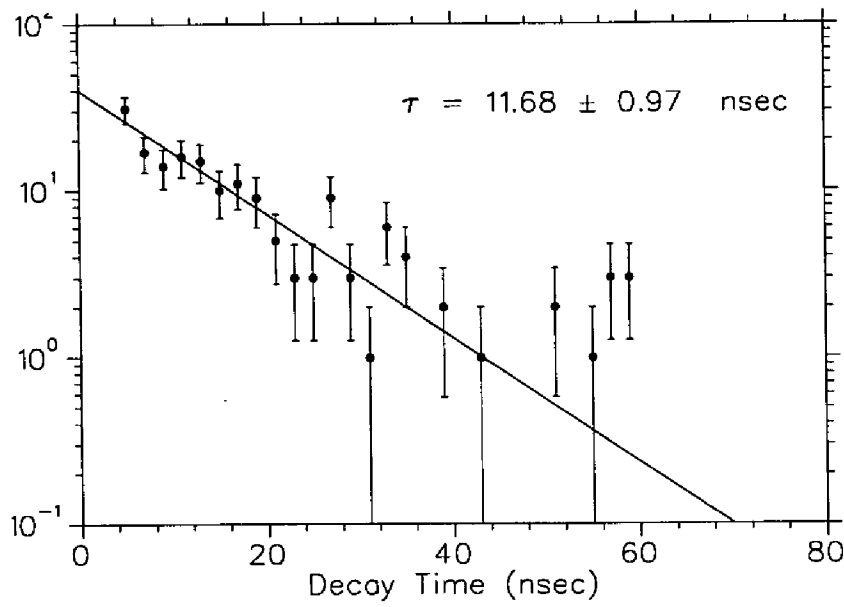


FIG. 4.32: The kaon decay time in the purified $\pi\mu\mu$ sample.

Chapter 5

Acceptance

The branching ratio for $K^+ \rightarrow \pi^+ \mu^+ \mu^-$ is determined from three essential numbers:

$$\text{Branching Ratio} = \frac{\# \text{ of } \pi\mu\mu \text{ events}}{\# \text{ of Kaon decays} \times \text{Acceptance}}$$

In the previous chapter we arrived at 196.0 ± 16.7 as the total number of $\pi\mu\mu$ events in our final sample. The number of kaon decays is primarily determined from the on-line scalers. These counters keep a record of various quantities measured during each spill. Recall that

$$KT \equiv \dot{C}_K \cdot B4 \cdot E_{TG}$$

During the time it takes the trigger to examine a kaon decay, and also while a candidate event is being recorded by the data acquisition system, the information in all subsystems regarding that event is frozen. This means that the detector is not attentive to any kaon decays during this time. This status is controlled by assertion

of the DT inhibit signal. Since the branching ratio should be determined based on the number of "observed" kaon decays, the KT_{live} scaler keeps track of the number of KT counts while the DT was not asserted; in other words,

$$KT_{live} \equiv KT \cdot \overline{DT}$$

The scalers are recorded and reset at the end of each spill. The analysis program KOFIA sums up the accumulated values of the scalers for all the runs analyzed. The total number of KT_{live} for the entire data set can thus be obtained. Nevertheless, this number does not exactly correspond to the actual number of kaons that decayed in the target while the detector was live. The main difference arises from the fact that a considerable fraction of kaons detected by the Čerenkov counter could undergo interactions or in-flight decays in the degrader with the product particles giving a $B4 \cdot E_{TG}$ signal. Moreover, if a pion accidentally satisfies the \check{C}_K condition and reaches the target, then it will also be counted as a KT_{live} . Another possibility is that a kaon leaves the target's fiducial region before decaying [14, 15]. The fraction f_S of the kaons stopped in the target has been determined by a normalization to the accepted $K_{\mu 2}$ branching ratio [20]. Thus,

$$K_{stop} = f_S \cdot KT_{live}.$$

The number of stopped kaons during the detector's live-time for the three years are shown in Table 5.1.

Year	KT_{live}	f_s	K_{stop}
1989	1.20349×10^{11}	0.681 ± 0.011	$(8.20 \pm 0.13) \times 10^{10}$
1990	1.97766×10^{11}	0.726 ± 0.012	$(14.36 \pm 0.24) \times 10^{10}$
1991	1.32778×10^{11}	0.584 ± 0.011	$(7.75 \pm 0.15) \times 10^{10}$
Total	4.5089×10^{11}	-	$(3.03 \pm 0.03) \times 10^{11}$

Table 5.1: Number of stopped kaons observed during the 1989-1991 runs.

5.1 Accidental Vetoes

The photon veto cuts are designed to eliminate decays in which a photon or an electron is present. However, they can also inflict non-negligible loss of acceptance due to the background activity in the detector's various subsystems (called *accidentals*). The efficiency of these cuts is a combination of two factors: i) their acceptance for the signal events, and ii) their inefficiencies due to the accidentals. The latter factor is discussed in this section.

$K_{\mu 2}$ is a desirable decay mode for measuring the accidental activity in the detector since the decay itself does not usually produce photons or prompt electrons that can cause random splashes of energy. The goal is to study the frequency of random energies in the RS, BV, or EC that are above the thresholds for the $\pi\mu\mu$ trigger or Pass3 cuts and that appear within each corresponding time window. Clearly the part of the RS containing the charged track had to be excluded first. In order to avoid counting any track-related energies not included in the RS track as accidental, the same-layer counters in the adjacent two sectors for each track element were also excluded.

The samples of $K_{\mu 2}$ events for this study were obtained from the $K_{\mu 2}$ triggers defined as:

$$\text{Level 0 } (K^+ \rightarrow \mu^+ \nu_{\mu}(1)) \equiv (T \cdot A) \cdot B_{CT} \cdot K_T \cdot (19_{CT} + 20_{CT} + 21_{CT}).$$

The triggers represent a prescaled sample of the $K_{\mu 2}$ decays that were mixed in and recorded along with the rare decay triggers. The effects of the online and offline photon veto cuts were studied by applying them to a clean sample of $K_{\mu 2}$ events as described below. It should be noted that although some of the requirements in the $\pi\mu\mu$ trigger (such as delayed coincidence) are not used in $K_{\mu 2}$ triggers, their status is nevertheless recorded. However, some trigger inefficiencies cannot be directly measured because of certain $K_{\mu 2}$ trigger requirements. The first one is the so called *muon veto* in the $\pi\mu\mu$ trigger which requires $\overline{(19 + 20 + 21)}$. Clearly, all $K_{\mu 2}$ triggers have a hit in at least one of these three layers. The second condition is the $\pi\mu\mu$ level 1 cut on the sum of energies in layers C through 11. Once again, all $K_{\mu 2}$ triggers deposit energy in these layers as their tracks are required to penetrate as far as layer 19. The last condition has to do with an accidental extension of a charged track in $\pi\mu\mu$ beyond layer B due to a random hit in one of the CT sectors. The above three cases were studied by simulating the trigger pulse widths (~ 40 nsec) and the discriminator thresholds (0.5 MeV for individual counters and 5.0 MeV for the level 1 energy sum) using the ADC and TDC information.

As a first step, the run number of each $K_{\mu 2}$ trigger was required to be within the

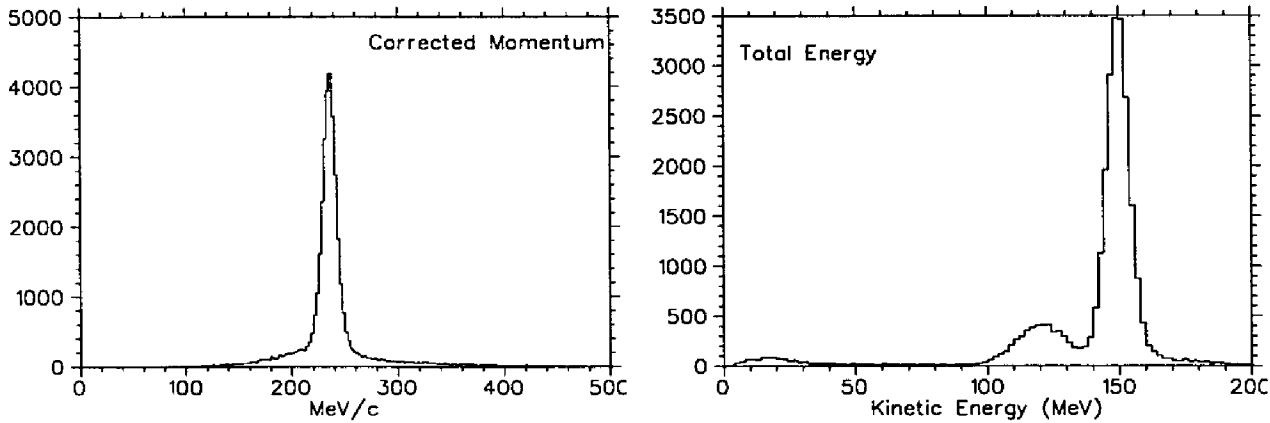


FIG. 5.1: Corrected momentum of the reconstructed $K_{\mu 2}$ triggers and the total energy of the ones that pass the [225,260] MeV/c momentum cut.

list of runs spanning the $\pi\mu\mu$ triggers. The following cuts were then applied in order to extract the $K_{\mu 2}$ events:

1. One RS-DC-TG matched track.
2. One RS track stopping short of layer 21 in order to avoid the muons that enter the BV.
3. Total momentum within [225,260] MeV/c
4. Total energy within [140,160] MeV

Figure 5.1 shows the momentum of the reconstructed events and the total energy of those that pass the momentum cut. For studying the accidentals, the on-line delayed coincidence was also required in order to further refine the sample.

The prompt energy cuts, exactly as they appear in the analysis, were applied to the selected sample for each year. In addition, the status of the veto trigger bits (L0BV, L0ECM, L0ECP) was examined. The sequential application of these cuts

Cut	1989	1990	1991
$K_{\mu 2}$ after on-line Delayed Coincidence	10193	16407	9862
$E_{\text{outer layers}}^{\text{RS}} < 1 \text{ MeV}$	9996	16012	9560
INTIME energy in BV $< 1 \text{ MeV}$	9838	15697	9350
INTIME energy in EC $< 1 \text{ MeV}$	8818	13610	7888
$E_{\text{inner layers}}^{\text{RS}} < 1 \text{ MeV}$	8663	13326	7699
\overline{LOBV}	8609	13225	7619
\overline{LOECM}	8468	12924	7452
\overline{LOECP}	8373	12749	7299
$(19 + 20 + 21)$	8269	12553	7157
$\Sigma(C + 11 + 12 + 13) < 5 \text{ MeV}$	8202	12418	7064
Charged track accidental extension	8164	12363	7026
Raw Efficiency	0.801 ± 0.004	0.754 ± 0.003	0.712 ± 0.005

Table 5.2: INTIME and trigger accidental vetoing in the $K_{\mu 2}$ data samples.

and conditions is necessary to eliminate any correlations which might result in double-counting an accidental. The surviving events were then subject to the simulation of the online requirements on muon veto and level 1 energy sum. For each condition, the INTIME energies in the corresponding layers—after excluding the track—were examined. The accidental extension of the charged track was studied by measuring INTIME energies in the individual modules in layers C through 18 in the 3 sectors opposite to the $K_{\mu 2}$ muon track.

Because of the differences between the Range Stack topologies of the charged tracks appearing in the $K_{\mu 2}$ and $\pi\mu\mu$ events, certain corrections must be applied to the above numbers. In estimating these corrections, it is assumed that a typical $K_{\mu 2}$

track extends as far as layer 18, whereas a typical $\pi\mu\mu$ event includes two T+A+B tracks. Since the $K_{\mu 2}$ charged track modules are excluded as the accidental hits are measured, their actual number in a $\pi\mu\mu$ event could be underestimated. In the following, the true rejection ξ of each cut will be estimated. The correction factor η to be applied to the raw efficiency will then be calculated as

$$\eta = \frac{a - (a - b) \cdot \xi}{b}$$

where a and b are the number of $K_{\mu 2}$ events before and after the cut.

1. $E_{\text{outer layers}}^{\text{RS}}$: the $K_{\mu 2}$ sample under-estimates the number of accidentals. In $\pi\mu\mu$ all the 11 layers \times 24 sectors can be subject to an accidental. In a typical $K_{\mu 2}$ event about 30 modules (along the track and its vicinity) were excluded in this region. Therefore the accidental rejection is higher by

$$\xi_1 = \frac{11 \times 24}{11 \times 24 - 30} = 1.128$$

$$\Rightarrow \eta_1 = \begin{cases} \frac{10193 - (10193 - 9996) \cdot 1.128}{9996} = 0.997 & \text{For 1989} \\ \frac{16407 - (16407 - 16012) \cdot 1.128}{16012} = 0.997 & \text{For 1990} \\ \frac{9862 - (9862 - 9560) \cdot 1.128}{9560} = 0.996 & \text{For 1991} \end{cases}$$

2. $E_{\text{inner layers}}^{\text{RS}}$: $K_{\mu 2}$ sample under-estimates the number of accidentals. A typical

$\pi\mu\mu$ track hits between 5 to 8 modules—average 6.5—in this region (T = 1 module, A = 4 modules, B = 3 modules) whereas $K_{\mu 2}$ excludes 3×10 modules (T through C and the vicinity, C = 2 modules). Thus the rejection is higher by

$$\xi_2 = \frac{10 \times 24 - 2 \times 6.5}{10 \times 24 - 30} = 1.081$$

$$\Rightarrow \eta_2 = \begin{cases} \frac{8818 - (8818 - 8663) \cdot 1.081}{8663} = 0.999 & \text{For 1989} \\ \frac{13610 - (13610 - 13326) \cdot 1.081}{13326} = 0.998 & \text{For 1990} \\ \frac{7888 - (7888 - 7699) \cdot 1.081}{7699} = 0.998 & \text{For 1991} \end{cases}$$

3. $(19 + 20 + 21)$: The muon track in layers 19 & 20 and their adjacent modules (total of 6 counters) were excluded in the $K_{\mu 2}$ sample. Therefore, the number of accidentals in 19 through 21 for all 24 sectors was underestimated by

$$\xi_3 = \frac{24 \times 3}{24 \times 3 - 6} = 1.091$$

$$\Rightarrow \eta_3 = \begin{cases} \frac{8373 - (8373 - 8269) \cdot 1.091}{8269} = 0.999 & \text{For 1989} \\ \frac{12749 - (12749 - 12553) \cdot 1.091}{12553} = 0.999 & \text{For 1990} \\ \frac{7299 - (7299 - 7157) \cdot 1.091}{7157} = 0.998 & \text{For 1991} \end{cases}$$

4. $\sum(C + 11 + 12 + 13) < 5 \text{ MeV}$: In the $K_{\mu 2}$ events, the part of the track going through this region and its vicinity was excluded whereas in $\pi\mu\mu$ events the entire 24×5 layers ($C = 2$ layers) are subject to accidentals. Therefore, the rejection was underestimated by

$$\xi_4 = \frac{24 \times 5}{24 \times 5 - 15} = 1.143$$

$$\Rightarrow \eta_4 = \begin{cases} \frac{8269 - (8269 - 8202) \cdot 1.143}{8202} = 0.999 & \text{For 1989} \\ \frac{12553 - (12553 - 12418) \cdot 1.143}{12418} = 0.998 & \text{For 1990} \\ \frac{7157 - (7157 - 7064) \cdot 1.143}{7064} = 0.998 & \text{For 1991} \end{cases}$$

5. Charged track accidental extension: The accidentals in layers C through 21 of the 3 opposite sectors in $K_{\mu 2}$ give the rate for a CT generated by one T.A. Two T.A will have twice the possibility of suffering from an accidental extension. Therefore, the corresponding loss in each year has to be doubled.

$$\xi_5 = 2$$

Year	1989	1990	1991
Raw Efficiency	0.801 ± 0.004	0.754 ± 0.003	0.712 ± 0.005
Correction factor	0.989	0.988	0.985
Corrected Efficiency	0.792 ± 0.004	0.745 ± 0.003	0.701 ± 0.005

Table 5.3: Efficiency of the trigger and INTIME cuts due to the accidentals.

$$\Rightarrow \eta_5 = \begin{cases} \frac{8202 - (8202 - 8164) \cdot 2}{8164} = 0.995 & \text{For 1989} \\ \frac{12418 - (12418 - 12363) \cdot 2}{12363} = 0.996 & \text{For 1990} \\ \frac{7064 - (7064 - 7026) \cdot 2}{7026} = 0.995 & \text{For 1991} \end{cases}$$

The product of the above numbers yields the additional rejection due to accidental hits. The raw and corrected efficiencies of the INTIME cuts due to accidental vetoing are summarized in table 5.3.

5.2 Delayed Coincidence

The selected $K_{\mu 2}$ events described in the previous section were used to measure both the online and offline delayed coincidence acceptance. The online acceptance was determined from the fraction of events with the online delayed coincidence asserted. SWATH (see Section 4.3.1) was applied to these events in order to get the fraction that pass the offline cut. The delayed coincidence acceptances are shown in table 5.4.

Since the efficiencies of most of the Pass3 cuts are determined from the UMC-

Year	Online	Offline	Overall acceptance
1989	0.799 ± 0.004	0.931 ± 0.003	0.744 ± 0.004
1990	0.814 ± 0.003	0.933 ± 0.002	0.759 ± 0.003
1991	0.787 ± 0.004	0.923 ± 0.003	0.726 ± 0.004

Table 5.4: Acceptance factors for both the online and offline delayed coincidence cuts.

generated data, it is important to simulate the $\pi\mu\mu$ events that pass the trigger while avoiding any double-counting. The online delayed coincidence condition in the $\pi\mu\mu$ trigger provides certain advantages for SWATH in terms of correct identification thanks to the imposed online K- π time separation. Thus the UMC-generated $\pi\mu\mu$ events should possess this feature for a realistic efficiency measurement for SWATH. However, the exact delayed coincidence efficiency should be entirely determined from the data. The problem is approached as following: in UMC, a cut was placed at the kaon decay time. This cut simulates the time separation between the K-“ π ” tracks that SWATH benefits from. However, the acceptance of the offline delayed coincidence cut is ignored when Pass3 is run on the UMC- $\pi\mu\mu$ events, and it is replaced by the measured online/offline combined values.

The position of the cut on the decay-time was selected after studying the corresponding spectrum for the stopped kaons in UMC. Notice that since the UMC kaons do not travel through a Čerenkov counter, it is not possible to simulate the real trigger pulses for delayed coincidence. The kaon decay time is the closest number for this purpose. It is desirable to place this cut as close to 2 nsec (the online value) as possible while staying at a safe interval below it in order to avoid rejecting events that

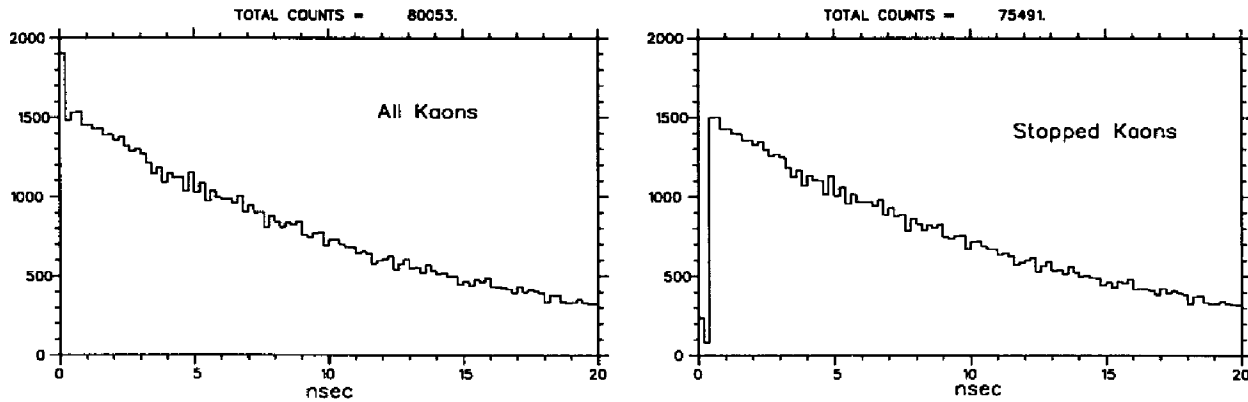


FIG. 5.2: The decay time for the kaons in UMC $\pi\mu\mu$ events. The spike at zero for all kaons corresponds to the decays in flight. The right plot indicates that the UMC kaons stop about 0.5 nsec after they are generated.

would otherwise pass the offline cut. The decay-time spectra of all the kaons and the ones that stopped before decaying are shown in Figure 5.2. A cut was placed on the kaons decaying before 1.5 nsec. This correspond to a ~ 1 nsec time elapsed after a kaon stops which is well below the approximately 2 nsec in the trigger.

5.3 Drift Chamber Reconstruction

Whereas the geometrical acceptance of the signal can be determined from the Monte Carlo, the detailed Drift Chamber reconstruction efficiency is not perfectly simulated and needs to be measured from the data. Almost all of the final $\pi\mu\mu$ events consist of two positive tracks in the Drift Chamber. These tracks are very unlikely to cross each other. Therefore, the two-track reconstruction efficiency for real data can be estimated as the square of the efficiency for events with a single, positive, low-momentum track.

The events for this study were selected from the $\pi\gamma\gamma(2)$ -type triggers in each

year.¹ The goal was to single out the events in which all the subsystems besides the DC point to the presence of a single low-momentum charged track in the event. Again, it was required that each trigger be within the list of run numbers spanning the $\pi\mu\mu$ triggers. The selection criteria were:

- Presence of two photon clusters in the BV or the RS which reconstruct a π^0 invariant mass.
- A single RS track that does not extend beyond layer C.
- Successful kaon and “pion” track found in the target using the DC-independent TG code, TARBNK.
- A single I-counter hit.

The events surviving these conditions are basically $K_{\mu 3}$, $K_{e 3}$, and some $K_{\pi 2}$ events, all of which should include a charged track in the DC. The DC code was then applied to these events, and the number of successful reconstructions (including the z-fitting) yielded the single track efficiency. The same procedure was applied to the UMC-generated $K_{\mu 3}$ events that passed the $\pi\gamma\gamma(2)$ trigger. The ratio of the real to UMC squared single-track efficiencies is used as the normalization factor. The results are tabulated in Table 5.5.

¹When a sufficient number of $\pi\gamma\gamma(2)$ triggers were not available, the required events were skimmed off by applying the online $\pi\gamma\gamma(2)$ trigger conditions (see Section 4.4.1) to the abundant $K_{\pi 2}$ monitor events using the trigger bits.

Year	Single-track efficiency	Two-track efficiency (ϵ_{DC})	$\epsilon_{DC}^{\text{data}} / \epsilon_{DC}^{\text{UMC}}$
UMC	0.993 ± 0.002	0.987 ± 0.002	-
1989	0.906 ± 0.014	0.820 ± 0.020	0.831 ± 0.020
1990	0.921 ± 0.013	0.849 ± 0.018	0.860 ± 0.018
1991	0.940 ± 0.009	0.884 ± 0.013	0.896 ± 0.013

Table 5.5: Single-track and the inferred two-track DC reconstruction efficiencies for low-momentum events. The latter is used to normalize the DC efficiency for the UMC-generated events.

5.4 Mass Cut

Although the empirical smearing of the RS-track energies can successfully simulate the observed mass resolutions of the pions and the muons, the exact acceptance of the mass cut hinges on the shape of the tails of the distributions and their momentum dependence. Therefore, the acceptance of a [60,190] MeV cut on K_{e4} FITPI pions (*i.e.* pions with an observable $\pi \rightarrow \mu$ signature) and also $K_{\mu 3}$ muons were measured in three momentum bins: [60,100], [100,140], and [140,180] MeV/c (see Figures 5.3 and 5.4). Then the lower and upper limits of the mass cut on the UMC-generated events were adjusted for each bin, and for either particle type, so that the same acceptance would be achieved. Since the chopping of the tails was to be simulated in UMC, only the upper limit for pions and the lower one for muons were adjusted. The cuts are tabulated in Tables 5.6 and 5.7.

In applying the mass cuts to the UMC data, first the identity of the particle is looked up in the track bank, and then the cuts appropriate to the particle and the measured momentum are applied. This method simulates the actual cuts for UMC

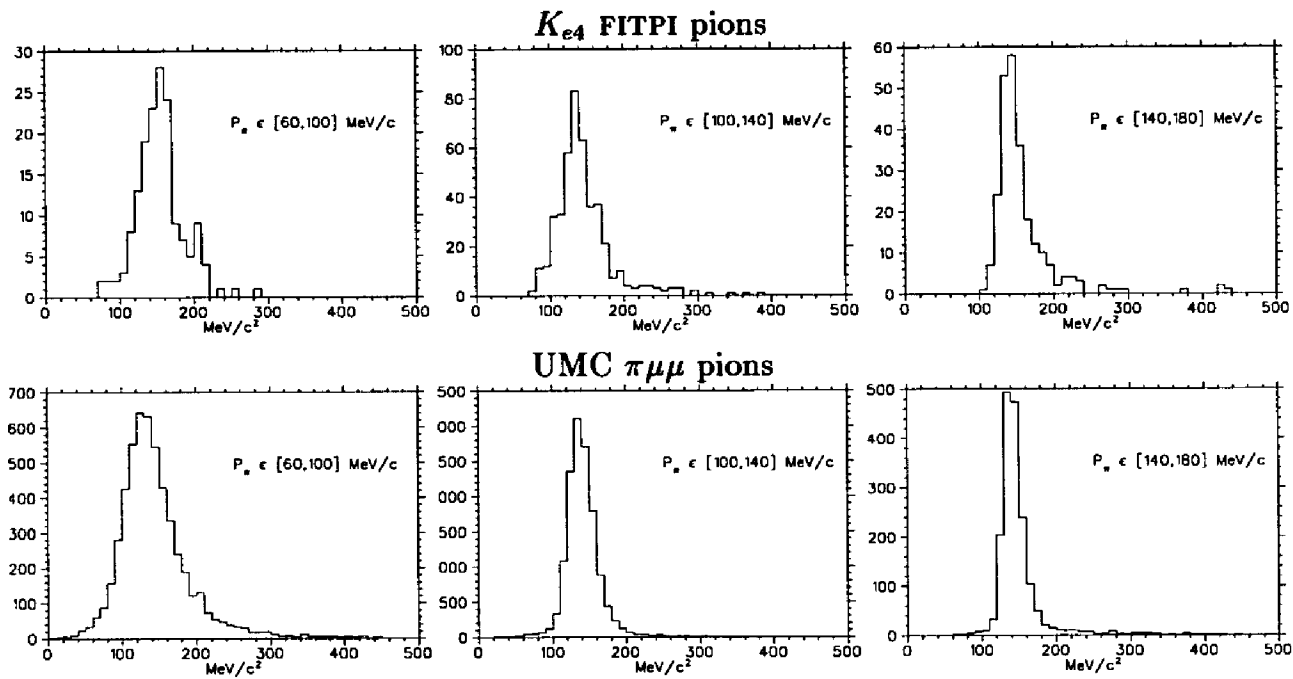


FIG. 5.3: Mass plots for K_{e4} -FITPI and also UMC- $\pi\mu\mu$ pions for the three momentum bins.

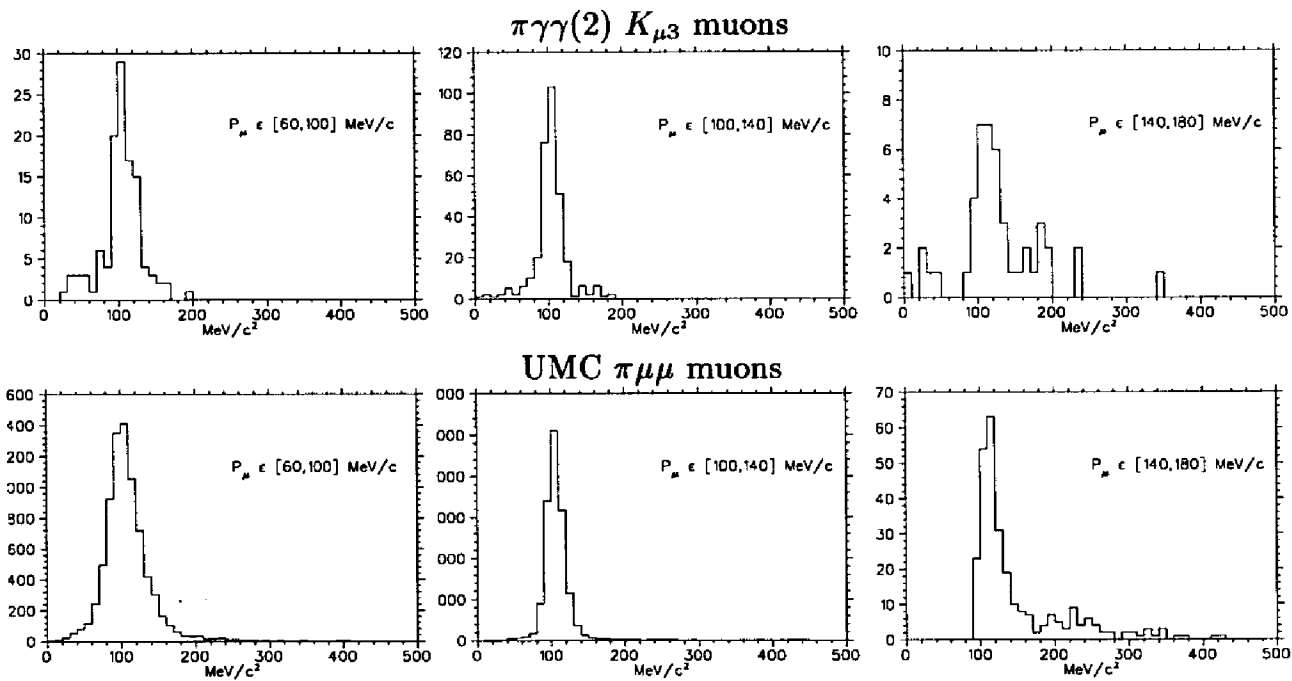


FIG. 5.4: Mass plots for $\pi\gamma\gamma(2)$ - $K_{\mu 3}$ and also UMC- $\pi\mu\mu$ muons for the three momentum bins.

Momentum \in [60,100] MeV/c	Cut	Efficiency	Fraction
K_{e4} FITPI π^+	[60,190] MeV	0.870 ± 0.027	19%
UMC $\pi\mu\mu$ π^+	[60,192] MeV	0.869 ± 0.005	26%
Momentum \in [100,140] MeV/c	Cut	Efficiency	Fraction
K_{e4} FITPI π^+	[60,190] MeV	0.904 ± 0.014	52%
UMC $\pi\mu\mu$ π^+	[60,167] MeV	0.908 ± 0.002	66%
Momentum \in [140,180] MeV/c	Cut	Efficiency	Fraction
K_{e4} FITPI π^+	[60,190] MeV	0.883 ± 0.020	29%
UMC $\pi\mu\mu$ π^+	[60,166] MeV	0.886 ± 0.008	8%

Table 5.6: The mass cut efficiency for K_{e4} pions in three momentum bins. The adjusted cuts for UMC $\pi\mu\mu$ pions simulate the measured efficiency. The last column shows the fraction of events in each momentum bin.

Momentum \in [60,100] MeV/c	Cut	Efficiency	Fraction
$\pi\gamma\gamma(2)$ $K_{\mu 3}$ μ^+	[60,190] MeV	0.904 ± 0.028	24%
UMC $\pi\mu\mu$ μ^+	[72,190] MeV	0.904 ± 0.003	34%
Momentum \in [100,140] MeV/c	Cut	Efficiency	Fraction
$\pi\gamma\gamma(2)$ $K_{\mu 3}$ μ^+	[60,190] MeV	0.959 ± 0.011	66%
UMC $\pi\mu\mu$ μ^+	[85,190] MeV	0.955 ± 0.002	65%
Momentum \in [140,180] MeV/c	Cut	Efficiency	Fraction
$\pi\gamma\gamma(2)$ $K_{\mu 3}$ μ^+	[60,190] MeV	0.783 ± 0.061	10%
UMC $\pi\mu\mu$ μ^+	[60,190] MeV	0.792 ± 0.024	1%

Table 5.7: The mass cut efficiency for $\pi\gamma\gamma(2)$ muons in three momentum bins. The adjusted cuts for UMC $\pi\mu\mu$ muons simulate the measured efficiency. The last column shows the fraction of events in each momentum bin.

by accepting or rejecting the events that are at the tails of the mass distributions.

5.5 Acceptance Factors from Monte Carlo

The major factor in the $\pi\mu\mu$ acceptance is due to the trigger as demonstrated in Table 4.1. The previous sections in this chapter described the reconstruction factors that needed to be determined based on various real events. The remaining factors of the acceptance was obtained by running the Pass3 code on the UMC-generated $\pi\mu\mu$ events. In generating the events, chiral perturbation with the parameter $w_+ = 0.89$ was assumed. The following modifications were included in the analysis code when dealing with the UMC data:

- The mass cuts were applied with the appropriate ranges in each momentum bin as explained above.
- The $B_NTGT \geq 9$ condition was skipped.
- No Target energy correction factor was applied.

The results are shown in table 5.8. Based on the number of surviving events, the Pass3 acceptance for UMC- $\pi\mu\mu$ events is

$$\epsilon_{\text{Pass3}}^{\text{UMC}} = 0.259 \pm 0.002$$

From Table 5.9, the offline delayed coincidence acceptance for the UMC- $\pi\mu\mu$ events is

$$\epsilon_{\text{DelCo}}^{\text{UMC}} = 0.938 \pm 0.001$$

Therefore, the Pass3 acceptance without the offline delayed coincidence is

$$\epsilon_{\text{Pass3, No DelCo}}^{\text{UMC}} = \frac{\epsilon_{\text{Pass3}}^{\text{UMC}}}{\epsilon_{\text{DelCo}}^{\text{UMC}}} = \frac{0.259 \pm 0.002}{0.938 \pm 0.001} = 0.276 \pm 0.002$$

5.6 Systematic Errors

Section 4.6.3 describes the systematic error associated with the fitted number of signal events. Here other possible sources of systematic error are studied by evaluating variations in the acceptance associated with uncertainties about the essential detector elements. For each element, the corresponding parameter in UMC was varied by the errors in their measurements. The generated particles then propagated through the slightly changed detector. Finally Pass3 was run on these UMC-generated triggers. Acceptance variations were then measured only for those cuts that were directly affected by the change.

5.6.1 Systematic Error Associated with the B -field

Figure 5.5 shows the trigger acceptance as a fitted function of the magnetic field in a wide range. The uncertainty in the measurement of the B -field is actually quite

Cut	Events surviving
Events entering	55331
2 or 3 consistent T·A	55149
RS inner layers ($T \rightarrow C$) energy < 120 MeV	54751
RS outer layers (11 \rightarrow 21) energy < 1 MeV	54624
BV energy < 1 MeV	54518
EC energy < 1 MeV	54253
≥ 2 RS-DC matched tracks	52419
Momentum of RS-DC tracks < 170 MeV/c	51612
TG reconstruction	44721
RS inner layer energy not associated with a track < 1 MeV	44301
More than two tracks in one cluster	43789
Mass of any RS-DC track > 80 MeV/c ²	41996
Mass of the negative RS-DC track < 135 MeV/c ²	40259
Mass of the positive RS-DC track < 185 MeV/c ²	36259
++ combination of charges	15495
Kinetic energy of the TG stub $\in [-30, 20]$ MeV	15174
P_{missing} in events with 3 DC-TG matched tracks < 60 MeV/c	15106
Angle of the TG stub within 0.9 radian of the expected direction	14353
Total UMC Efficiency	0.259 ± 0.002

Table 5.8: The number of UMC- $\pi\mu\mu$ events surviving various Pass3 cuts.

Target Reconstruction Cuts	Events surviving
Events entering	51612
2 or 3 SWATH tracks	50012
Offline delayed coincidence	46919
Same kaon blob associated with the tracks	45857
Times of pion tracks within 6 nsec of each other	45697
Maximum gap between kaon and "pion" cells < 1.8 cm	45180
Maximum gap within "pion" tracks < 1.8 cm	44938
Maximum gap between any "pion" track and the corresponding TG edge < 1.8 cm	44878
Too many DC tracks through the kaon vertex	44816
Consistent I-counter hits along the tracks	44722
Too many disconnected energy clusters	44721

Table 5.9: Breakdown of the number of UMC- $\pi\mu\mu$ events surviving the various Target reconstruction cuts.

small (5 to 10 gauss). Hence the systematic error in the trigger acceptance due to a

$\delta B = 10$ Gauss uncertainty at $B = 10$ KGauss is

$$\text{Trigger } \frac{\delta\epsilon}{\epsilon} = \left| \frac{-0.38B + 2.2}{-0.19B^2 + 2.2B + 9.0} \right| \delta B = 0.13\%$$

Figure 5.6 shows the total acceptance as a function of the B -field. The UMC events for this plot were generated with various values of B . They were then analyzed with the PASS3 code whose DC-tracking routine assumes a $B = 10$ KGauss field. Therefore the tracks of the events generated with $B < 10$ KGauss look too stiff and are vetoed as electrons by PASS3. This causes the suppression of the total acceptance for $B < 10$ KGauss in Figure 5.6. Figure 5.7 shows the total acceptance as the B-field is varied by smaller amounts. From the shown linear fit to the data,

$$\text{Total } \frac{\delta\epsilon}{\epsilon} = \left| \frac{3.7}{3.7B - 7.3} \right| \delta B = 0.12\%$$

for the overall acceptance. Cancelling effects in the trigger and PASS3 were found to cause the overall variation to be slightly smaller than the one due to the trigger. The larger of the above two errors, 0.13%, is taken as the systematic error associated with the uncertainty in the magnetic field.

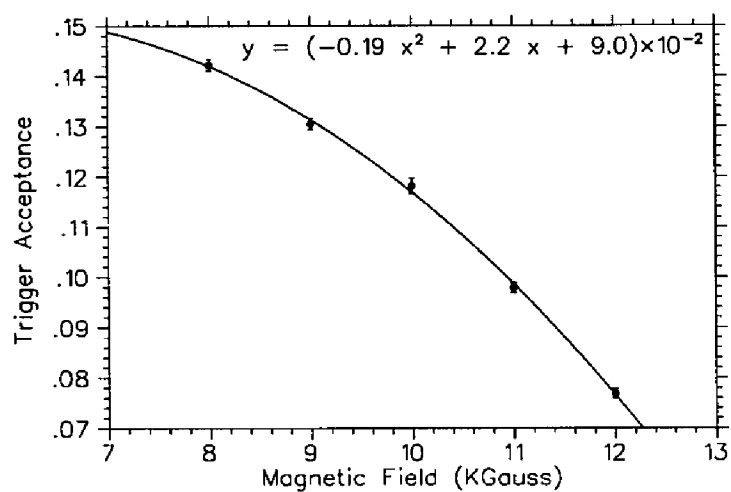


FIG. 5.5: Trigger acceptance as a function of the magnetic field.

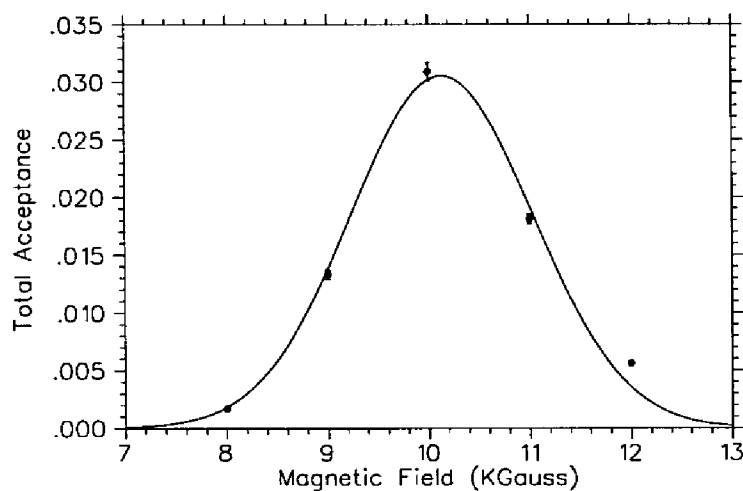


FIG. 5.6: Total acceptance as a function of the magnetic field in a wide range. The fitted gaussian is simply used as an empirical function to represent the overall shape.

5.6.2 Systematic Error Associated with other UMC-Measured Acceptance Factors

Table 5.10 shows the systematic errors in the acceptance as various UMC parameters are varied by their estimated errors. In each case only the affected cuts contribute to the reported variations. For example, the effects of varying the Drift Chamber end-plates' thickness can be measured from the variations in the EC photon veto cuts (both online and offline). The "Acceptance" column shows the combined efficiencies of the affected cuts in each case.

5.6.3 Systematic Errors Associated with the Accidentals

The uncertainties associated with simulating certain $\pi\mu\mu$ trigger conditions in studying the accidental vetoing are shown in Table 5.11. The table includes results for the 1989 data. The systematic errors for the other two years are at the same level to within their statistical errors.

5.6.4 The Overall Systematic Error

The above numbers can be combined into two components: systematic errors in *i*) the signal, and *ii*) the acceptance. The former is 17.5 events (or 8.9%) as explained in Section 4.6.3. The latter is obtained by adding in quadrature the largest (in absolute value) percentages of error in each category given in Tables 5.10 and 5.11 as well as the 0.13% for the B-field uncertainty. This yields a 7.9% uncertainty in the acceptance.

Source	Nominal Value	Variation	Acceptance	% Change
RS counters' thickness	1.905 cm	+0.05 cm	0.971 ± 0.002	$+0.4 \pm 0.2$
RS counters' thickness	1.905 cm	<i>reference</i>	0.967 ± 0.001	-
RS counters' thickness	1.905 cm	-0.05 cm	0.959 ± 0.002	-0.8 ± 0.2
IC thickness	0.635 cm	+0.20 cm	0.153 ± 0.002	-3.2 ± 1.9
IC thickness	0.635 cm	<i>reference</i>	0.158 ± 0.001	-
IC thickness	0.635 cm	-0.20 cm	0.167 ± 0.002	$+5.6 \pm 1.9$
DC endplates' thickness	1.73 & 1.35 cm	+1 cm	0.995 ± 0.001	$+0.1 \pm 0.1$
DC endplates' thickness	1.73 & 1.35 cm	<i>reference</i>	0.994 ± 0.001	-
DC endplates' thickness	1.73 & 1.35 cm	-1 cm	0.975 ± 0.002	-1.9 ± 0.2
N_{TG} in UMC	20	-2	0.958 ± 0.002	$+3.2 \pm 0.3$
N_{TG} in UMC	20	-1	0.946 ± 0.003	$+1.9 \pm 0.4$
N_{TG} in UMC	20	<i>reference</i>	0.928 ± 0.002	-
N_{TG} in UMC	20	+1	0.909 ± 0.003	-2.0 ± 0.4
N_{TG} in UMC	20	+2	0.888 ± 0.004	-4.3 ± 0.5
UMC mass resolution	$130./E$ MeV	down 10%	0.851 ± 0.006	$+2.7 \pm 0.8$
UMC mass resolution	$130./E$ MeV	down 5%	0.841 ± 0.005	$+1.6 \pm 0.7$
UMC mass resolution	$130./E$ MeV	<i>reference</i>	0.828 ± 0.002	-
UMC mass resolution	$130./E$ MeV	up 5%	0.823 ± 0.006	-0.6 ± 0.8
UMC mass resolution	$130./E$ MeV	up 10%	0.812 ± 0.006	-1.9 ± 0.8

Table 5.10: Systematic errors in the UMC-measured acceptance associated with uncertainties in various detector elements.

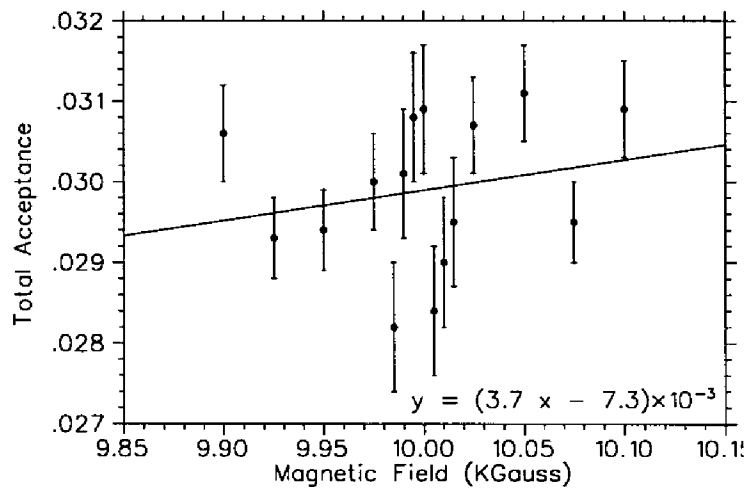


FIG. 5.7: Total acceptance as a function of the magnetic field in a short range.

Source	Nominal Value	Variation	Acceptance	% Change
Reference	-	-	0.812 ± 0.004	-
RS discrim. width	40 nsec	+10 nsec	0.803 ± 0.004	-1.1 ± 0.7
RS discrim. width	40 nsec	-10 nsec	0.819 ± 0.004	$+0.9 \pm 0.7$
RS discrim. threshold	0.5 MeV	+0.5 MeV	0.813 ± 0.004	$+0.1 \pm 0.7$
RS discrim. threshold	0.5 MeV	-0.3 MeV	0.812 ± 0.004	0.0 ± 0.7
Level 1 threshold	5 MeV	+1.0 MeV	0.812 ± 0.004	0.0 ± 0.7
Level 1 threshold	5 MeV	-1.0 MeV	0.811 ± 0.004	-0.1 ± 0.7

Table 5.11: Systematic errors associated with simulating the trigger requirements in studying the accidentals. The acceptance pertains to all the prompt energy cuts (both online and offline). The values are for the 1989 data.

Year	1989	1990	1991
<i>Requirement</i>	<i>Acceptance</i>		
Trigger	0.127 ± 0.001	0.087 ± 0.001	0.087 ± 0.001
Pass3 without offline delayed coincidence	0.276 ± 0.002	0.276 ± 0.002	0.276 ± 0.002
Online and offline delayed coincidence	0.744 ± 0.004	0.759 ± 0.003	0.726 ± 0.004
DC reconstruction	0.831 ± 0.020	0.860 ± 0.018	0.896 ± 0.013
Accidentals	0.792 ± 0.004	0.745 ± 0.003	0.701 ± 0.005
Total	0.0172 ± 0.0005	0.0117 ± 0.0003	0.0109 ± 0.0002

Table 5.12: Acceptance factors for the $\pi\mu\mu$ search.

5.7 Summary

Table 5.12 summarizes the acceptance factors to be used in the branching ratio calculation.

Chapter 6

Conclusion

Based on the 196.0 ± 16.7 events measured as a result of the fit to the total energy spectrum of the final events, the branching ratio for the $\pi\mu\mu$ decay can be calculated

as

$$BR = \frac{N_{\pi\mu\mu}}{K_{stop}^{1989} \cdot \epsilon_{1989} + K_{stop}^{1990} \cdot \epsilon_{1990} + K_{stop}^{1991} \cdot \epsilon_{1991}}.$$

From Tables 4.1 and 5.12, the values of the terms in the denominator are

$$\begin{aligned} K_{stop}^{1989} \cdot \epsilon_{1989} &= ((8.20 \pm 0.13) \times 10^{10}) \cdot ((1.72 \pm 0.05) \times 10^{-2}) \\ &= (1.41 \pm 0.05) \times 10^9 \end{aligned}$$

$$\begin{aligned} K_{stop}^{1990} \cdot \epsilon_{1990} &= ((14.36 \pm 0.24) \times 10^{10}) \cdot ((1.17 \pm 0.03) \times 10^{-2}) \\ &= (1.68 \pm 0.05) \times 10^9 \end{aligned}$$

$$\begin{aligned} K_{stop}^{1991} \cdot \epsilon_{1990} &= ((7.75 \pm 0.15) \times 10^{10}) \cdot ((1.09 \pm 0.02) \times 10^{-2}) \\ &= (8.45 \pm 0.23) \times 10^8 \end{aligned}$$

Hence,

$$\begin{aligned} BR &= \frac{196.0 \pm 16.7}{(1.41 \pm 0.05) \times 10^9 + (1.68 \pm 0.05) \times 10^9 + (8.45 \pm 0.23) \times 10^8} \\ &= \frac{196.0 \pm 16.7}{(3.935 \pm 0.074) \times 10^9} \\ &= (4.98 \pm 0.43_{stat}) \times 10^{-8}. \end{aligned}$$

From the systematic errors derived in Section 5.6, the systematic part of the error in the branching ratio is

$$\begin{aligned}
 BR &= \frac{196.0 \pm 17.5}{(1.41 \times 10^9 + 1.68 \times 10^9 + 8.45 \times 10^8) \cdot (1 \pm 0.079)} \\
 &= \frac{196.0 \pm 17.5}{(3.935 \pm 0.311) \times 10^9} \\
 &= (4.98 \pm 0.59_{sys}) \times 10^{-8}.
 \end{aligned}$$

Therefore, the branching ratio is quoted as:

$$BR(K^+ \rightarrow \pi^+ \mu^+ \mu^-) = (4.98 \pm 0.43_{stat} \pm 0.59_{sys}) \times 10^{-8}$$

6.1 w_+

As described in Section 2.2.1, the predicted branching ratio for $\pi\mu\mu$ in terms of the w_+ parameter is

$$BR(K^+ \rightarrow \pi^+ \mu^+ \mu^-) = (3.92 - 32.6w_+ + 70.3w_+^2) \times 10^{-9}$$

Using the measured branching ratio of $(4.98 \pm 0.43 \pm 0.59) \times 10^{-8}$ or $(4.98 \pm 0.73) \times 10^{-8}$, one obtains

$$w_+ = \begin{cases} +1.07 \pm 0.06 \\ -0.61 \pm 0.06 \end{cases}$$

The branching ratio was derived from acceptance measurements based on a $w_+ = 0.89$ hypothesis (see Sections 4.2.2 and 5.5). Therefore it is important to check the variations in the acceptance as a function of w_+ . Figure 6.1 shows the total acceptance measured as a function of w_+ . The plot indicates that the deviation from the $w_+ = 0.89$ acceptance is $\leq 12\%$ for $w_+ > 0.2$. This in turn results in an additional 0.05 uncertainty in the derived values of w_+ in a first iteration. Therefore,

$$w_+ = \begin{cases} +1.07 \pm 0.08 \\ -0.61 \pm 0.08 \end{cases}$$

6.2 Spectrum

Figure 6.2 shows the spectrum of $m_{\mu\mu}^2/m_{K^+}^2$ for the purified $\pi\mu\mu$ events as well as for the UMC-generated events within the signal region ($115 \text{ MeV} < E_{\text{tot}} < 155 \text{ MeV}$).

Figure 6.3 shows the Dalitz plots for the real and UMC two-track events. In this representation, E_{μ^+} is plotted versus E_{μ^-} . E_{μ^+} is calculated from the corrected momentum at the decay vertex of the “lighter” particle (*i.e.*, the RS-reaching track with the smaller calculated mass). E_{μ^-} is calculated from the expected momentum of the third track (using the corrected momenta of the two RS-reaching tracks and

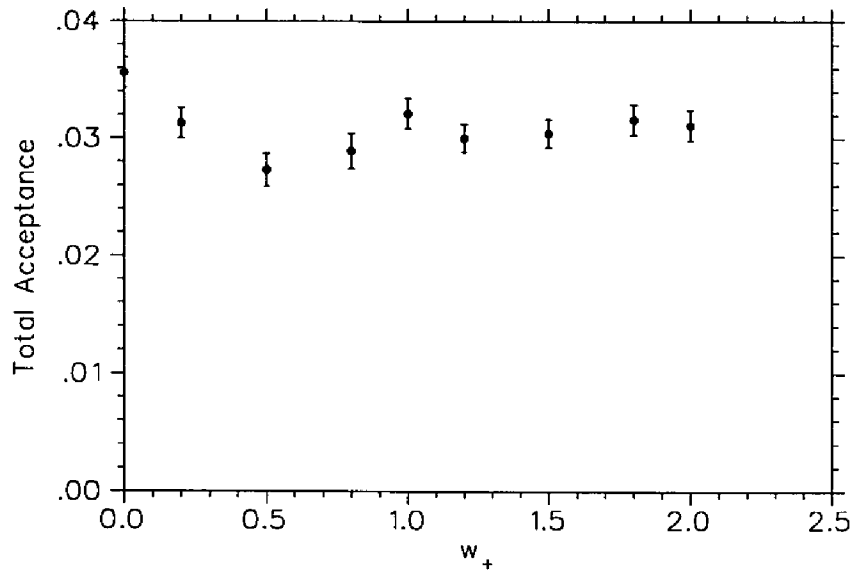


FIG. 6.1: Total acceptance for several values of $w_+ \geq 0$.

momentum conservation). The UMC events were generated with a chiral perturbation theory matrix element and $w_+ = 0.89$.

A detailed study of the observed spectra will be the subject of a future study.

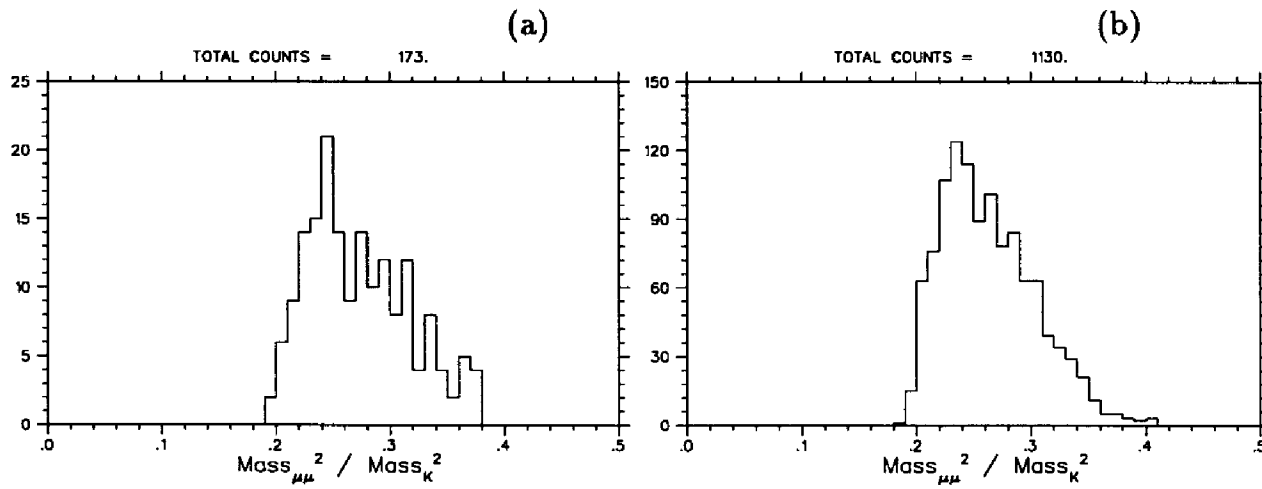


FIG. 6.2: Distribution of the normalized di-muon invariant mass $m_{\mu\mu}^2/m_{K^+}^2$ for the (a) purified and (b) UMC-generated $\pi\mu\mu$ events in the signal region ($115 \text{ MeV} < E_{\text{tot}} < 155 \text{ MeV}$).

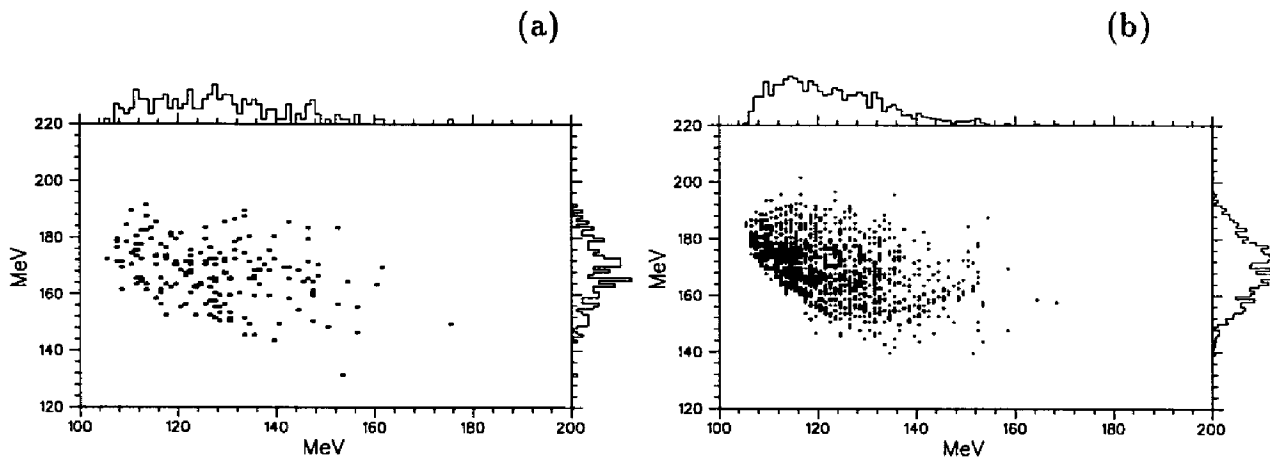


FIG. 6.3: A Dalitz representation of the (a) purified and (b) UMC-generated $\pi\mu\mu$ events within the signal region. Plotted is E_{μ^+} versus E_{μ^-} .

References

- [1] Mats A. Selen, *Hunting for the Rare Decay $K^+ \rightarrow \pi^+ \mu^+ \mu^-$* , DOE/ER/3072-49, Princeton University thesis (unpublished), (1989).
- [2] M.S. Atiya *et al.*, *Phys. Rev. Lett.* **63**, 2177 (1989).
- [3] J.S. Haggerty, C.Witzig, and L.Felawka, E787 Technical Notes # 275 and #277.
- [4] M. Kobayashi and K. Maskawa, *Prog. Theor. Phys.* **49**, 282 (1972).
- [5] S.L. Glashow, J. Iliopoulos, and L. Maiani, *Phys. Rev. D* **2**, 1285 (1970).
- [6] G. Ecker, A. Pich, and E. de Rafael, *Nucl. Phys.* **B291**, 692 (1987).
- [7] C. Alliegro *et al.*, *Phys. Rev. Lett.* **68**, 278 (1992).
- [8] J.S. Haggerty, E787 Technical Note # 262.
- [9] M.S. Atiya *et al.*, *Nucl. Instr. and Meth.* **A321**, 129 (1992).
- [10] M. Atiya, M. Ito, J. Haggerty, C. Ng, and F.W. Sippach, *Nucl. Instr. and Meth.* **A279**, 180 (1989).
- [11] T. Suzuki *et al.*, *Phys. Rev. C* **35**, 2212 (1987).

-
- [12] L. Littenberg and C. Witzig, *private communications*.
- [13] G.F. Knoll, *Radiation Detection and Measurement*, 2nd edition, John Wiley & Sons Inc., p. 222, 1989.
- [14] D. Akerib, D. Marlow and P.D. Meyers, E787 Technical Note # 186.
- [15] D. Akerib, D. Marlow and P.D. Meyers, E787 Technical Note # 168.
- [16] D. Eisenstein and P.D. Meyers, E787 Technical Note # 224.
- [17] M. Ardebili, D. Marlow and P.D. Meyers, E787 Technical Note # 228.
- [18] M. Ardebili, E787 Technical Note # 257.
- [19] M. Ardebili, E787 Technical Note # 280.
- [20] A. Turcot, E787 Technical Note # 281.
- [21] A. Bilal and C.G. Callac, *Nucl. Phys. B* **394** (1993)
- [22] S.W. Hawking, *Math. Phys.* **43** 199 (1975)
- [23] G. Backenstoss, *Ann. Rev. of Nuc. Sci.* **20**, 467 (1970)
- [24] R. Madey *et al.*, *Phys. Rev. C* **25** 3050 (1982)
- [25] G. Mechttersheimer *et al.*, *Phys. Lett.* 73B, 115 (1978)